Test Report of the Melt Spreading Tests ECOKATS-V1 and ECOKATS-1

CONTRACT FIKS-CT1999-00003

EX-VESSEL CORE MELT STABILIZATION RESEARCH

H. Alsmeyer, T. Cron, J. J. Foit, G. Messemer, S. Schmidt-Stiefel, W. Häfner, H. Kriscio

**Institut für Kern- und Energietechnik
Programm Nukleare Sicherheitsforschung**

November 2004

Forschungszentrum Karlsruhe

in der Helmholtz-Gemeinschaft

Test Report of the
Melt Spreading Tests ECOKATS-V1 and ECOKATS-1

CONTRACT FIKS-CT1999-00003

EX-VESSEL CORE MELT STABILIZATION RESEARCH

H. Alsmeyer, T. Cron, J. J. Foit, G. Messemer, S. Schmidt-Stiefel
W. Häfner*, H. Kriscio*

Institut für Kern- und Energietechnik
Programm Nukleare Sicherheitsforschung

*Becker Technologies, Eschborn, Germany

Abstract

As one of the major tasks of the ECOSTAR project, two large-scale experiments on oxidic melt spreading were performed. The experimental conditions were selected to represent low flow rate of oxidic melt, released with low overheat, so that stop of the spreading process may occur during ongoing melt release, and spreading would be incomplete. Besides the basic experimental information on spreading of large melt masses under low flow conditions, the experiments were designed to be used for the final validation of spreading codes. After completion of the validation process, the computer programs would be able to predict with sufficient accuracy the spreading process in case of an accident, which is expected to occur under less critical conditions than the actual experiment.

The report describes also the selection and characterization of the multi-component oxide melt, which simulates the ex-vessel oxide corium melt in an anticipated reactor accident. The melt was generated by a modified exothermic thermite reaction, and poured to the spreading surfaces under controlled conditions.

To improve the information about the rheological behaviour of the selected oxide melt, a pre-test ECOKATS-V1 was performed in which the oxide melt was spread in a 1-d flow channel. Together with qualified spreading calculations, this experiment allowed for estimation of the initial viscosity of the melt and characterization of the rheological behaviour in the freezing range. Furthermore, significant information about the nature of the 1-d spreading process during onset of solidification as well as growth and failure of a front crust was gained.

The large scale 2-d spreading experiment ECOKATS-1 was performed on a concrete surface, 4 m long and 3 m wide . 547 kg of oxide melt were released to the spreading surface during a period of 85 s. The melt and the spreading conditions were selected to represent the situation for which the melt stopped during the phase of melt inflow (incomplete spreading). Degassing of the concrete during the initial spreading phase has an important effect on the spreading process as can be seen e.g. in the inlet flow channel by comparison with the test ECOKATS-V1. Spreading on the large surface into the longitudinal direction already stopped at the first time after 1 m at 20 s, and was subsequently followed by a pronounced spreading towards the lateral walls, and a series of smaller outflows of melt through the front crust. The end of spreading was reached at 100 s equal to 15 s after the end of melt release. The total area that has finally been covered by the spread melt was 4.88 m^2.

Detailed material investigations were performed to determine the important properties of the melt, especially with respect to its viscosity and its freezing behaviour which dominate the spreading process. With this additional information, the physico-chemical properties of the multi-component melt are well characterized.

In both experiments, spreading of the oxide melt is characterized by pronounced thermal boundary layers that exist at the free surface of the melt on the one hand, and at the surface of the concrete or ceramic substrate on the other hand. This leads to the formation of crusts, while the bulk of the melt remains at high temperatures. This is evident because late outflows of melt through cracks in the front crust show still very high melt temperatures. The crust on the upper surface and especially at the leading edge of the melt is indeed responsible for the stop of the spreading process. At these locations, the relevant crust growth is controlled mainly by radiation. In the contrary,

the bottom crust has only little effect on spreading as that crust is easily overflowed by the bulk of the melt. Furthermore, as the bottom crust limits heat transfer to the substrate, heat conduction in the substrate has only minor influence on spreading.

The experimental conditions are described and detailed results are given. Both experiments have been used for blind post-test calculations for validation of advanced spreading codes.

Ergebnisse der Schmelzenausbreitungsexperimente ECOKATS-V1 und ECOKATS-1

Zusammenfassung

Als eine der wesentlichen Aufgaben des ECOSTAR Projekts wurden 2 groß-skalige Experimente zur Ausbreitung von Oxid-Schmelzen durchgeführt. Die experimentellen Bedingungen wurden so gewählt, dass sie den langsamen Ausfluss einer Oxid-schmelze mit geringer Überhitzung darstellen, so dass ein Stopp der Ausbreitung während des Ausflusses der Schmelze auftreten kann, und die Ausbreitung unvoll-ständig bleibt. Über die grundlegenden experimentellen Informationen zur Ausbreitung großer Schmelzemassen bei geringer Ausflußrate hinaus wurden die Experimente so ausgelegt, dass sie zur abschließenden Verifizierung von Rechenprogrammen ver-wendet werden können. Nach erfolgreicher Verifizierung sollten die Rechenprogram-me in der Lage sein, mit ausreichender Genauigkeit die Ausbreitung der Kernschmel-ze vorherzusagen, die im Falle eines Kernschmelzenunfalls unter weniger kritischen Bedingungen als im durchgeführten Experiment erwartet wird.

Der Bericht beschreibt die Auswahl und Charakterisierung der mehr-komponentigen Oxidschmelze, die die ex-vessel Kernschmelze in einem unterstellten Reaktor-Unfall simuliert. Die Schmelze wurde durch eine modifizierte exotherme Thermit-Reaktion erzeugt und unter kontrollierten Bedingungen auf die Ausbreitungsfläche geleitet.

Um die Kenntnis über die rheologischen Eigenschaften der ausgewählten Oxid-schmelze zu verbessern, wurde das Vorexperiment ECOKATS-V1 durchgeführt, bei dem sich die Schmelze in einem 1-dimensionalen Kanal ausbreitete. Dieses Experi-ment ermöglicht mit Hilfe qualifizierter Rechnungen zur Ausbreitung, die anfängliche Zähigkeit der Schmelze abzuschätzen und ihr rheologisches Verhalten innerhalb des Erstarrungsbereiches zu charakterisieren. Darüber hinaus wurden wichtige Informati-onen über den Ablauf der 1-dimensionalen Ausbreitung gewonnen, speziell im Hin-blick auf das Einsetzen der Erstarrung und das Wachsen und Versagen der Kruste an der Front der Schmelze.

Das Experiment ECOKATS-1 wurde als 2-dimensionales Ausbreitexperiment auf einer großen Betonfläche von 4 m Länge und 3 m Breite ausgeführt. 547 kg Oxidschmelze wurden während 85 s Auslaufzeit auf die Ausbreitfläche geleitet. Schmelze und Aus-breitbedingungen waren so gewählt, dass ein Stopp der Ausbreitung während der Aufgabe der Schmelze eintreten sollte (unvollständige Ausbreitung). Die Gasfreiset-zung aus dem Beton hat dabei einen wichtigen Einfluss auf den Ausbreitvorgang, wie z. B. durch die Ausbreitung im Einlaufkanal im Vergleich mit dem Experiment ECOKATS-V1 festgestellt werden kann. Die Ausbreitung der Schmelze auf der Fläche stoppte in Längsrichtung bereits nach 1 m nach 20 s, und erfolgte dann in Querrich-tung in Richtung der seitlichen Wände sowie durch eine Folge kleiner Schmelzenaus-flüsse durch Risse, die in der vorderen Kruste entstanden. Das Ende der Ausbreitung war 15 s nach dem Ende der Schmelzenzufuhr erreicht. Die gesamte von der Schmel-ze bedeckte Fläche betrug 4,88 m^2.

Ergänzend wurden detaillierte Materialuntersuchungen durchgeführt, um die wichtigen Eigenschaften der Schmelzen zu bestimmen, speziell bezüglich Zähigkeit und Erstar-rungsverhalten der Schmelze. Mit dieser zusätzlichen Information sind die physika-lisch – chemischen Eigenschaften der Schmelze gut charakterisiert.

In beiden Experimenten ist die Ausbreitung der Oxidschmelze durch die Ausbildung von Temperaturgrenzschichten charakterisiert, die einerseits an der freien Oberfläche der Schmelze und andererseits an ihrer Unterseite in Kontakt mit der Keramik- oder Betonfläche existieren. Dies führt zur Ausbildung von Krusten in diesen Bereichen, während der Zentralbereich der Schmelzenschicht seine hohe Temperatur behält. Dies ist erkennbar an der hohen Temperatur, mit der Schmelze aus Spalten aus der Frontkruste austritt. Die Kruste auf der Schmelzenoberseite und speziell an der Schmelzenfront ist für den Stopp der Ausbreitung verantwortlich. In diesen Bereichen wird das Wachstum der Kruste vorwiegend durch Wärmestrahlung gesteuert. Im Gegensatz dazu hat die Kruste an der Unterseite der Schmelze nur geringen Einfluss auf die Ausbreitung, da sie leicht von der Schmelze überströmt wird. Weiterhin begrenzt diese untere Kruste den Wärmeaustrag an die Ausbreitfläche, und damit bleibt der Einfluss der Wärmeleitung in der Ausbreitfläche auf die Ausbreitung gering.

Der Bericht beschreibt die experimentellen Bedingungen und die Ergebnisse der durchgeführten Experimente. Beide Experimente wurden für blinde Nachrechnungen zur Verifizierung fortgeschrittener Rechenprogramme zur Schmelzenausbreitung verwendet.

TABLE OF CONTENTS

List of Figures

List of Tables

1 Introduction

1.1 Background

As one of the major tasks of the ECOSTAR project, large-scale experiments on melt spreading were performed. The experimental data were also used for a benchmark procedure to complete the validation of the advanced spreading codes, so that in combination with the validated codes, relevant information on melt spreading during accident conditions can be achieved. The interest for plant application is defined by the following subjects, which are realized in two large scale experiments:

- Investigation of "critical" flow conditions, namely spreading at reduced temperature and low flow rate of the melt, for which melt spreading is expected to be incomplete, that is stop of propagation of the melt front during release of the melt because of formation of a surface crust (experiment ECOKATS-1). This experiment is used as benchmark for code validation. It is evident that incomplete spreading should be avoided in an accident by design and/or by accident mitigation measurements.

- Investigation of complete and homogeneous spreading of a corium melt on a large concrete surface under anticipated representative conditions with high melt release rate and characteristic temperature of the melt near its liquidus temperature (experiment ECOKATS-2) [11].

To improve the quality of the planned spreading tests, especially with respect to the behaviour of the melt under transient conditions, an additional experiment was required:

- In a pre-test, the rheological behaviour of the oxide melt, which influences spreading and stop of the melt, has been estimated by a "standard" 1-d spreading experiment on inert ceramic substrate (experiment ECOKATS-V1).

The substrate, on which the melt was spread in experiment ECOKATS-1, was conventional structural concrete of the siliceous concrete type. Gas release, which occurred during the spreading process from concrete decomposition, did influence the spreading process and is part of the physical problem to be described.

In the original ECOSTAR work plan, the corium melt, which was planned to be used for the spreading tests, should have a representative concentration of UO_2. However, during the course of the project the use of UO_2 became impossible and finally Siempelkamp as the responsible contractor for these experiments left the project. Forschungszentrum Karlsruhe took over the experimental task with the modification, that the UO_2 based oxide melt would be replaced by a high temperature simulant melt, which is composed of Al_2O_3, SiO_2, CaO, and FeO and which can be produced by a modified thermite reaction, based on aluminium and iron-oxide. This composition was selected because of the wide and representative freezing range of the melt and the relatively reliable process of melt generation.. Furthermore, it was expected that for such a melt data for the most important physical properties would be available or could be measured.

After a series of pre-tests, which investigated the thermite burn of different initial compositions of thermite mixtures, and with assistance of thermo-chemical calculations, an optimized composition of a thermite generated oxide melt was selected. Obviously, the spreading process is especially sensitive on the freezing/solidification range and on the

1

viscosity of the melt. To improve the available property data of the selected melt for the benchmarking process, University of Würzburg [2] made an effort to measure the viscosity of the melt up to 1400 °C in a rotational viscometer. However, it turned out that, in contradiction to thermo-chemical calculations, even partial melting of the generated oxide could not be achieved until 1400°C,. Furthermore, this comparison emphasized that also for the expected corium melts substantial uncertainties of the physical data may exist, especially under fast cooling conditions, which may lead to chemical non-equilibrium during cool-down of the melt.

Consequently, conduct of the pre-test ECOKATS-V1 was found to be highly important to narrow the uncertainty range of the property data of the simulant melt.

The present report describes the experimental setup for the experiments ECOKATS-V1, and ECOKATS-1, the basic sequences of the tests and finally the results of both experiments. The physical and chemical data of the high temperature melt were determined as accurate as possible and are also reported, as they are necessary to understand the spreading behaviour and to perform blind post-test calculations with available computer codes.

1.2   Experimental Requirements

To perform the planned experiments ECOKATS-V1, and -1 the test facility and the required measuring equipment had to be designed, new parts were supplied, and all components had to be assembled and tested. The main components were (1) thermite crucible, which must be able to generate and to release the large mass of thermite melt, with controlled opening of the melt release valve and a reliable weighing system, (2) whirl basin, and (3) extensively instrumented spreading device to which the melt was released.

Of primary importance were the selection, the characterisation, and the testing of the simulant melt based on the "conventional" thermite reaction with addition of further oxides. The performed investigations are reported below.

2   1-D Pre-Test ECOKATS-V1

2.1   Description of the Experiment

The experiment ECOKATS-V1 was designed as a 1-d spreading test for the simulant oxide melt on ceramic substrate. **Figure 2-1** gives the arrangement of the thermite crucible, whirl basin, and of the spreading channel, which was 293 mm wide and 8 m long, with an open end to allow outflow of the melt in case of extreme horizontal spreading. The spreading channel was formed by a U-shaped support structure of siliceous concrete and a cordierite ceramic bottom liner embedded on a layer of sand (**Figure 2-2**). The cordierite plates were carefully levelled to be exactly horizontal, with deviations from the horizontal less than 1 mm. The sidewalls of the spreading channel were made of concrete. The volume of the whirl basin up to the spreading level was 15.98 litres. **Figure 2-2** shows the positions of W-Re thermocouples to measure the temperature of the melt in the whirl basin, indicated by the signatures WOPLW1 - 3. No thermocouples were located in the spreading channel. **Figure 2-3** and **Figure 2-4** illustrate the test set-up.

For the simulant melt, the optimal thermite mixture has been investigated by several small pre-tests described in [1]. The composition of the thermite mix which was loaded in the thermite tank and the generated oxide melt used in ECOKATS-V1 is given in **Table 2-1**. The metal melt fraction, which makes 26.5 % of the mixture or 79.4 kg of Fe, is not listed. This metal melt has a higher density than the oxide melt and is therefore retained in the whirl basin.

Table 2-1: Mix of thermite powder and generated oxide melt composition for experiment ECOKATS-V1

Thermite Mixture		Oxide Melt	
Constituent	Mass	Constituent	Part
Aluminium Thermite	189.74 kg	Al_2O_3	41 %
CaO	46.31 kg	FeO	24 %
SiO_2	33.08 kg	CaO	19 %
Fe_2O_3	30.87 kg	SiO_2	16 %
Total	**300.00 kg**	**Total**	**100 %**

The thermite powder was loaded and coarsely mixed in the thermite vessel and electrical igniters were placed in the upper powder layer. To increase the temperature of the generated melt, the powder was preheated in the vessel to 100 °C by electrical heaters for more than 12 hours.

The following measurements were taken during the test:

- Mass of the thermite reaction vessel by load cells; gives melt flow rate, transition from metal to oxide, and total melt mass.

- Thermocouples in the whirl basin, give the temperatures of metal and oxide melt during their release.

- Video registration with different systems delivers information about the release and the spreading process.
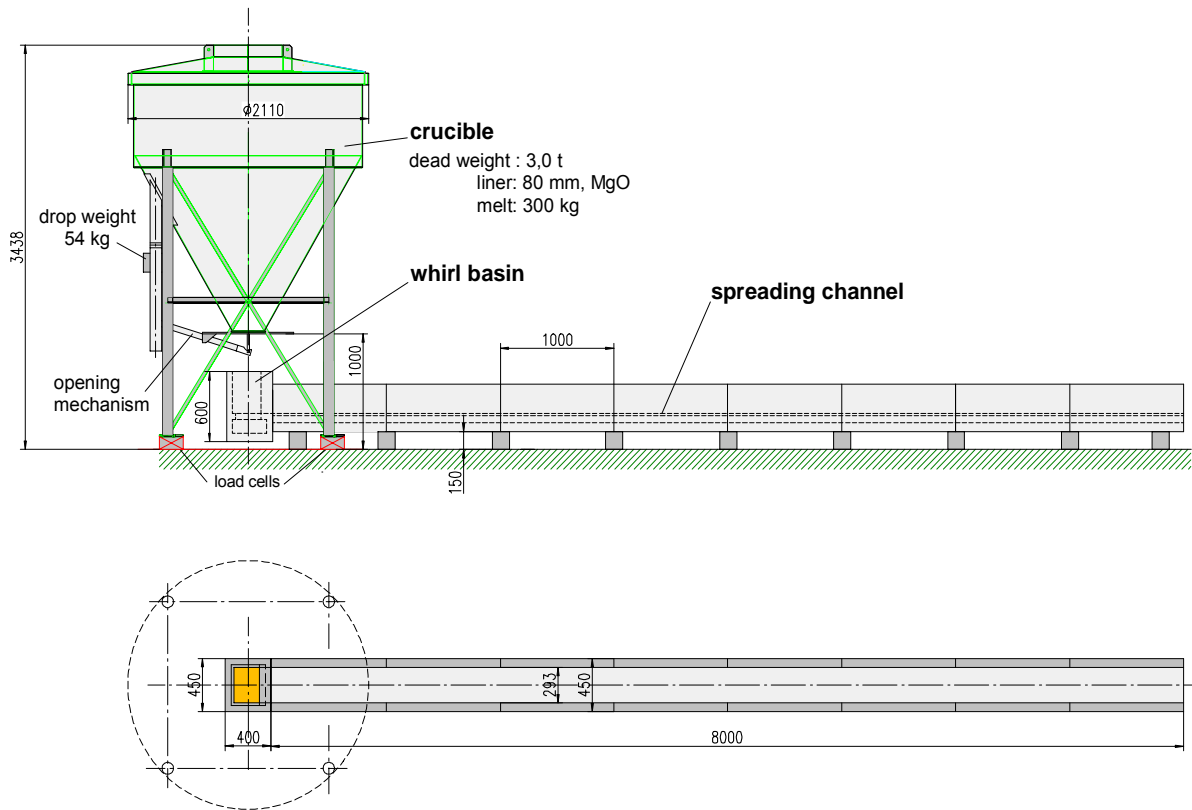
Figure 2-1: Arrangement of crucible and spreading channel for experiment ECOKATS-V1
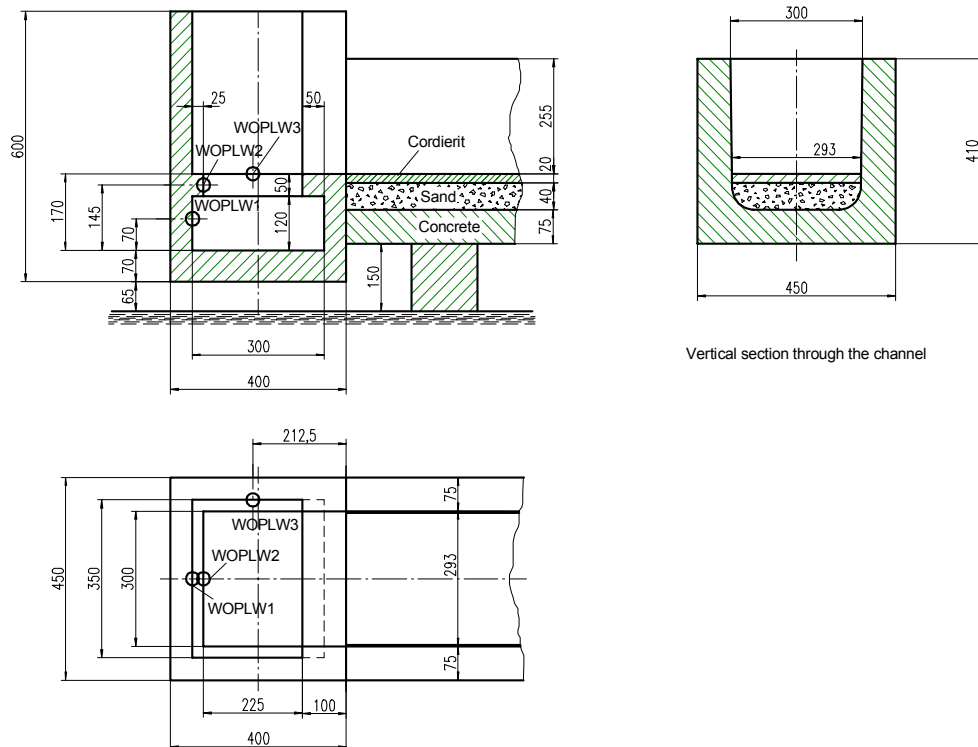
Figure 2-2: Design of whirl basin and spreading channel of the experiment ECOKATS-V1

Figure 2-3: Thermite reaction vessel and view into the whirl basin in ECOKATS-V1

Figure 2-4: Front view and side view of the spreading channel of ECOKATS-V1

2.2 Experimental Results

2.2.1 Test Procedure

The realized experimental process of the ECOKATS-V1 experiment is provided in **Table 2-2**. After completion of the test preparation, the thermite powder was ignited 120 s before start of the melt pour.

Table 2-2: Realized process of the experiment ECOKATS-V1

Time	Rel. Time [s]	Event
11:25:00	-180.0	data acquisition started and operating
11:26:00	-120.0	ignition of thermite
11:27:18	-42.0	thermite burn ends
11:28:00	0.0	opening of the nozzle of thermite vessel
11:28:01.5	1.5	start of melt release from thermite vessel
11:28:17	16.8	end of metal and start of oxide outflow
11:28:22	22.0	melt enters spreading channel, start of melt spreading
11:28:50	50.0	first stop of the floating melt crust at 3.4 m
11:29:07	67.0	second stop of the floating melt crust at 4.7 m
11:29:17	76.8	melt pour ended
11:29:34	92.0	third stop of the floating melt crust at 6.2 m
11.30.27	147.0	end of slow residual spreading at 6.5 m

Two minutes after ignition, the thermite burn was complete and the metal and oxide fractions were separated, metal at the bottom, oxide on top. Pour of the melt was started by opening the nozzle at the bottom of the vessel at time 0. The heavier iron fraction of the melt was released first from 1.5 to 16.8 s, and filled the lower part of the whirl basin. The subsequent oxide release led to the overflow of the whirl basin at 22 s, and the oxide melt entered the spreading channel with no horizontal momentum from the pouring process. Melt release from the thermite vessel ended at 76.8 s. A total outflow of 295 kg of melt was determined (79 kg metal and 216 kg oxide). The main characteristics of the melt as generated in the thermite crucible are given in **Table 2-3**.

Table 2-3: Characteristics of the melt in ECOKATS-V1

Parameter	planned	realized	outflow from crucible
total mass of mixed thermite	300 kg	300 kg	295 kg [1]
preheating of thermite mixture	100°C	100°C	
metal fraction generated	80 kg	80 kg	79 kg [2]
oxide fraction generated	220 kg	220 kg	216 kg
initial temperature of melt	1590°C	1620°C [3]	1620°C [3]
initial rate of oxide outflow	2 litre/s		1.36 litre/s
duration of oxide melt release	41 s		60 s

[1] the missing 5 kg oxide formed a film on the inner wall of the thermite crucible
[2] weighed solid metal regulus in the whirl basin
[3] TC measurement in the whirl basin

Figure 2-5 gives the measured mass of the thermite vessel during outflow of the melt (dashed line) with some unavoidable disturbances. From this curve the equivalent mass flow into the whirl basin during the spreading period from 22 s (start of spreading) to 76.7 s (end of outflow) was derived by approximation through linear time intervals in **Table 2-4**. In this table, the time zero is the start of spreading at 22s. The solid curve in **Figure 2-5** is the calculated oxide outflow derived by the formula of Torricelli, considering the real geometry of the thermite vessel. The result is in good agreement with the measurements, thus confirming that the melt outflow process was performed as expected.

The experimental conditions for the experiment ECOKATS-V1 are summarized in **Table 2-5** and in [5].
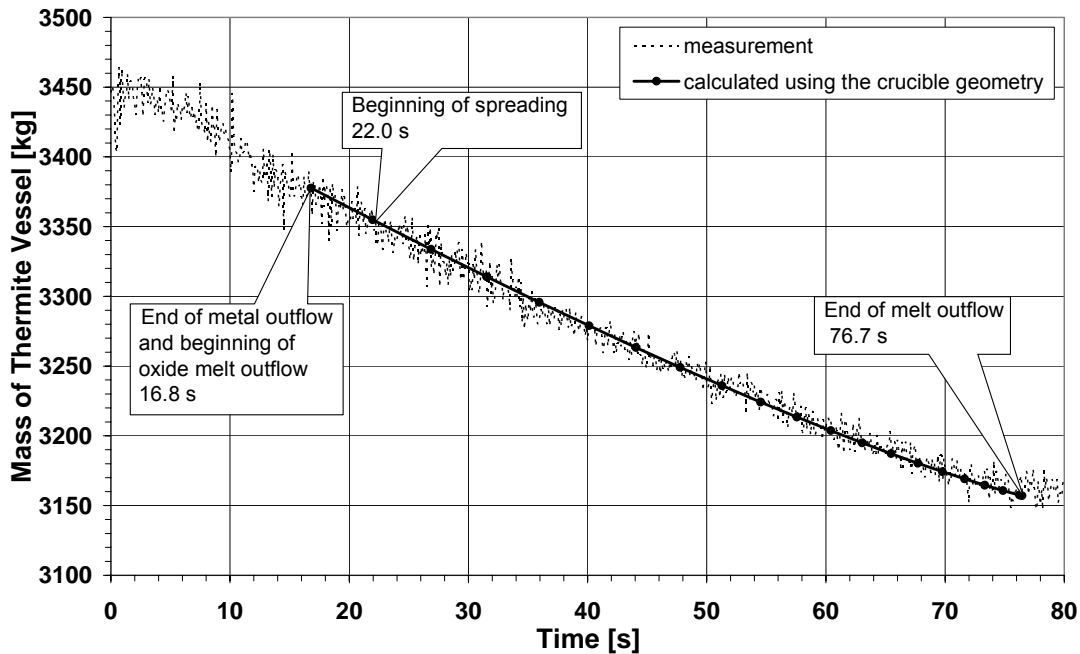
Figure 2-5: Mass of thermite vessel during outflow of the melt in ECOKATS-V1

Table 2-4: Stepwise constant mass flow of the melt in ECOKATS-V1

Time [s]	Mass flow [kg/s]
[0, 13.7]	4.2375
(13.7, 40.5]	3.4629
(40.5, 47.6]	3.2909
(47.6, 54.7]	2.61
t > 54.7	0

Table 2-5: Conditions during spreading of the melt in ECOKATS-V1

Parameter	ECOKATS-V1
Initial temperature of the melt	1620°C/1893 K
Initial flow rate of the melt	1.3 litre/s
Duration of melt pour to surface	54.7 s
Spread melt mass	193 kg
Spreading surface	Cordierite (inert ceramic)
B x L	0.293 m x 8.0 m
Melting temperature	1893 K – 1923 K

2.2.2 Temperature of the melt at start of spreading

To measure the temperature of the melt at the start of spreading, three W-Re thermo-couples, WOPLW1, WOPLW2, and WOPLW3, were installed in the whirl basin below the crucible at elevations of 70, 145 and 170 mm above the bottom of the whirl basin. As it is shown in **Figure 2-2,** this part of the test facility is very similar to the corresponding arrangement in ECOKATS 1. The measured signals of the three thermocouples are given in **Figure 2-6**. The first temperature rise is controlled by the radiation from the melt jet and melt surface. Direct contact with the melt results in a sharp increase of the measured signals at 10 s, 17.5 s, and 20 s, respectively, in correspondence with the different locations of the thermocouples. However, some splashed material obviously contacted the sensor WOPLW2, 12 s already before the melt level reached the sensor. However, this has no influence on the measured temperature of the spreading melt, which is consistently measured by the two thermocouples WOPLW1 and WOPLW2 after 23 s to be about 1620°C. These thermocouples are located in the metal phase of the generated melt, which is retained in the whirl basin and give a reliable signal with fast response. Therefore, the actual temperature of the melt entering the spreading surface by overflow of the whirl pool at 22 s is 1620°C.

The third thermocouple WOPLW3, positioned at the uppermost level, only contacted the oxide melt, which covered the heavier metal melt. This thermocouple gives a temperature that is 300 K lower than expected, which is probably due to some oxide crust which encapsulated the sensor. It is well known, that this type of sensors tends to measure lower temperatures for oxide melts.
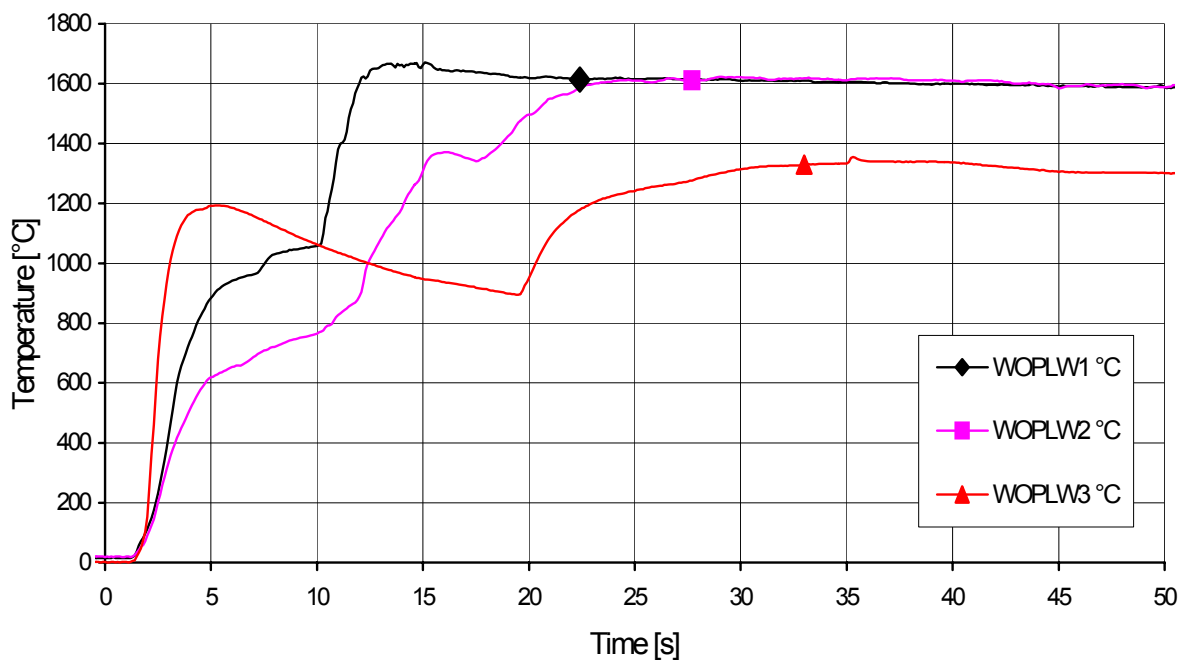
Figure 2-6: Temperature measurements in the whirl basin of ECOKATS-V1

2.2.3 Spreading of the Melt

The spreading behaviour, which is characterized by motion of the melt front, was determined from the records of the video and CMOS cameras. For this purpose a line raster with a 10 cm pitch was marked on the spreading surface. Since the conventional video cameras tend to fade-out due to the sudden rise of the luminosity, the main task of the CMOS camera was to monitor the initiation of spreading. The CMOS camera was provided by Becker Technologies and positioned in such a way that the channel entrance from 0 m to 1.5 m, i.e. over the first 7 s of front propagation, could be observed. **Figure 2-7** shows one picture of the early spreading process at the channel length of 1.0 m (4 s) which was taken with the CMOS camera. For the whole spreading channel two conventional video cameras were installed by FZK, each for one half of the channel.
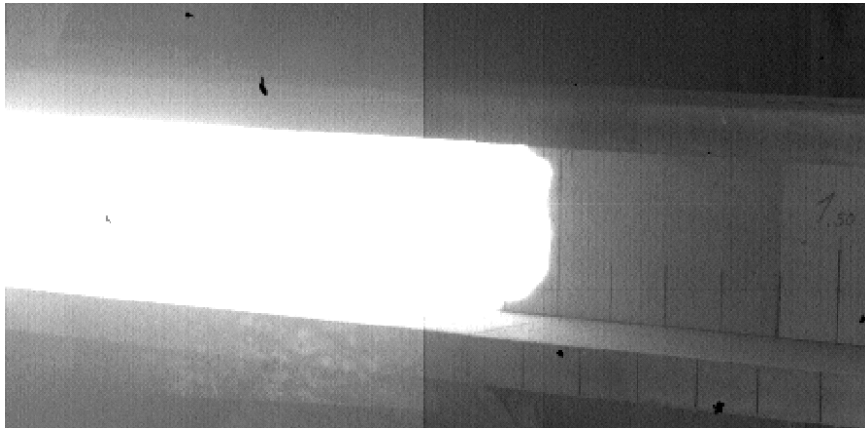
Figure 2-7: Oxide melt during spreading in ECOKATS-V1, melt flows from left to right

Evaluation of the video recordings results in the spreading characteristic. This is shown in **Figure 2-8**. Time zero is set to the start of spreading, which corresponds to 22 s after the melt tapping.
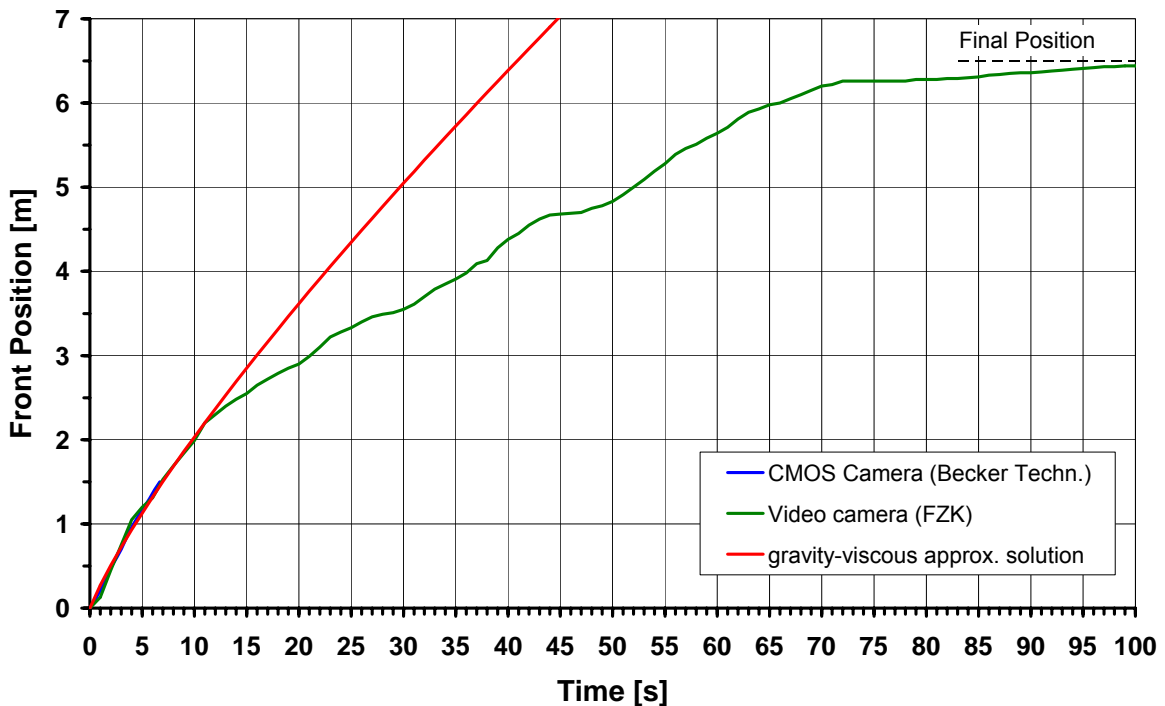
Figure 2-8: Time behaviour of the melt front position in ECOKATS-V1

Spreading of the melt was quiet and smooth. Because of the ceramic substrate, no production of gases was observed which would have perturbed the motion of the melt. During the first 12 s, spreading was not influenced by any crust formation. Afterwards, a thin floating surface crust was formed, which delayed the spreading process and led to a temporary stop of the melt front when the crust anchored to the sidewalls. This occurred first at the distance of 3.4 m at 28 s, as shown in **Figure 2-8**. Immediately after the stop of the melt crust, hot melt material penetrated under the crust and a new front of the spreading melt was formed, propagating nearly isothermally with a bulk viscosity of about 1.12 Pa s (**Figure 2-9**). The same process of crust anchoring and transient melt stop was observed at the distance of 4.7 m at 45 s, and finally near the end of the spreading at 6.2 m after 70 s, that is 15 s after the end of melt release, which occurred at 55 s. Slow melt front propagation continued until 147 s by release of a small mass of residual hot melt under the anchored crust, moving the melt front to its final position at 6.5 m.
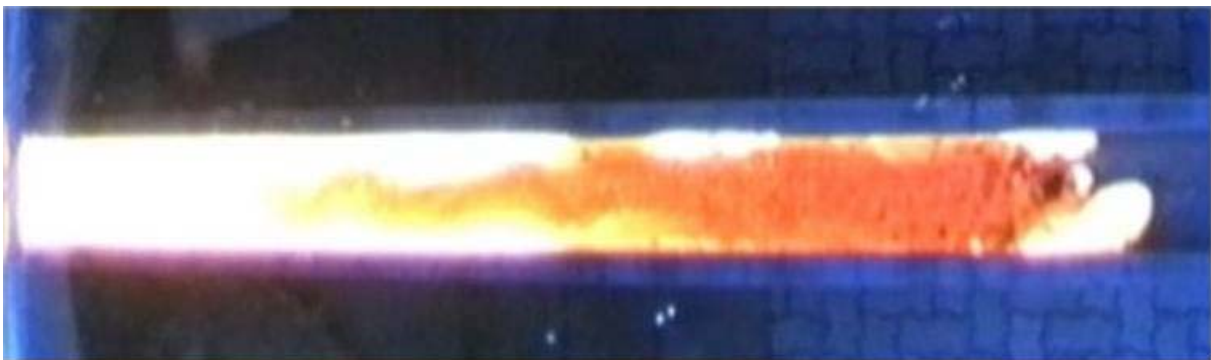
Figure 2-9: Continuation of spreading after transient stop by anchored surface crust at 3.4 m
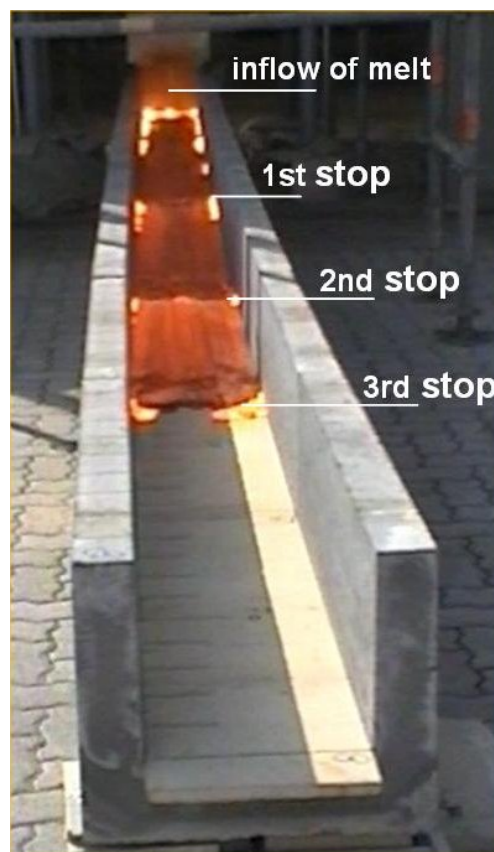
Figure 2-10: Melt at the end of spreading showing 3 zones of anchored crusts

10

Figure 2-10 shows the spread melt almost at the end of the spreading process. The 3 locations where the crust anchored to the channel walls and the melt penetrated under the crust are marked. They are characterized by the transition from the dark crust to the brighter melt/crust.

In **Figure 2-8**, a comparison is included with the theoretical approximation of the melt motion which is valid for the first phase of the spreading process from 0 to 12 s. During this period, spreading is dominated by gravity and viscous forces only, and the influence of inertia and of crust formation can be neglected. Therefore, the approximate self-similar solution for the melt front motion is applied [6]. This includes estimation of the melt viscosity to 0.2 Pa s. This viscosity is valid for the melt at temperatures near 1600 °C, before onset of solidification, and is in the expected range of a multi-component oxide melt with the composition of **Table 2-1**. Determination of the melt viscosity is an important contribution to characterize the physical properties of the melt for further theoretical analysis, as the temperature of the melt was too high to measure the viscosity of the melt by high temperature viscometers. Further property data of the melt are given in section 3.2.6.

Figure 2-11 shows the melt front velocity from 0 to 80 s, derived from the measured data in **Figure 2-8**. The strong scattering of the velocity is a normal result of differentiating the measured front position with minor fluctuations, for which no filtering or smoothing has been applied. The initial front velocity of 0.3 m/s decreases to less than 0.1 m/s at 12 s. From there the velocity decreases to about 0.5 m/s at 70 s. Three temporary stops are visible at 28 s, 45 s, and 72 s, followed by continuation of the spreading process.
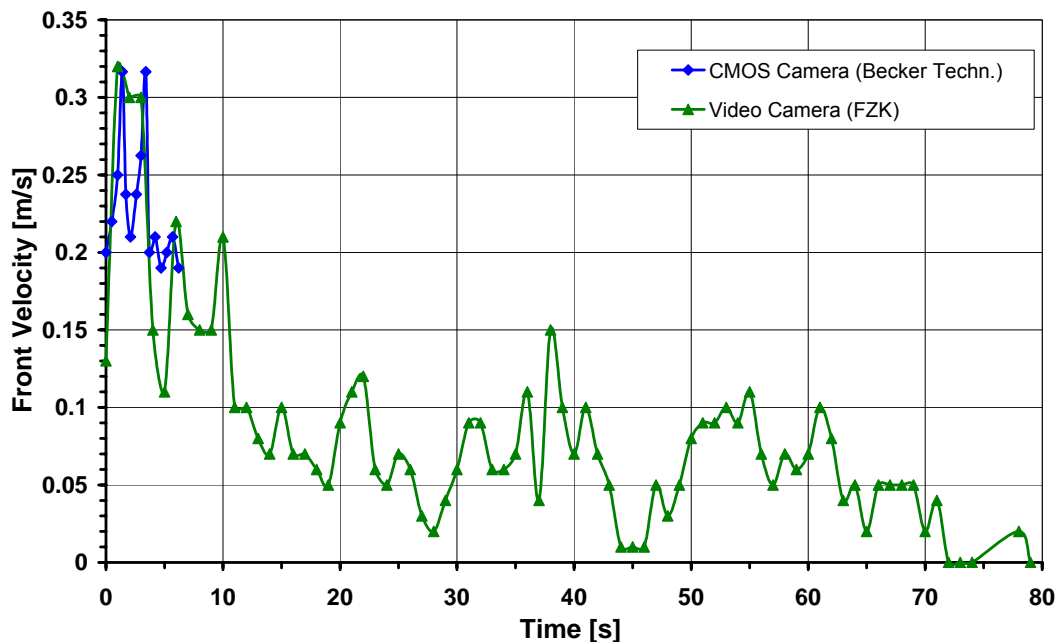
Figure 2-11: Melt front velocity of the spreading process in ECOKATS-V1

Figure 2-12 shows a good agreement between the measured melt front velocity and the theoretical approximation of the gravity-viscous solution during the first time period of 12 s.
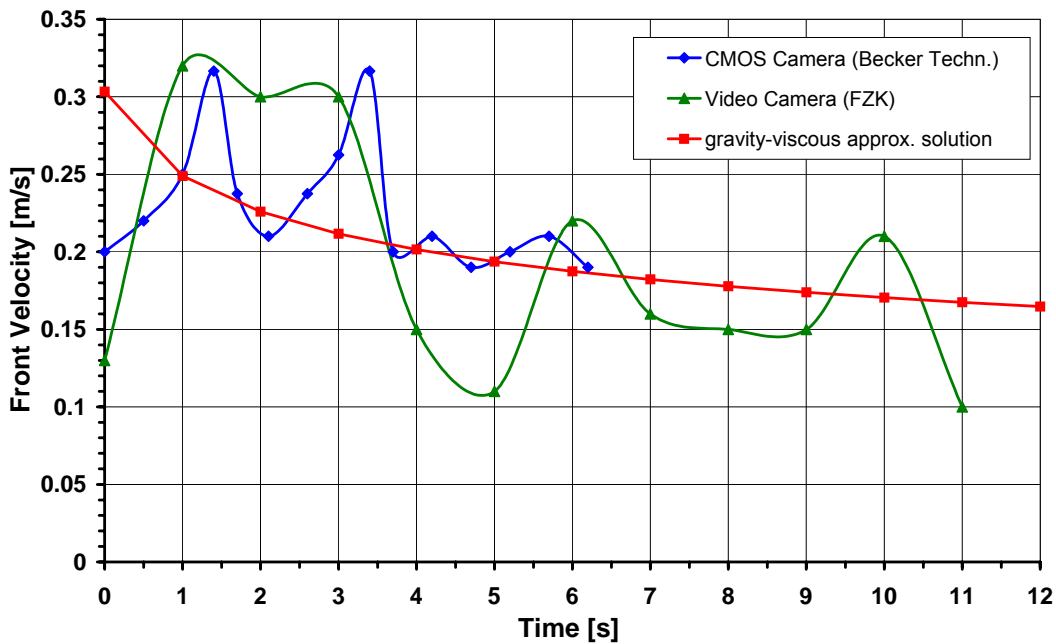
Figure 2-12: Initial velocity of the melt front in ECOKATS-V1

Figure 2-13 and **Figure 2-14** are photographs of the spread melt during spreading and after complete solidification. **Figure 2-15** shows the crust surface at the positions of the melt stops, where the surface has a higher roughness than elsewhere.

The highest thickness of the solidified melt was determined to be 77 mm at the entrance of the spreading channel over the distance of 0.37 m (**Figure 2-14**). The end of the spread melt is thinner than elsewhere and is characterized by the crust at 6.2 m and some minor melt mass that slowly penetrated under the crust to 6.5 m (**Figure 2-15**). In **Table 2-6** the average thickness of the solidified melt is given in dependence of the spreading length.

Table 2-6: Average thickness of the solidified melt in ECOKATS-V1

Spread length [m]	Average thickness [mm]
0 – 0.37	77)[1]
0.37 – 1.25	50
1.25 – 1.50	52)[1]
1.50 – 3.20	45
3.20 – 3.60	64)[1]
3.60 – 4.80	36
4.80 – 5.20	53)[1]
5.20 – 5.90	35
5.90 – 6.05	34
6.05 – 6.50	14

)[1] Local elevations

Figure 2-13: Total spread oxide melt in ECOKATS-V1

Figure 2-14: Spread oxide melt near the whirl basin in ECOKATS-V1

Position at 3.4 m   Position at 4.7 m

End of spreading near 6.5 m

Figure 2-15: Surface of solidified oxide melt in ECOKATS-V1 at different positions

3   2-D Spreading Experiment ECOKATS-1

3.1   Description of the Experiment

3.1.1 Main Test Parameters

The experiment ECOKATS-1 was designed as a large-scale spreading test of an oxide melt on a horizontal surface for the purpose of code validation. To fulfil these requirements, the following objectives had to be considered:
- Flow rate and initial temperature of the melt should be sufficiently low, so that stop of the melt front occurs during release of the melt on the large spreading surface before contact with the walls ("critical" flow conditions)
- The spreading surface had to be fabricated from siliceous concrete to represent the conditions of the basement in a nuclear plant.

Using the estimated property data of the simulant melt as described in [1], design calculations of the spreading codes confirmed, that a spreading surface 4 m long and 3 m wide would be adequate to allow undisturbed spreading of 600 kg oxide melt. At the time of test preparation, the density of the melt was only tentatively known ($\rho \sim 2700$ kg/m^3) and a corresponding oxide melt volume of 220 litres was estimated. Because of the higher density of the oxide melt due to the high content of FeO, which was determined later ($\rho = 3263$ kg/m^3) the melt volume was about 184 litres only.

The experimental installation of ECOKATS-1 consisted of the thermite crucible, the whirl basin, and the spreading surface (**Figure 3-1**). The horizontal spreading device consists of a 2.6 m long supply channel that ends on the 3 m by 4 m rectangular surface. Registration of the weight of the thermite vessel during melt release, which was well-proven in the test ECOKATS-V1, was also in operation.

The support structure for the spreading area was made up of a suspension system consisting of 4 support legs and 2 cross girders (**Figure 3-1** and **Figure 3-2**). For a redundant determination of the spread melt mass, the spreading surface was suspended on 4 load cells to determine the weight increase during release of the melt. This new technique was also tested for its future use in ECOKATS-2.

Along the way of the spreading melt, several thermocouples for temperature measurements were provided, two inside the supply channel and many in the spreading area in different positions from the upper concrete surface. They allowed registration of the temperature response of the concrete and of downward melt penetration.

For the video observation cross marks were drawn over the whole spreading surface which form a grid of 20 by 20 cm.

Figure 3-2 shows different views of the test assembly.
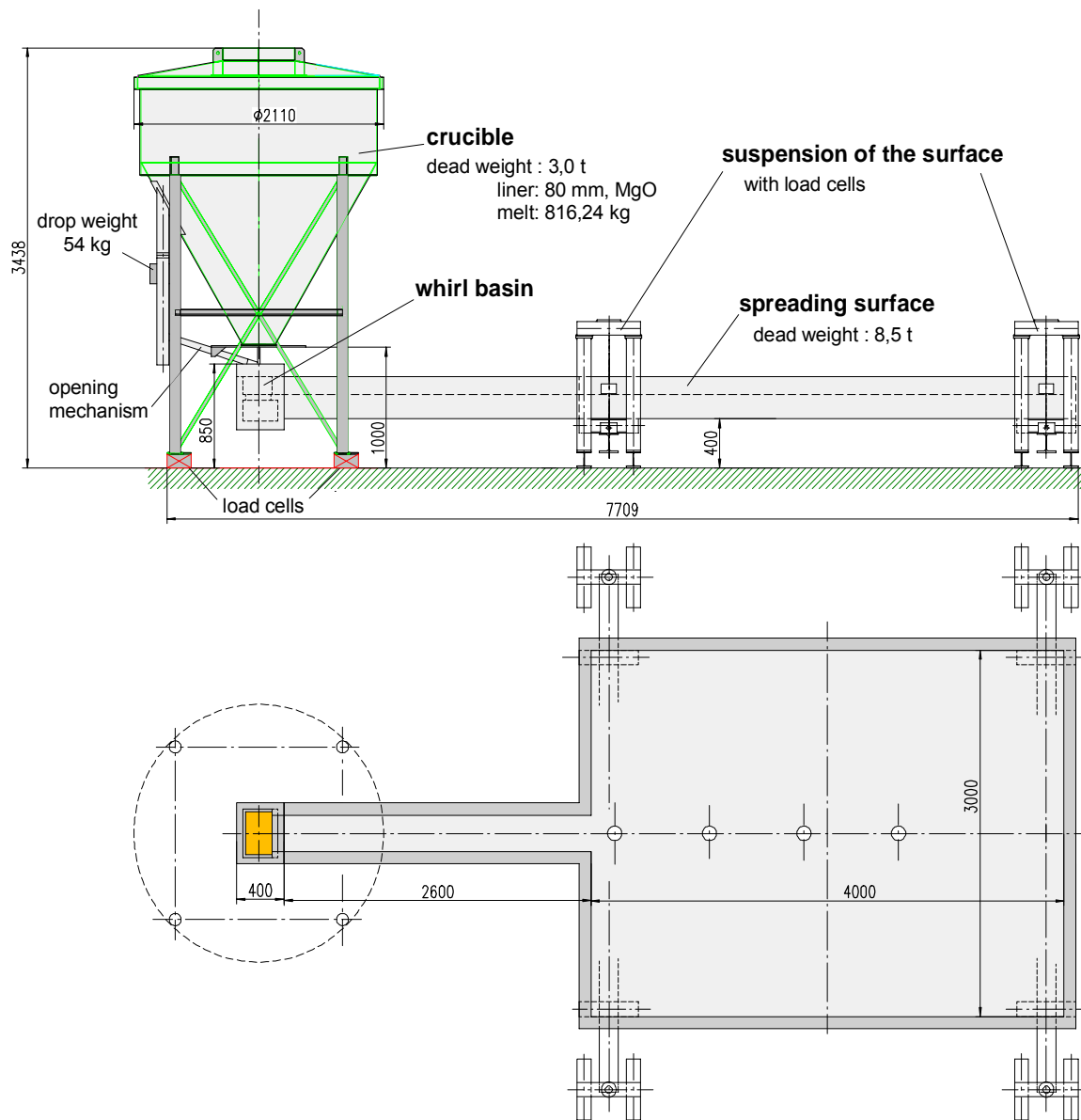
Figure 3-1: Arrangement of crucible, whirl basin, and spreading surface in ECOKATS-1

The planned sequence of the experiment was as follows:

- Ignition of the thermite mix in the crucible
- After 2 min for completion of the thermite reaction and separation of the heavier metal phase and the lighter oxide phase: Start of melt release by opening of the release nozzle at the bottom of the thermite crucible (time 0 s).
- Release of the melt, metal first, into the whirl basin. The metal fraction is retained in the lower basin. By overflow of the whirl basin, the oxide melt flows through the horizontal supply channel to the spreading surface.

The initial 1-d flow of the melt in the supply channel is used to characterize the linear spreading process under the influence of concrete decomposition and can be directly compared to the spreading process in experiment ECOKATS-V1 on an inert ceramic substrate.

Transport of the large spreading device,
view from bottom.

Suspension of the spreading area
with load cells

Test configuration ECOKATS-1,
crucible in the background

Outlet of thermite vessel, whirl basin,
channel and spreading surface

Test configuration ECOKATS-1 with scaffold
for video observation, front view

Test configuration ECOKATS-1 with scaffold
for video observation, side view

Figure 3-2: Assembly of the test ECOKATS-1

3.1.2 Melt Generation in the Thermite Crucible

The mass of the oxide melt to be spread on the large surface was increased from 300 kg, which were originally specified in the ECOSTAR work package, to 600 kg, to give a more representative spreading test. Preparation of the melt was in accordance with the specifications of Table 2 in [1]. The composition of the thermite mix which was loaded to the thermite tank is given in **Table 3-1**. The table also shows the constituents of the oxide melt generated by the thermite reaction. Not listed is the metal part of the melt which makes 26.5 % of the mixture or 216.3 kg of Fe and which is retained in the whirl basin.

Table 3-1: Mix of thermite powder and generated oxide melt composition for experiment ECOKATS-1

Thermite Mixture		Oxide Melt	
Constituent	**Mass**	**Constituent**	**Mass%**
Aluminium Thermite	516.24 kg	Al_2O_3	41 %
CaO	126.00 kg	FeO	24 %
SiO_2	90.00 kg	CaO	19 %
Fe_2O_3	84.00 kg	SiO_2	16 %
Total	**816.24 kg**	**Total**	**100 %**

The mixture of thermite powder was preheated in the crucible to 100° C for more than 18 hours to give a higher initial temperature of the melt. To start the chemical reaction, 3 electrical igniters were placed in the upper powder layer. The necessary time to complete the thermite burn and to allow separation of the heavier steel phase and the lighter oxide phase was about 2 minutes.

3.1.3 Spreading Area

The spreading area with the attached whirl basin is shown in **Figure 3-3**. The spreading area was fabricated as a single element of reinforced siliceous concrete. The rectangular spreading surface was 3 m wide, 4 m long and had even horizontal surface. The thickness of the bottom plate was 0.20 m. The surface was surrounded with a concrete wall 0.10 m wide and 0.15 m high. The supply channel, 0.288 m wide and 2.60 m long, was located in the middle of one short side. To obtain the specified quality of industrial concrete the minimum curing time of 28 days was kept.

The whirl basin was designed for undisturbed supply of the melt to the spreading surface. Its retention volume of 33.5 litres corresponds to the metallic melt and a minor quantity of oxide (**Figure 3-4**). It was fabricated from a steel case and coated with a ceramic liner. It was directly mounted to the supply channel, hence its mass was weighted together with the spreading device.

To measure the temperature of the incoming melt and the response and downward erosion of the concrete surface, 4 instrumentation modules with various thermocouples were integrated in the spreading device in line with the supply channel at selected measurement positions as shown in **Figure 3-4**. The modules were produced with complete wiring as separate plugs of concrete with a diameter of 120 mm and were inserted after fabrication flush with the inner surface. Detailed description of the modules is given in section 3.1.6.

18
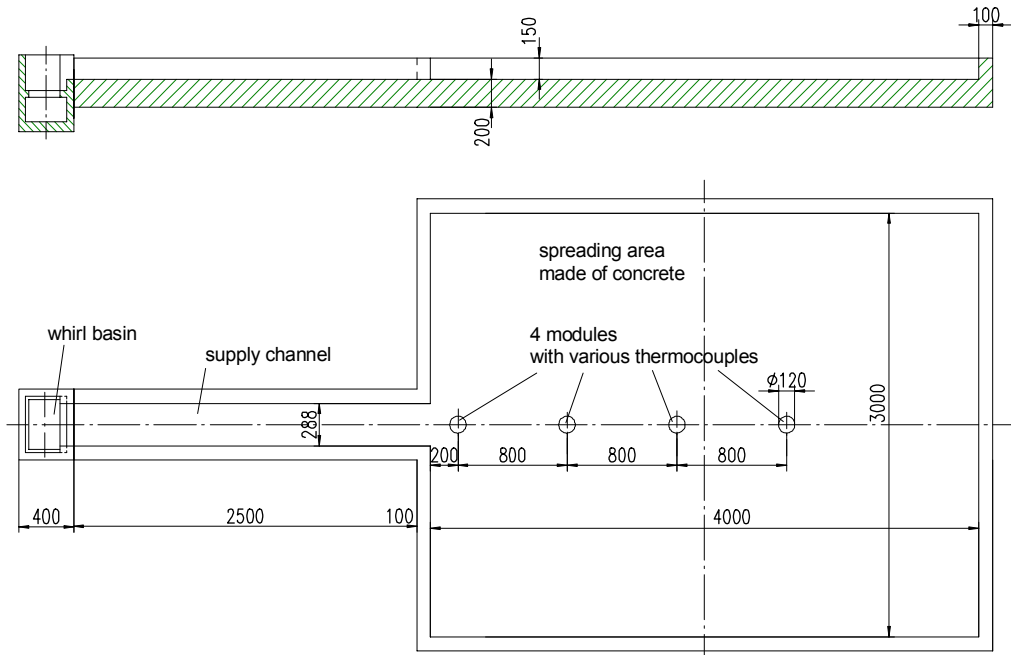
Figure 3-3: Spreading surface made of concrete with attached whirl basin for ECOKATS-1
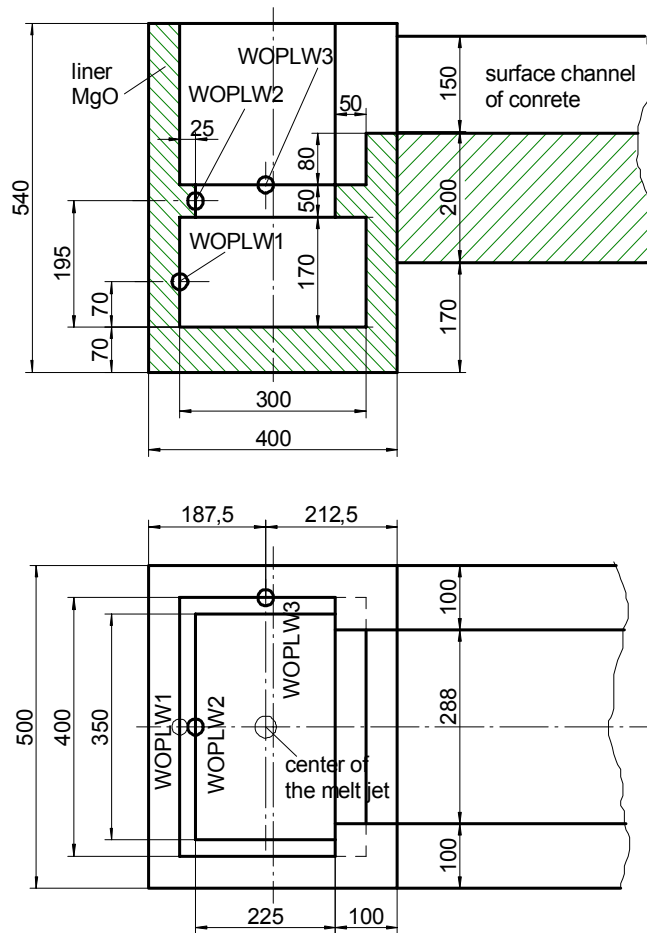
Figure 3-4: Geometry and instrumentation of the whirl basin in ECOKATS-1

19

3.1.4 Composition of the Concrete

The siliceous concrete of the spreading area was fabricated with the following specification:

Material	Mass per m^3
Water	190 kg
Cement CEM III/B 32,5 NWHS	350 kg
SiO$_2$ sand & aggregates (Rheinkies) with:	1783 kg
Sand 0 – 2 mm	35 %
Sand 2 – 8 mm	15 %
Gravel 8 – 16 mm	25 %
Gravel 16 – 32 mm	25 %

Its density is $\rho = 2323$ kg /m^3.

As this composition has only minor deviations from the standard concrete composition e.g. of the previous BETA experiments, its decomposition enthalpy can be assumed as $\Delta h = 2.1$ MJ/kg.

3.1.5 Pour of the Melt

Pour of the melt took place through a nozzle at the bottom of the thermite crucible. The nozzle had an opening diameter of 34 mm to allow initial flow rate of about 2.4 l/s, see **Figure 3-5**. Time zero is defined by the electrical signal that leads to mechanical opening of the nozzle.

At first, the heavier iron fraction of the melt poured out into the whirl basin underneath the crucible, and then the light oxide melt followed. After filling the whirl basin to 300 mm, the melt entered the supply channel and spread onto the spreading surface. No major horizontal momentum was generated by the use of the whirl basin.
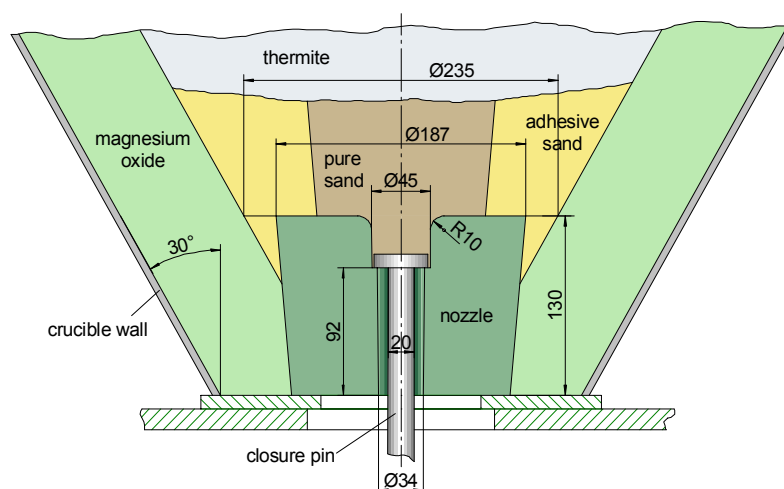
Figure 3-5: Geometry of the nozzle to release the melt

3.1.6 Instrumentation

The ECOKATS-1 facility was equipped with load cells, thermocouples, video and infrared cameras. Declarations of the sensor encodings and the sensor locations are given in the instrumentation plan in the Appendix and in **Figure 3-2** and **Figure 3-6**. The cameras and the crucible instrumentation are not shown in the figures.

Mass of Thermite Vessel
As shown in **Figure 3-1**, the thermite crucible was positioned on 4 load cells to determine the total mass and the melt release during the experiment. Each load cell had a maximum capacity of 4700 kg with an error less than 0.05% and with the sensitivity of 2.85 mV/V ±0.1 %. The signal of each load cell was given to an electrical summing element, which delivered the analog signal of the total crucible weight. The sum signal was fed to an amplifier, which raised the measured signal to a maximum output value of +10 V.

Because of the measuring range of about 4000 kg for the loaded crucible, the amplifier was configured such that a maximum weight of 5000 kg yielded the maximum output of +10 V. The measured load signal of the thermite crucible was defined as LOAD00.

Temperature of the Poured Melt and of the Spreading Surface Melt
The initial temperature of the melt as released from the thermite vessel was measured in the whirl basin with 3 W-Re thermocouples WOPLW1, WOPLW2 and WOPLW3 (W-Re plunging type). Locations of these thermocouples are shown in **Figure 3-4**.

Temperature measurement of the melt during spreading started at the entrance of the supply channel with the thermocouples NIMAC1 (Ni-CrNi mantle type) and WOPLC1 (W-Re plunging type) as shown in **Figure 3-6**. At a distance of 1.5 m from the entrance, the thermocouple WOPLC2 (W-Re plunging type) was placed. The active junctions of these thermocouples were located 10 mm above the concrete surface.

Four thermocouple modules 1 to 4 were mounted in the spreading surface (**Figure 3-6**). The modules consist of a vertical concrete cylinder, mounted flush with the spreading surface, with different thermocouple instrumentation. As shown in **Figure 3-7** and **Figure 3-8**, each of the 4 modules was equipped with a rake of 4 staggered thermocouples NIWlmi (Ni-CrNi wire type), embedded in the concrete. They measured the temperature of the concrete and the possible propagation of the melt into the concrete. The first thermocouple of the rake was flush with the concrete surface. The following 3 thermocouples were 2 mm apart each. The tip of the Ni-CrNi- thermocouples was inclined 10° from the horizontal concrete surface to avoid as far as possible, heat losses by heat conduction through the thermocouple material. The temperature of the spreading melt was measured by thermocouple WOPLm1 (W-Re plunging type), located 5 mm above the concrete surface and protruding into the melt. In addition, modules 1 and 3 were instrumented with one W-Re thermocouple with Ta sheath (WOMAm1), 6 mm above the concrete surface, for a redundant temperature measurement of the spreading melt.

Furthermore, the temperature of the environment is measured at several positions with the sensors RTEM01-RTEM03.
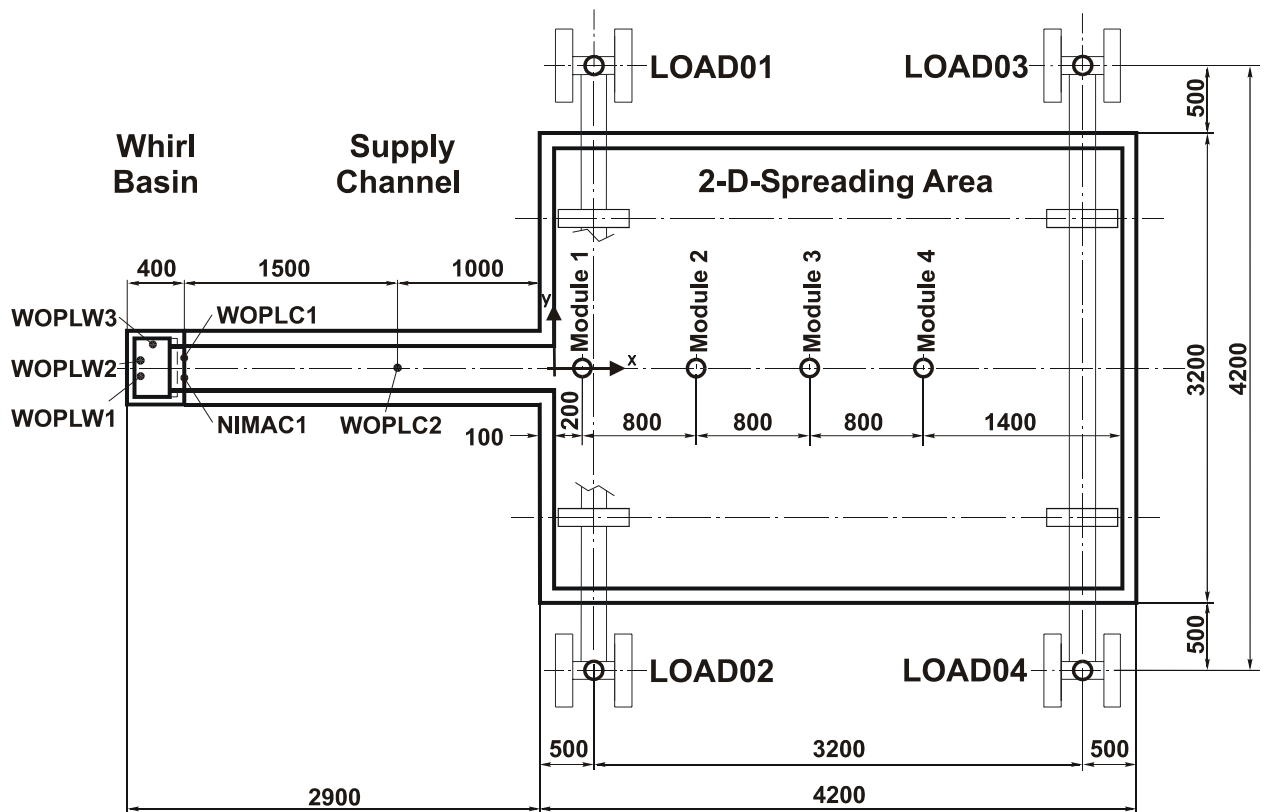
Figure 3-6: Instrumentation of the spreading area for ECOKATS-1
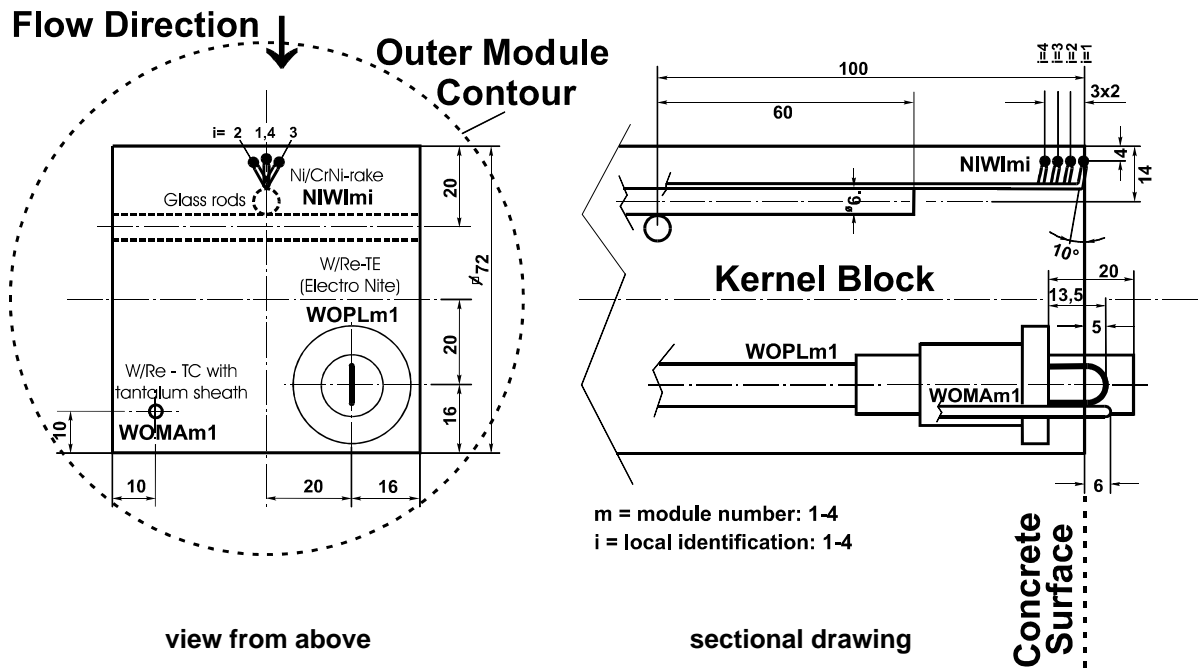
Figure 3-7: Detail of the thermocouple modules used in ECOKATS-1
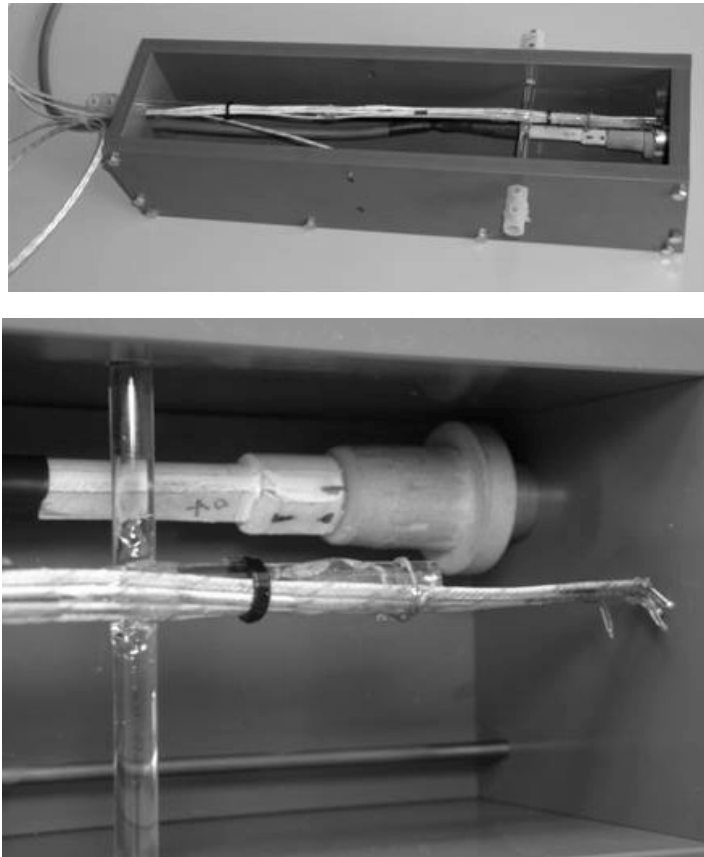
Figure 3-8: Thermocouple modules: Thermocouples in the mould prior to filling the concrete

Mass of Spreading Melt Area during Spreading of the Melt

The steel support of the spreading area was made up of a suspension system with 4 support legs as shown in **Figure 3-1** and **Figure 3-2**. The legs were prepared with the load cells LOAD01 – LOAD04 to measure the total weight of the spreading area and hence the resultant weight of the supplied melt.

Each load cell had a maximum capacity of 50 kN with an error less than 0,04 % and sensitivity of 2 mV/V ±0,1 %. Each load signal was processed by an instrumentation amplifier, which raised the measured signal to a higher output value. Thus the maximum load signal of 50 kN yielded a maximum output signal of +10 V.

3.1.7 Data Acquisition

The data recording was done by an application program under LabWindows (National Instruments, Version 2.3.1). The implementation provided for a maximum of 128 input channels. For the actual application, about 40 channels were sufficient for all installed sensors. The recording system provided a time base by setting a time mark to all measured signals. In addition to the sensor signals, the control voltage to open the outlet nozzle has been registered as time mark for start of the melt pour.

With the cycle frequency of 10 Hz and the maximum recording time of 1 hour, the total capacity of the required memory was some 6 Mbytes.

23

The instrumentation plan with all implemented sensors is given in the Appendix. Three I/O submodules (5001) from Analog Devices with 16 amplifiers on each module were available primarily for processing the signals of the thermocouples. All load cells were prepared with special bridge amplifiers, as mentioned in section 3.1.6.

For the data transfer to the recording PC, four multiplexer units SCXI from National Instruments with 32 input channels per unit were available, from which only 2 multiplexer units were used for the actual experiment.

3.1.8 Camera Observation

Video Camera

For observation of the experiment, 5 conventional colour video cameras with a frame rate of 25 Hz were installed by FZK. Two cameras were behind the crucible: One to monitor the head of the thermite crucible during the reaction phase and one to observe the mechanism for opening of the release nozzle. Three cameras registered the spreading surface: one for the whole area of the test facility; one monitored the melt flow inside the supply channel, and one registered the spreading process on the rectangular spreading surface. This camera was mounted above the surface at a vertical distance of 4 m. **Figure 3-2** shows the scaffold on which the different video systems were mounted.

Becker Technologies provided one black & white CMOS camera with arbitrary logarithmic characteristic of sensibility versus brightness. Because its low aperture angle, this camera recorded only part of the supply channel.

Infrared Camera

From Automation Technology GmbH an infrared (IR) video camera was positioned 4 m above the spreading surface to register the temperature at the melt surface. The camera was calibrated for a measuring range of 350-1800°C with an error < ±2 %. Because of the large 60° angle of the objective, the whole spreading area was monitored from the high mounting distance. The camera had a picture ratio of 4:3 with 320 x 240 pixels with a frame rate of 8.333 Hz.

Besides general information on the dynamics of spreading and crust formation, evaluation of the IR-records should allow an estimate of the characteristic temperatures of the melt during the spreading process, such as the liquidus/solidus range and the typical temperature, when the first crusts are formed.

3.2 Experimental Results

3.2.1 Test Procedure

The realized experimental process of the ECOKATS-1 experiment is provided in **Table 3-2**.

Before the beginning of the experiment the thermite powder was preheated in the thermite vessel to 100 °C for 18 hours to give a higher initial temperature of the melt. After completion of the test preparation the thermite powder was ignited 120 s before start of the melt pour.

Table 3-2: Realized process of the experiment ECOKATS-1

Real Time	Rel. Time [s]	Event
11:24:00	-180.0	Data acquisition started, measurement signals are available only after 80 s; consequently data recording starts at -100 s
11:25:00	-120.0	Ignition of thermite
11:26:54	-6.0	Thermite burn ends
11:27:00	0.0	Opening of the nozzle of the thermite vessel
11:27:02	2.5	Start of melt release to whirl basin, metal first
11:27:27	27.8	End of metal release, start of oxide melt release
11:27:31	31.8	Overflow of whirl basin: oxide enters supply channel, start of spreading
11:27:38	38.0	Melt at thermocouple WOPLC2 in the supply channel
11:27:44	44.2	Melt at the end of the supply channel
11:27:44	44.8	Melt reaches the edge of thermocouple module-1 at x = 14 cm , y = 0 on the centreline of the spreading area)[1]
11:27:45	45.2	Melt reaches the middle of thermocouple module-1 at x = 20 cm; the movement shortly stops at this position, but the melt flows around module-1.
11:27:47	47.2	Melt flow over thermocouple module-1 is set in motion.
11:27:48	48.2	Melt reaches the cross sign at x= 40 cm / y = 0.
11:27:49	49.1	Melt reaches the cross sign at x= 60 cm / y = 0.
11:27:50	50.2	Melt reaches the cross sign at x= 80 cm / y = 0.
11:27:51	51.5	Melt reaches the edge of thermocouple module-2 at x = 96 cm
11:27:52	52.0	First stop of the melt in longitudinal direction at x = 98 cm, shape of the spread melt nearly symmetrical
11:27:54	54.0	Melt front moves very slowly in longitudinal direction and finally stops at x =100 cm in the middle of thermocouple module-2. Lateral spreading is continuing nearly symmetrically.
11:28:03	63.0	Longitudinal front still stopped at x = 100 cm; lateral spreading symmetrically reaches y = ± 120 cm. From now, the melt flow is arbitrary and asymmetric with various irregular outflows of melt by overflow or melt-through of the front crust
11:28:56	116.7	End of melt release from thermite vessel
11:29:11	131.8	End of spreading, the final covered area is reached
11:43:12	972.0	On the left furthermost part of the solidified melt, an area of about 0,5 m^2 was abruptly disrupted from the concrete surface and moved 7 cm away in flow direction.

)[1] see definition of the coordinate system at the end of the supply channel in **Figure 3-6**

Figure 3-9 shows the weight of the thermite reaction crucible, with the reaction period of the thermite (from -100 to -6 s) and the melt release starting at time zero (definition of t = 0 s). In the last phase of the thermite reaction, an extraordinary oscillation occurred, probably caused by the intense chemical reaction of a residual mass of thermite powder in the lower crucible head. Thermite burn was completed at -6 s, 114 s after the ignition, indicated by the end of oscillations of the weighing system. In earlier tests with similar thermite mixtures, the strong thermite reaction occurred mostly at the initial phase of the thermite burn; therefore this effect was not expected at the end of the burning process. The short remaining time of 6 s until pour was just sufficient for the segregation of the metal and of the oxide phases.

The release of 786 kg melt (212 kg metal and 574 kg oxide), starting at time zero was completed after 116.7 s. The oxide melt entered the spreading channel with no horizontal momentum from the pouring process
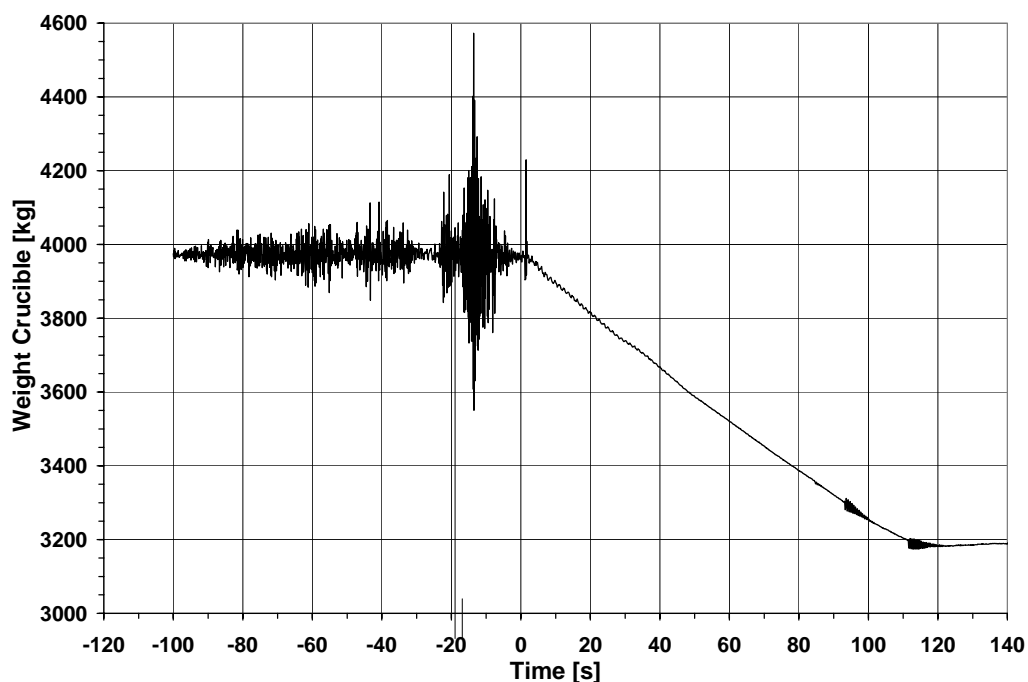
Figure 3-9: Weight of thermite vessel during thermite burn and melt release

Figure 3-10 gives a more detailed view of the weight of the thermite vessel during melt release. Two different slopes characterize the weight reduction: The steeper slope is related to the release of the heavier metal, and reduces to a more moderate slope at t=27.8 s, when the melt changes from metal to the lighter oxide. At the end of the curve two short vibrations at 93.3 s and 111.5 s have been recorded, caused by suddenly released thermal stresses in the crucible.

From this curve the equivalent mass flow (pouring rate) into the whirl basin was derived which characterizes the spreading period from 31.8 s (start of spreading, i.e. start of outflow to the supply channel) to 116.7 s.

Table 3-3 gives the time intervals, for which a stepwise constant mass flow rate was determined to be used for code calculations. In this table, the time zero is the start of spreading at 31.8 s.

Table 3-3: Stepwise constant mass flow of the melt in ECOKATS-1

Time [s]	Oxide Mass flow [kg/s]
[0.0, 16.1]	7.8351
(16.1, 70.0]	6.6614
(70.0, 79.6]	4.775
(79.6, 84.9]	3.083
t > 84.9	0.0
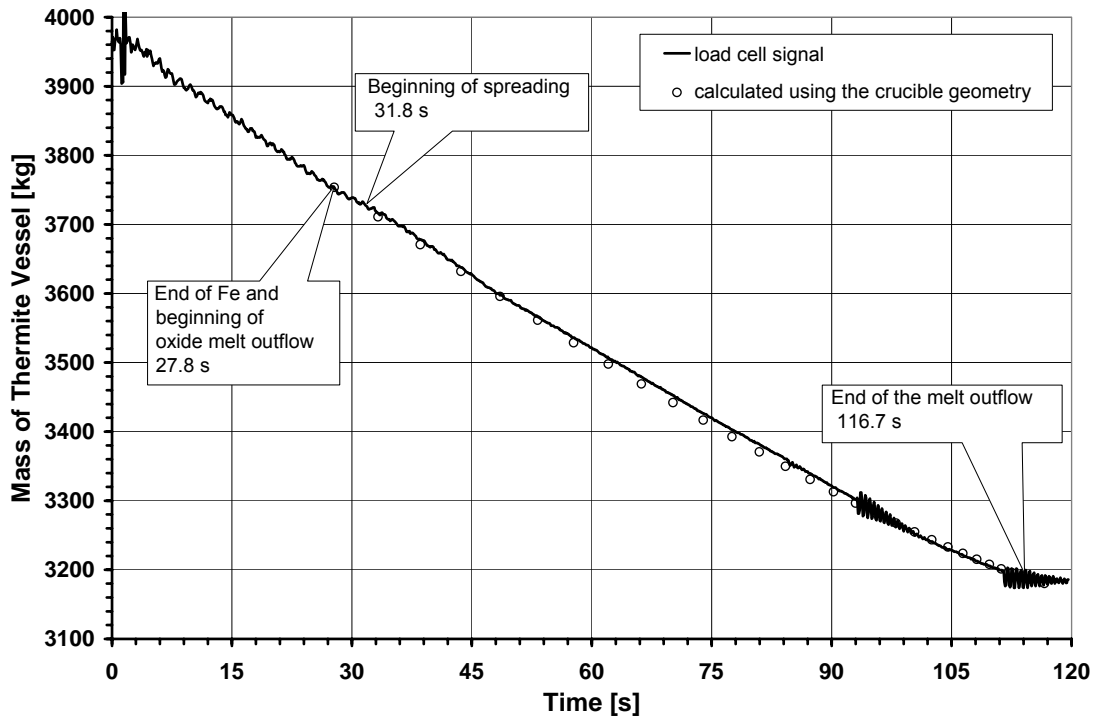
Figure 3-10: Mass of thermite vessel during outflow of the melt in ECOKATS-1

The mass of the melt which arrived at the spreading surface was investigated by weighing the whole spreading area including the attached whirl basin. **Figure 3-11** shows the history of the registered weight during the experiment with some unavoidable disturbances which are mainly due to the melt concrete interaction.

With both weight curves **Figure 3-10** and **Figure 3-11**, the mass balance of the spread melt could be analyzed. The metal fraction which remained in the whirl basin was determined after the experiment by weighing this part separately. Inevitable losses between inserted mass and spread melt mass come from a thin melt layer remaining in the crucible, from melt splashing outside of the spreading area, and from evaporation of water from the concrete. The resulting masses for the experiment ECOKATS-1 are given in
Table 3-4 and **Table 3-5**. In these tables also the characteristics of the melt and the conditions during spreading are given.

It is recognized that the experimental data are very close to the planning so that the experiment fulfils the requirements.
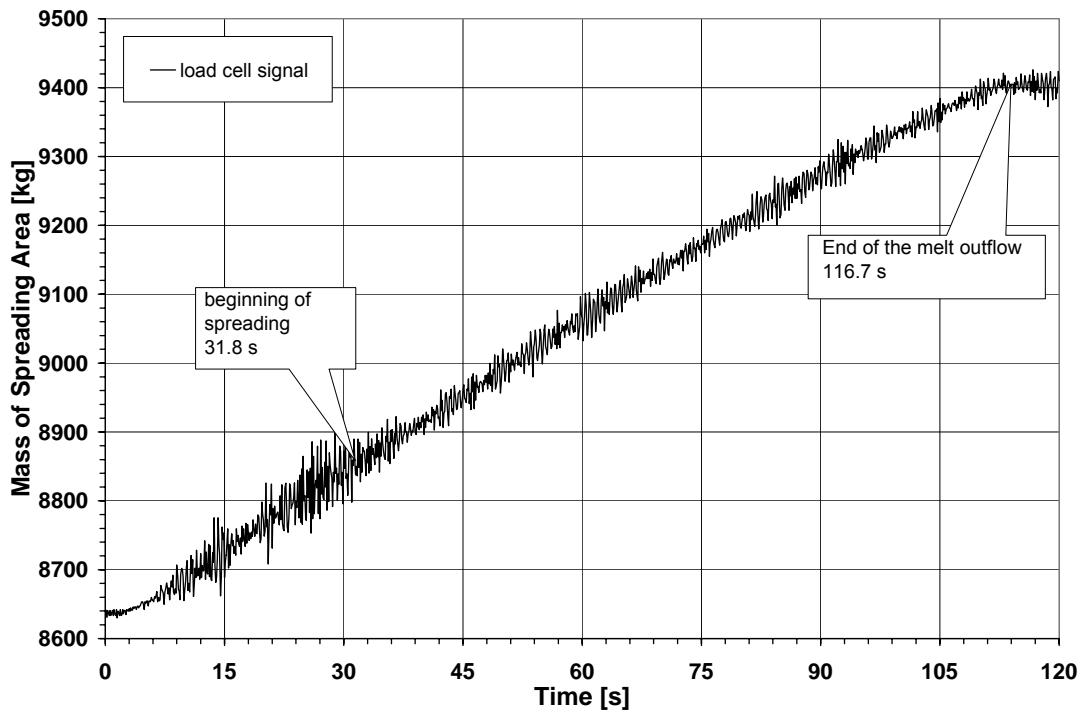
Figure 3-11: Mass of spreading device during outflow of the melt in ECOKATS-1

Table 3-4: Characteristics of the melt in ECOKATS-1

Parameter	planned	realized	outflow from crucible	received at basin & spreading area
total mass of mixed thermite	816.24 kg	816 kg	786 kg [1]	771 [2]
preheating of thermite mixture	100°C	100°C		
metal fraction	216 kg	217 kg	212 kg	205 [3]
oxide fraction	600 kg	599 kg	574 kg	566 [4]
initial temperature of melt	1590°C	1600°C [5]	1600°C [5]	1600°C [5]
initial rate of oxide outflow	2 liter/s		2.4 liter/s	2.4 liter/s
duration of oxide melt release	110 s [6]		89 s	89 s

[1] the missing 30 kg formed a film on the inner wall of the thermite crucible
[2] the missing 15 kg resulted from the splashed melt and from the evaporated water
[3] solid metal regulus, measured in the whirl basin
[4] 547 kg were released to the spreading channel
[5] TC measurement in the whirl basin
[6] calculated by using the too low oxide density of $\rho \sim 2700$ kg/m^3

Table 3-5: Conditions during spreading of the melt in ECOKATS–1

Parameter	ECOKATS-1
Initial temperature of the melt	1600°C/1873 K
Initial flow rate of the melt	2.4 litres/s
Duration of melt pour to surface	85 s
Spread melt mass	547 kg

Spreading surface
    B x L
    Melting temperature
	Siliceous concrete
	3.0 m x 4.0 m
	~ 1573 K

3.2.2 Spreading of the Melt

Table 3-2 gives the most interesting observations during spreading from 31.8 to 131.8 s. **Figure 3-12** shows successively the spreading of the melt with pictures from the infrared camera. On the right side of each picture the end of the supply channel is shown from which the melt entered the spreading area. In the first 3 pictures, the right sidewall of the spreading area is marked with a line. The crosses in the pictures indicate the positions of the thermocouple modules M01-M03. The lower edge of each picture is identical with the lateral wall of the spreading area. The section of the spreading surface in the picture corresponds to 3 m x 2.4 m. Each picture of the series is labelled with the associated relative time (according to **Table 3-2**) and in brackets with the time referred to the start of spreading in the supply channel at t=31.8 s. On the right side, the temperature colours from 300-1500 °C are given, assuming the emissivity of the melt as 0.92. One has to keep in mind that the infrared technique provides only the temperature of the surface of the melt.

The front advanced by deforming the crust, pushing it away and building outbreaks. Until 63 s, the contour of the melt was nearly symmetrical. Later on, an irregular shape of the moving front developed (see **Figure 3-12** and **Figure 3-13**).

46.7 s [14.9 s]

48.2 s [16.4 s]

49.1 s [17.3 s]

50.2 s [18.4 s]
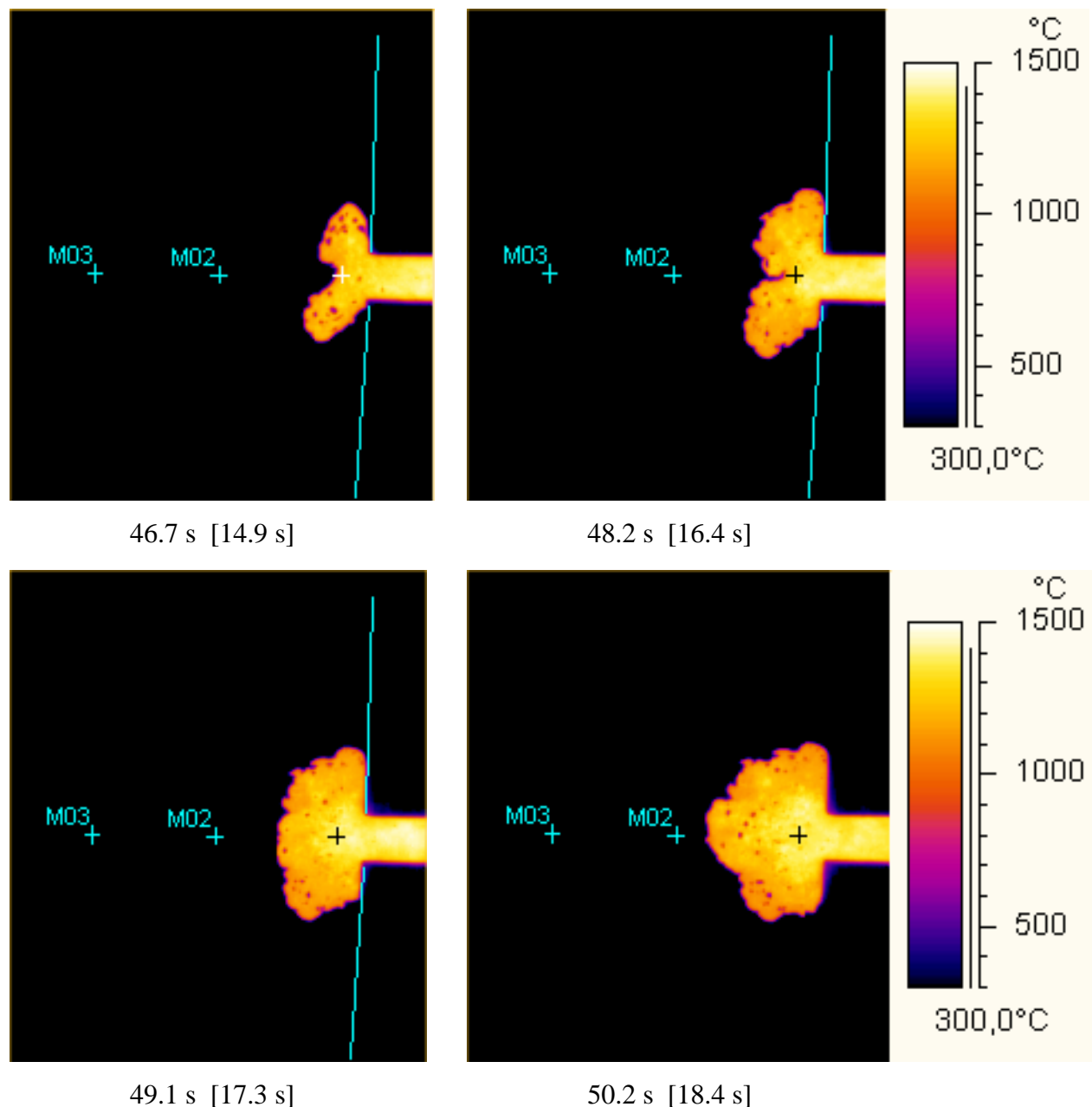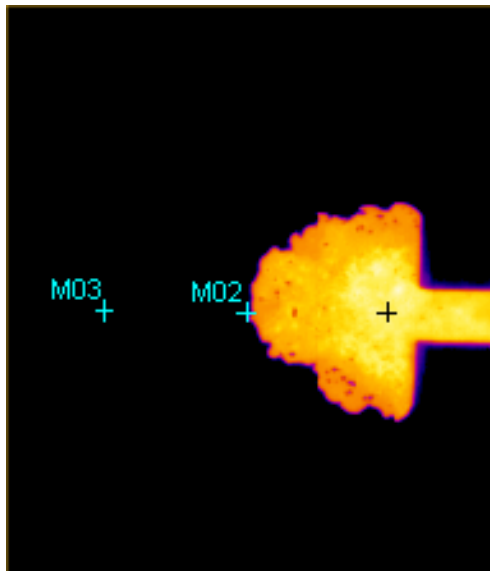
51.8 s [20.0 s]
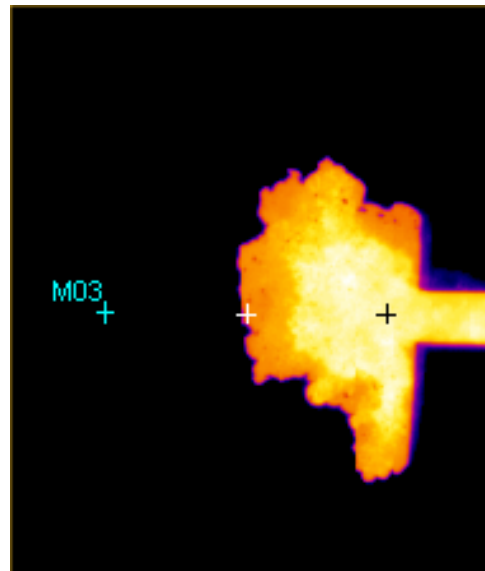
57.0 s [25.2 s]
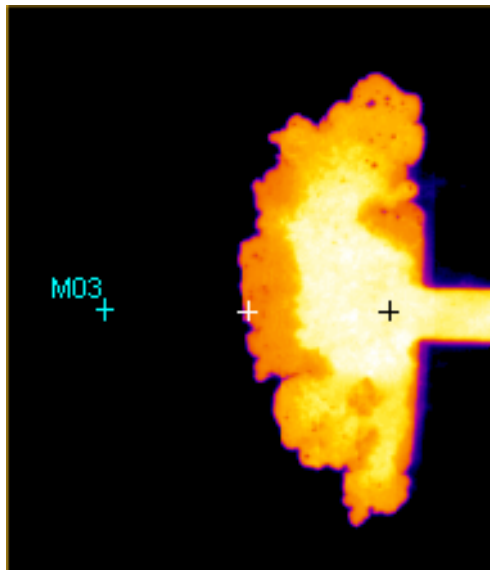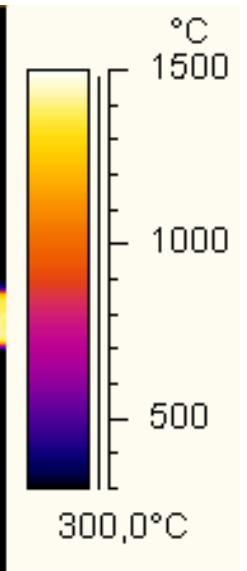
61.8 s [30.0 s]
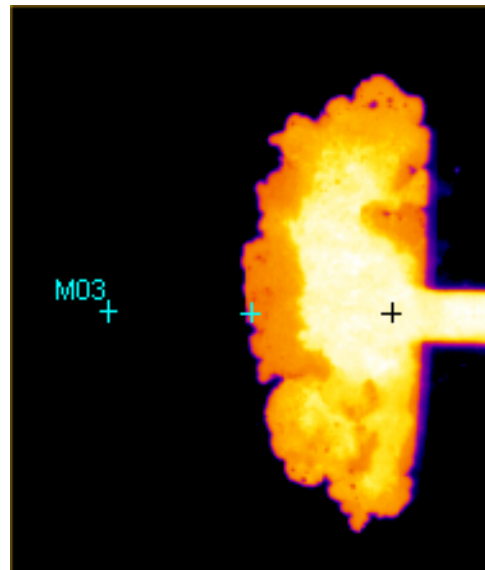
63.0 s [31.2 s]
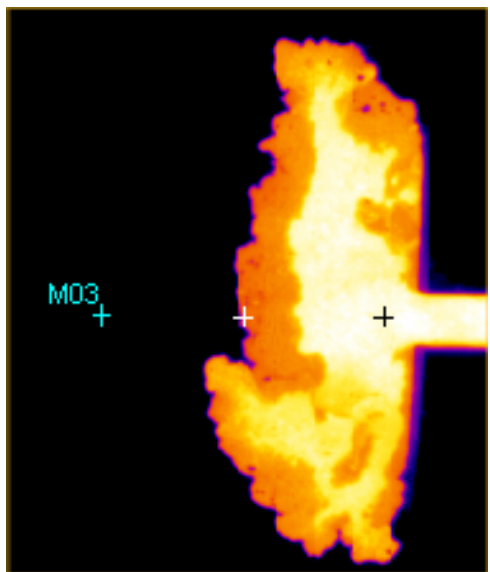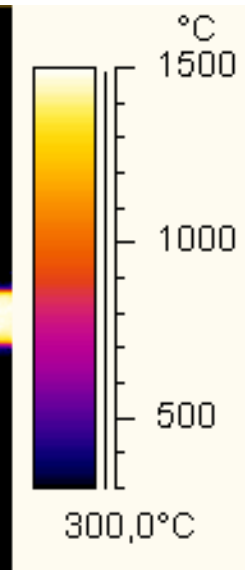
71.8 s [40.0 s]
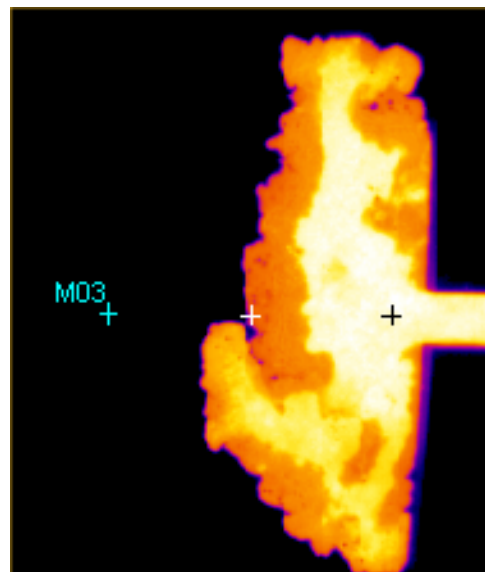
75.0 s [43.2 s]
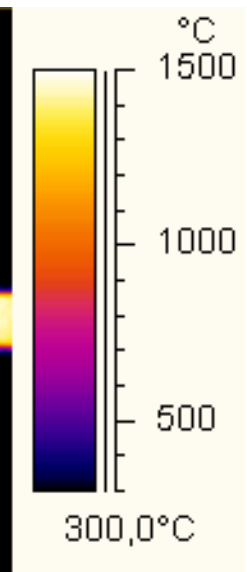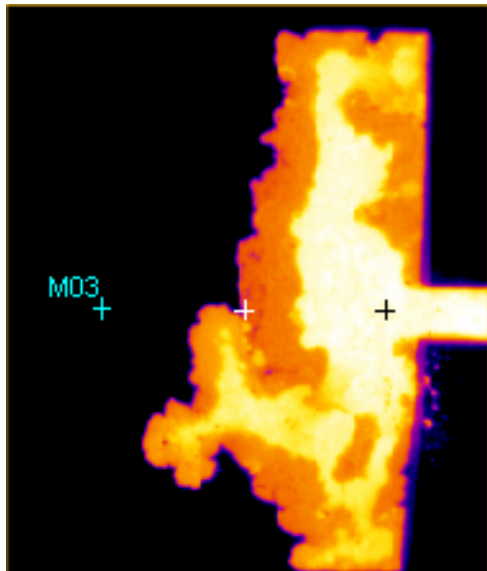
81.9 s [50.1 s]
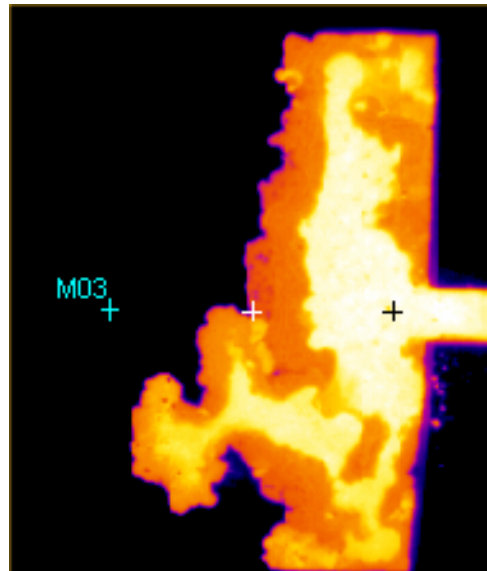
87.0 s [55.2 s]
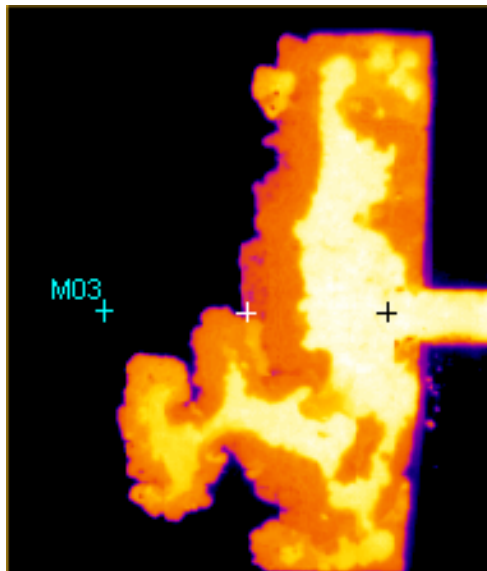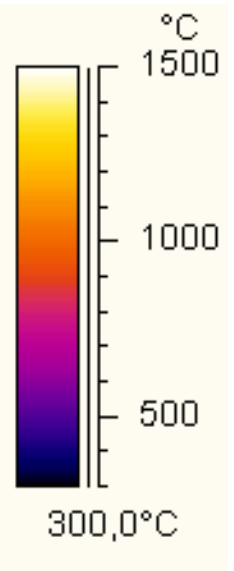
91.8 s [60.0 s]
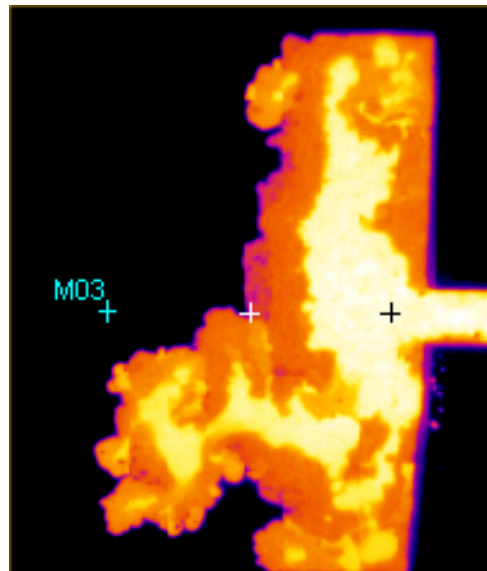
101.8 s [70.0 s]
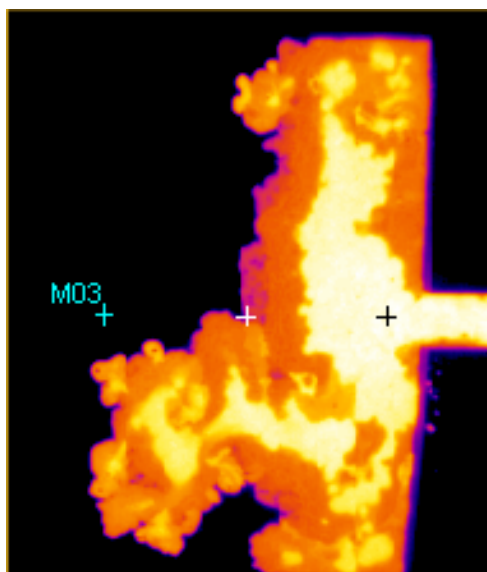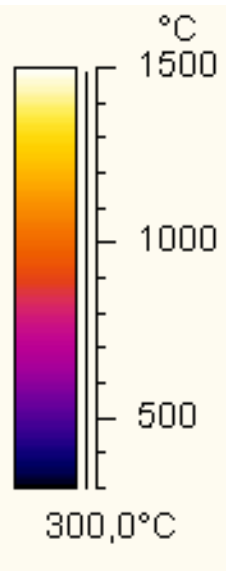
105.1 s [73.3 s]

111.8 s [80.0 s]
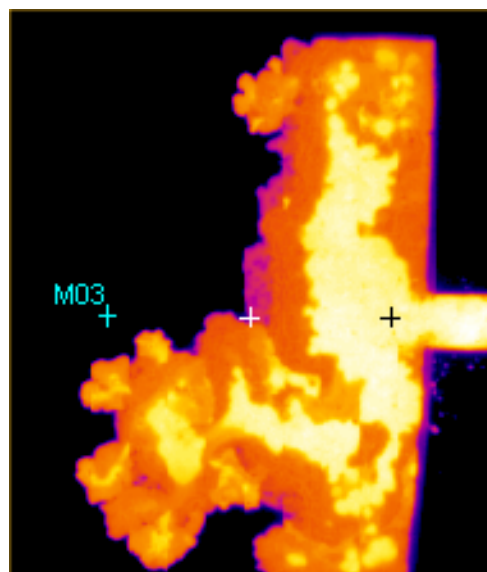
117.1 s [85.3 s]   131.8 s [100.0 s]
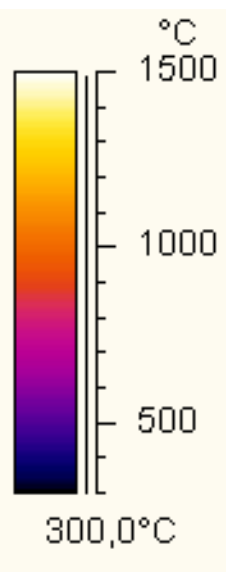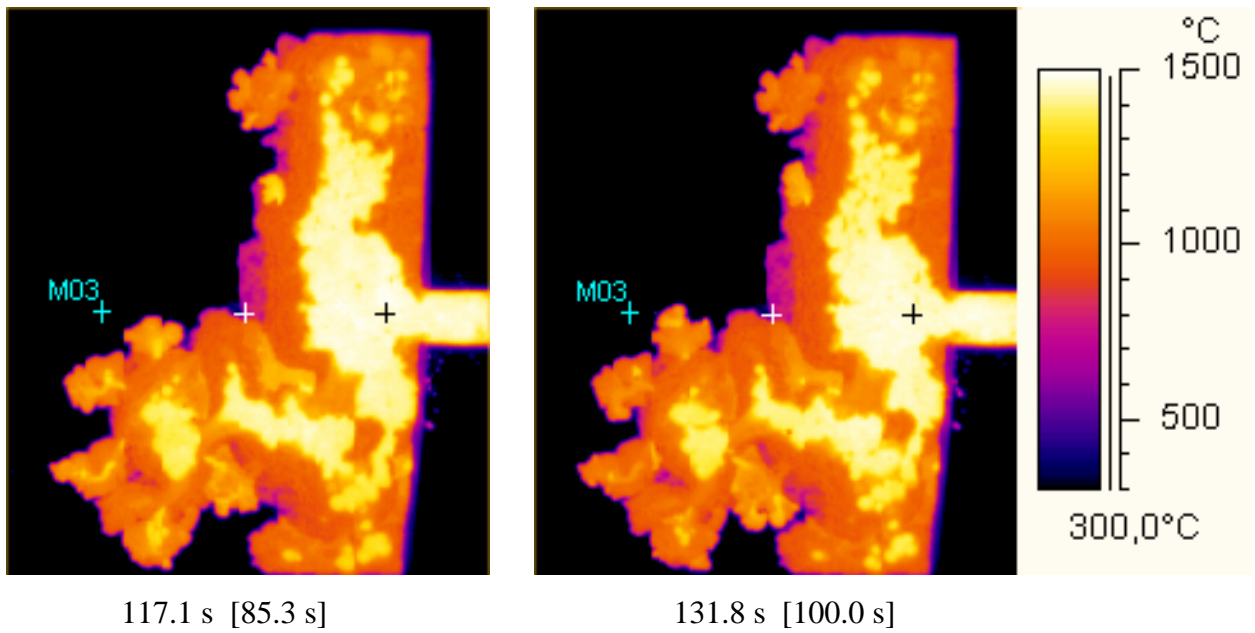
(Time in s: after start of melt pour / [after entering the flow channel])

Figure 3-12: Spreading of the melt from infrared camera in ECOKATS-1

The first picture in **Figure 3-12** at 46.7 s shows how the melt was flowing around the protruding thermocouple of module 1, whereas the middle of the melt stopped shortly at this position. Further at 52 s the melt front stopped at x =100 cm, i. e. at the centre of the thermocouple module 2. Thermocouple module 2 was indeed not covered during the whole period of spreading. From 52 s to 70 s, the melt propagated mainly towards the lateral walls. The melt front ceased to move at 131.8 s, [100 s after start of spreading], i. e. 15 s after the end of the melt release (**Figure 3-13**).
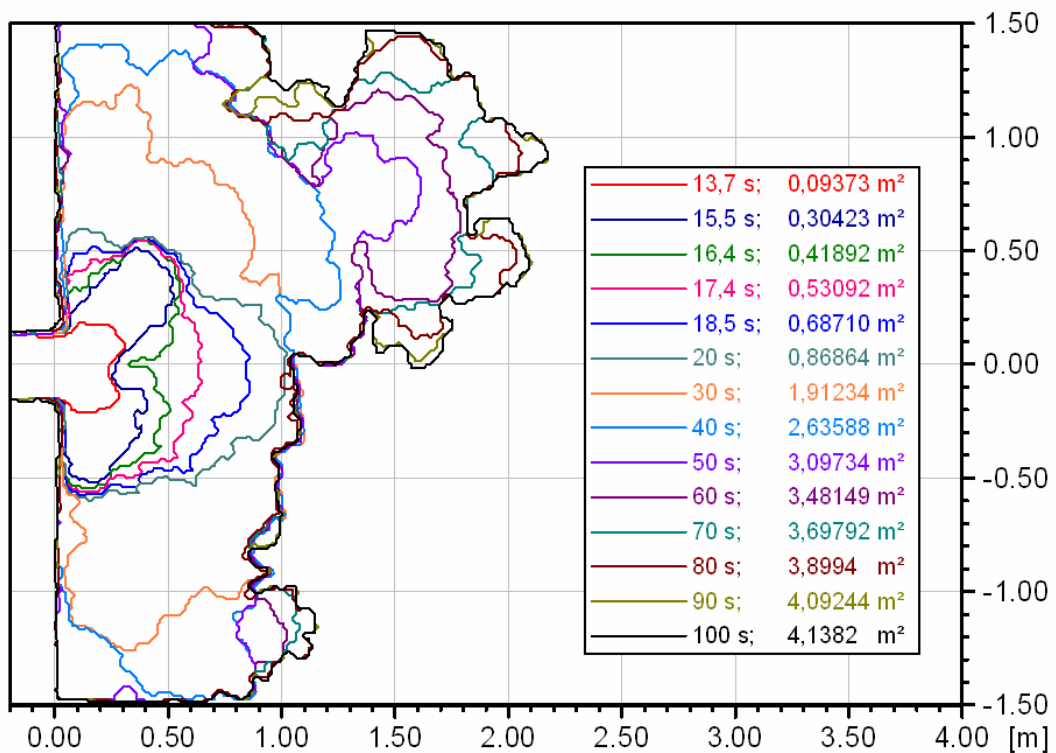
Figure 3-13: Contours of the melt front as a function of time

From the infrared measurements the covered area of the spread melt could be determined by numerical integration for different times of the spreading process. To analyse the highly irregular melt contour, as shown in **Figure 3-13,** a boundary temperature of about 700 °C was set as limiting value. **Figure 3-14** shows the estimated area of the large concrete surface versus time that was covered by the melt. Note, that in this diagram time zero is set to the first entrance of the melt into the supply channel at 31.8 s. The covered area after completion of the spreading process is 4.89 m² (incl. the channel area).
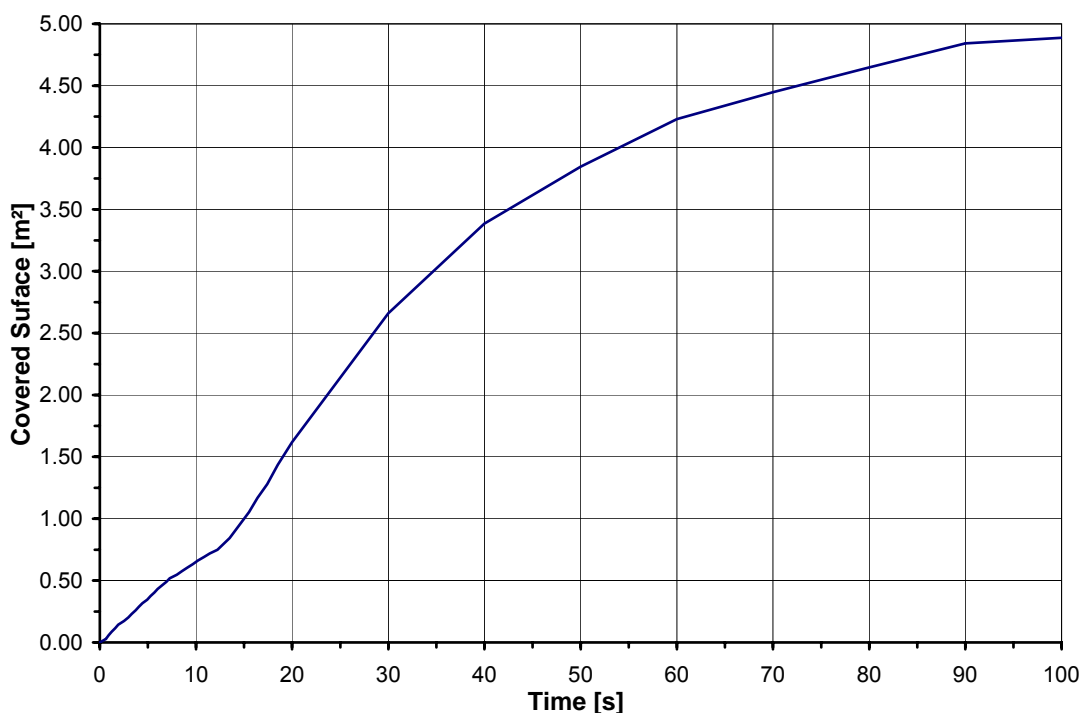
Figure 3-14: Area of the spreading surface covered by the melt versus time

Similar to the test ECOKATS-V1, the movement of the melt front into the x direction versus time was analysed. **Figure 3-15** gives the melt front positions in the supply channel evaluated from the video records, and is the basis for the calculation of the front velocity in **Figure 3-16**. Time zero is set to the first entrance of the melt into the supply channel at 31.8 s after start of melt release. The melt flow starts at the beginning of the channel with an average velocity of 0.27 m/s, and slows down to 0.13 m/s after 2.6 m at the end of the channel.

Based on the gravity-viscous solution for melt spreading [6] mentioned in chapter 2.2.3, the front motion was calculated along the supply channel. **Figure 3-15** and **Figure 3-16** show that with the estimated initial melt viscosity of 0.72 Pa·s the melt front motion in the channel during the time period of 12 s, is in good agreement with the experiment. From this comparison it is obvious that due to the influence of gas production from the decomposing concrete the initial "effective" viscosity of the melt in ECOKATS-1 is a factor 3.6 higher than in ECOKATS-V1 where the melt spread on inert ceramic. This increase is due to the presence of gas bubbles in the melt.

The motion of the melt front on the 2-d spreading surface into the x direction was evaluated along the centreline of the surface (**Figure 3-17**). The relatively long melt stop of about 2 s at 0.2 m is illustrated by the first picture of **Figure 3-12**, where the melt flows around the protruding thermocouple in module 1. Thereafter, melt flow continued without interruption until the final stop at 1 m. In **Figure 3-18** the velocity of the melt front, calculated from **Figure 3-17** is shown. The starting point in this figure is equivalent to

the last point at the end of the supply channel (**Figure 3-16**). At the entrance to the 2-d surface first the velocity of the melt slightly increased to 0.22 m/s and then stopped at module 1. Afterwards, the motion of the melt increased again to 0.21 m/s over a time period of 2 s to slow down continuously to the final stop of the melt at 20.2 s. The duration of melt spreading on the centreline of the 2-d surface was 7.8 s until the final stop. Further spreading occurred beyond the centreline, mainly in perpendicular direction and on the left side of the surface, as described above.
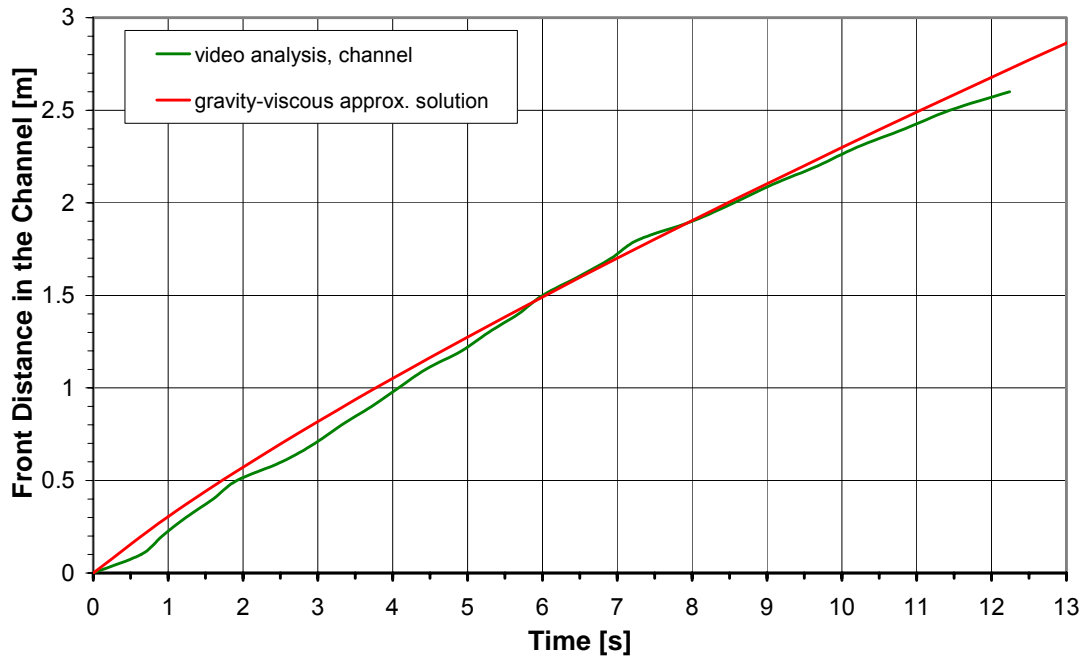
Figure 3-15: Melt front position in the supply channel of ECOKATS-1
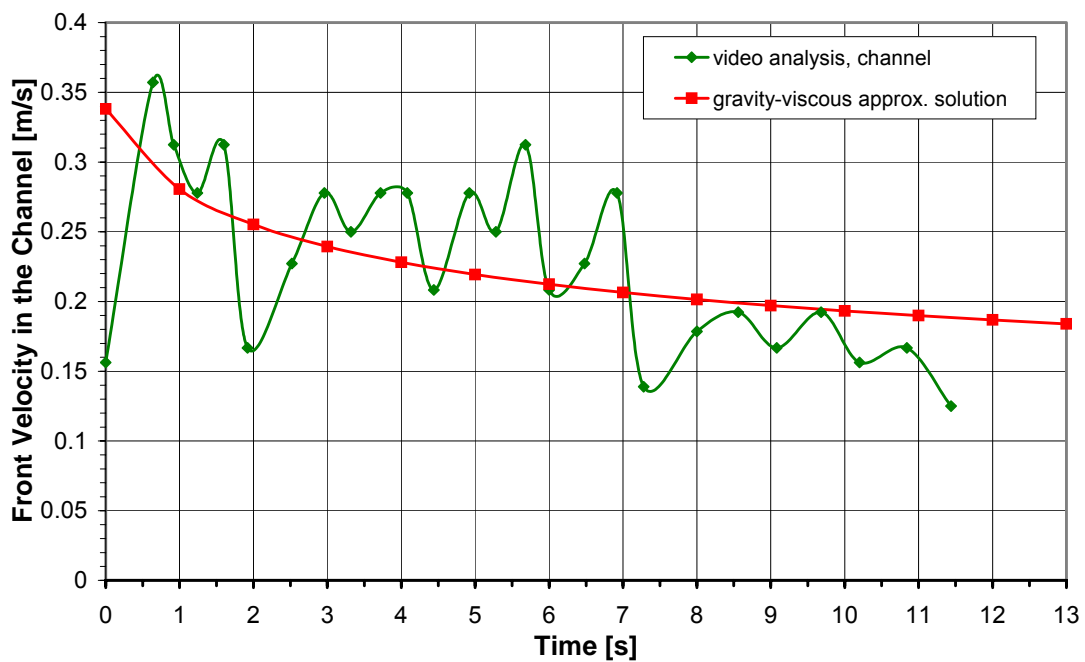
Figure 3-16: Melt front velocity in the supply channel of ECOKATS-1
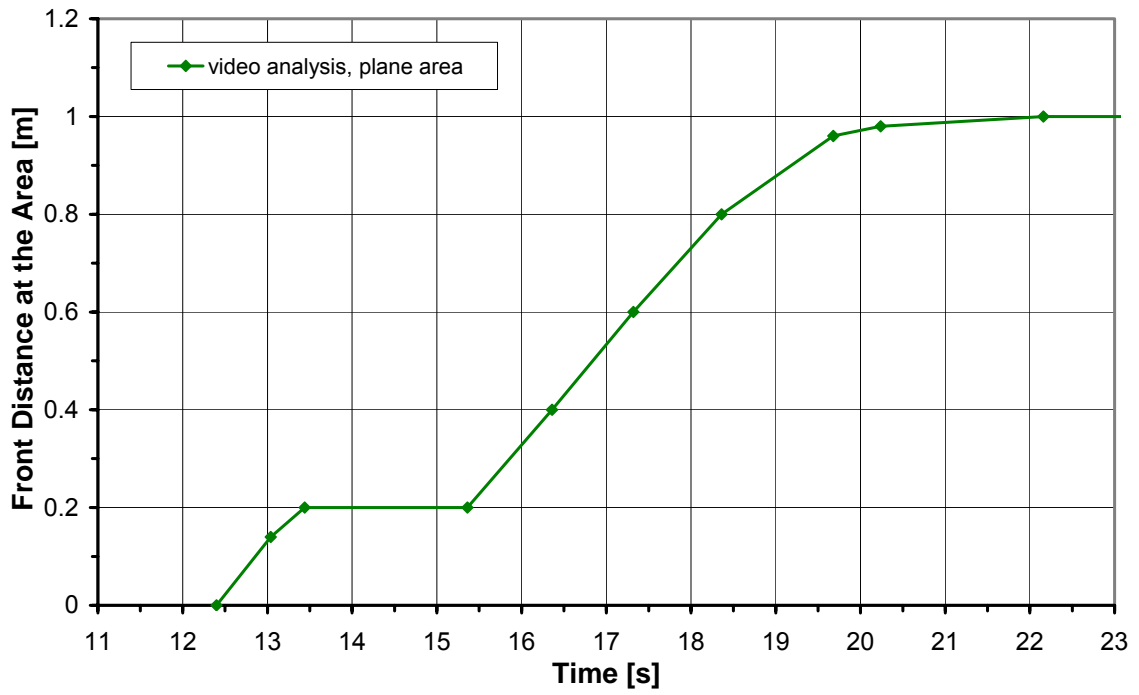
Figure 3-17: Melt front position along the centreline of the spreading surface in ECOKATS-1
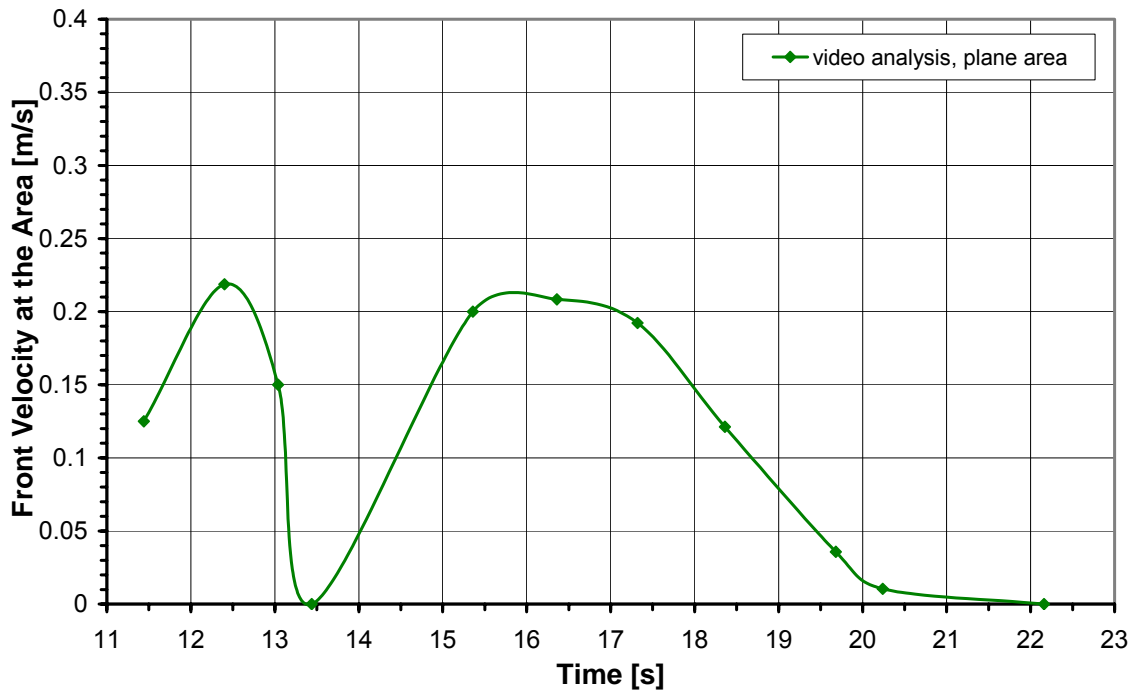
Figure 3-18: Melt front velocity along the centreline of the spreading surface in ECOKATS-1

Figure 3-19 shows the melt during the cool-down, 63 s after the end of spreading. In the photograph the formation of the surface structure is illustrated. The bright spots indicate small volcanoes or bubbles that were generated by gas release from the concrete. This process formed an uneven crust surface shown in **Figure 3-20**.
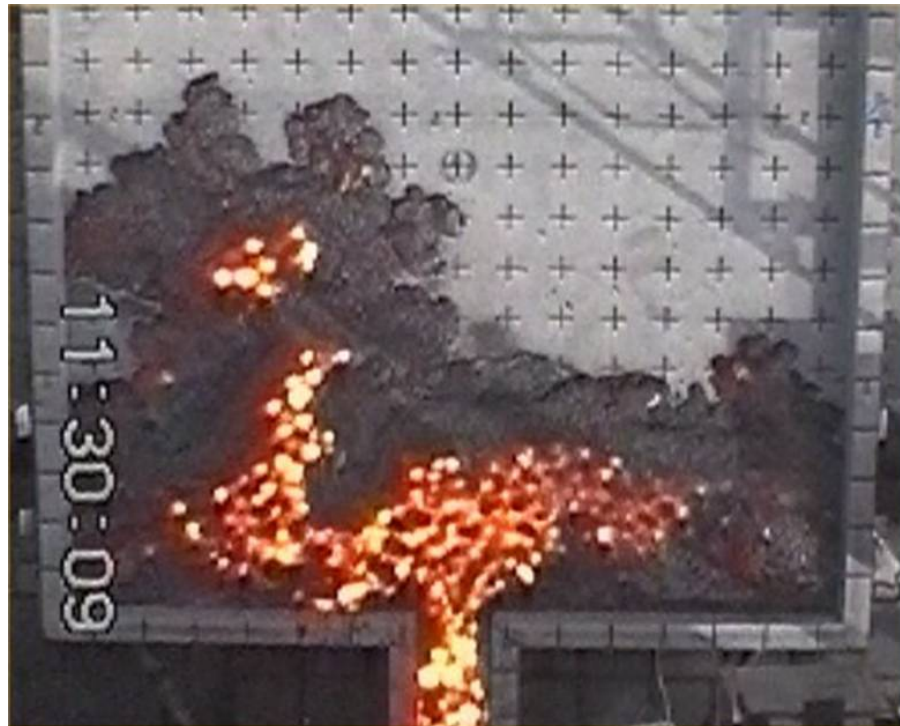
Figure 3-19: Cool-down of the melt 63 s after the end of spreading in ECOKATS-1
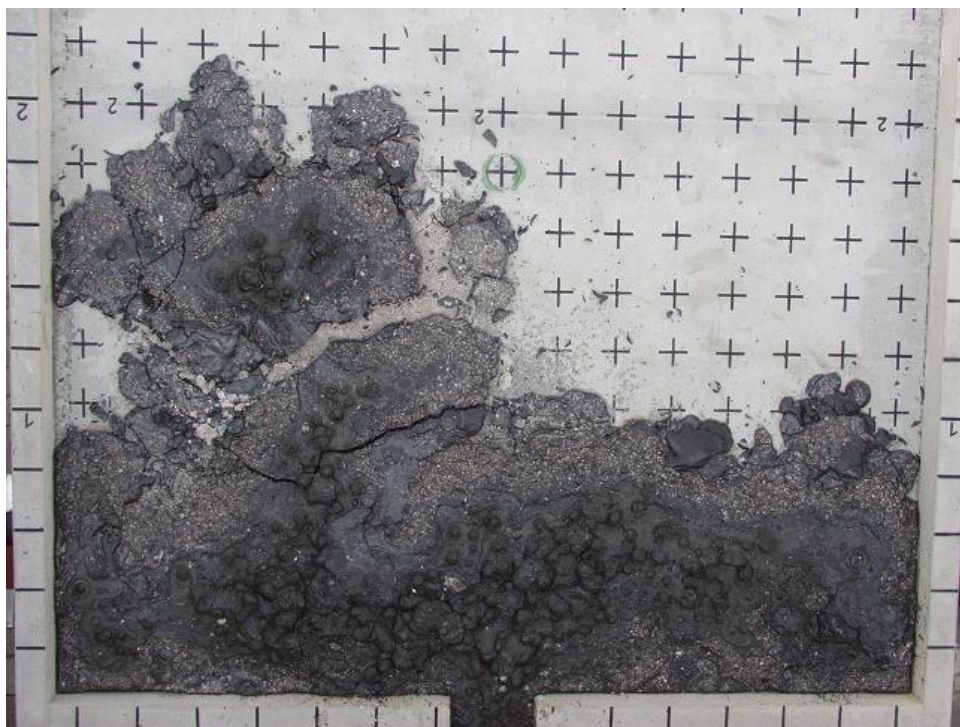
Figure 3-20: Contour of the spread melt after cool down

At 972 s (~16 min) during the cool-down of the solidified melt, a loud bang occurred. Under the left furthermost part of the solidified melt a continuous thin layer of concrete of about 1 m^2 was suddenly disrupted from the substrate and moved a part of the solidified melt about 7 cm into the flow direction. The left photo of **Figure 3-21** shows the region of the separated concrete layer marked by the hatched area. In the right picture a local edge of the broken substrate (at x=100 cm / y=100 cm) with a delamination depth of 28 mm is given.

This process of spallation of the concrete surface is attributed to thermal stresses in the uppermost layer and to gas release from the concrete with possible pressure build-up.

Figure 3-21: Area of spalled concrete under the solid melt and detail of the fracture edge

3.2.3 Measured Temperatures

3.2.3.1 Temperature of the Melt in the Whirl Basin

To measure the temperature of the melt at start of spreading, three W-Re thermocouples WOPLW1, WOPLW2 and WOPLW3 were installed in the whirl basin at elevations of 70, 195 and 220 mm above the bottom (**Figure 3-4**). The measured temperatures are shown in **Figure 3-22** together with the records of the W-Re element WOPLC1 at start of the supply channel. As in ECOKATS-V1, the first increase of the measured temperature is due to radiation and possibly to some splashed melt, followed by a fast temperature rise at direct contact of the sensor with the melt at 11, 22, and 24 s, respectively. The comparison verifies that the three measurements in the basin are reliable and give the initial temperature of the spreading melt as 1600°C ± 10°C. The slightly lower temperature measured by WOPLC1 which is positioned near the entrance of the channel, may be due to the thermal boundary layer that is formed close to the concrete bottom (see section 3.2.3.2).
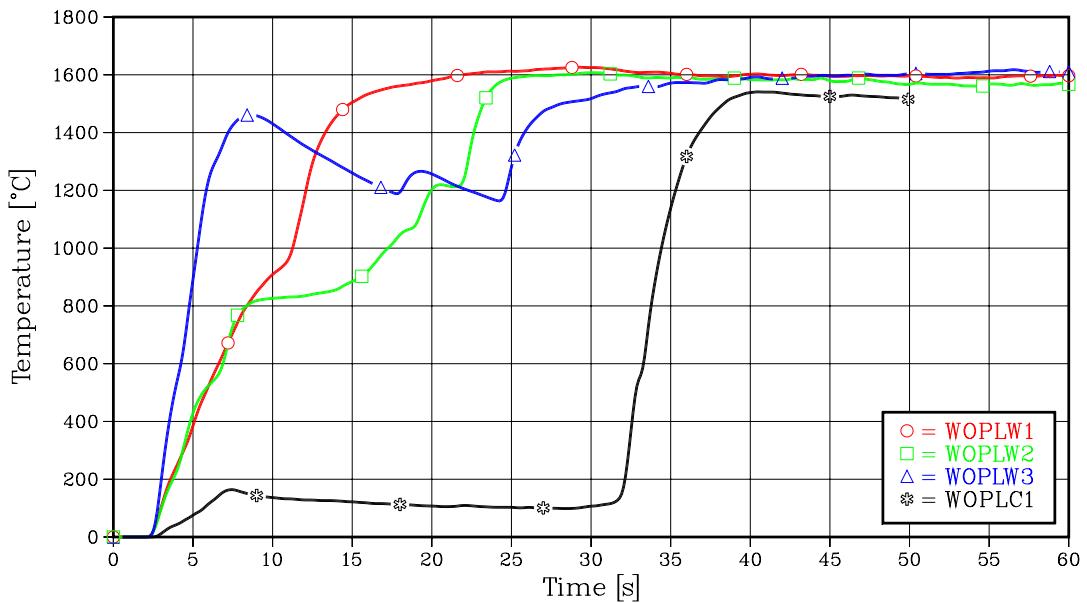
Figure 3-22: Temperature of the melt in the whirl basin and nearby

3.2.3.2 Temperature of the Melt in the Supply Channel

The temperature of the melt at the entrance of the supply channel and 1.5 m from the entrance were measured with the thermocouples WOPLC1, NIMAC1, and WOPLC2 as illustrated in **Figure 3-6**. The corresponding measurement signals with the associated arrival time of the melt are shown in **Figure 3-23**. The measurements show a reduction of the temperatures from 1540 °C to 1426 °C along the way of 1.5 m in the channel. However, one has to consider that these thermocouples are located 10 mm above the concrete surface so that the heat transfer to the concrete and the formation of a thermal boundary layer or a growing melt crust may influence the measured temperature, so that they may not represent the bulk temperature of the melt.

The thermocouple NIMAC1 failed at a temperature of 1350 °C as was expected. It was primarily implemented to identify the arrival time of the melt at the entrance of the supply channel, which is 31.8 s as listed in **Table 3-2**.
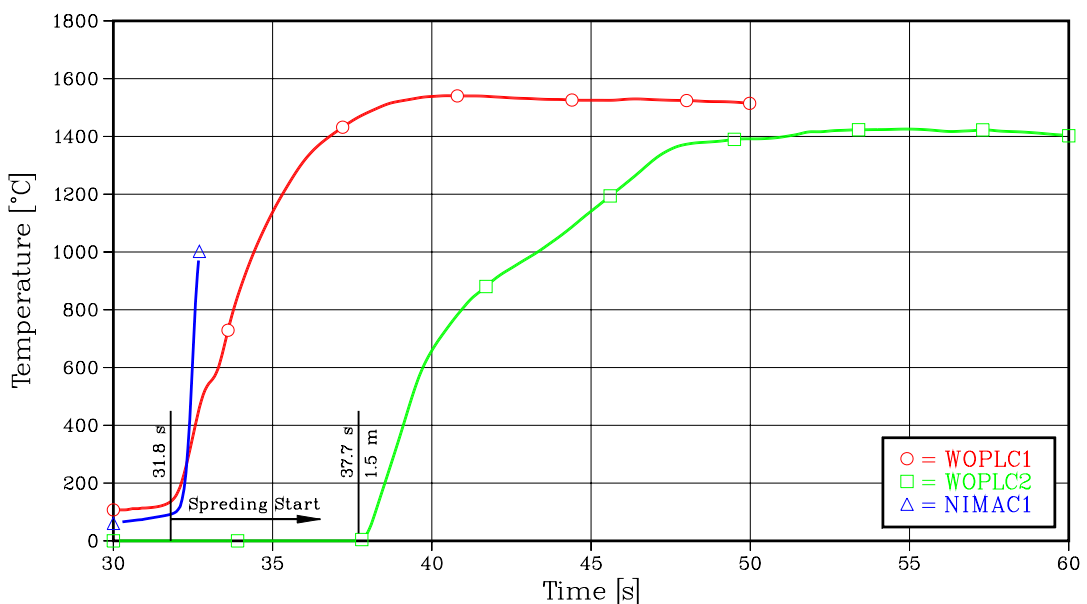
Figure 3-23: Temperature of the melt measured in the supply channel

The temperatures measured by thermocouples can be compared with the measurements of the infrared camera. From the IR video records, the maximum temperature values at the end of the supply channel were taken over a time period of about 100 s. **Figure 3-24** presents the results of this evaluation together with the thermocouple measurements in the whirl basin. The comparison shows consistent results of both measurement systems. Due to the cooler front part of the spreading melt, a short start up phase was necessary until the infrared camera recorded the same temperature level of about 1500 °C as the thermocouples in the whirl basin.
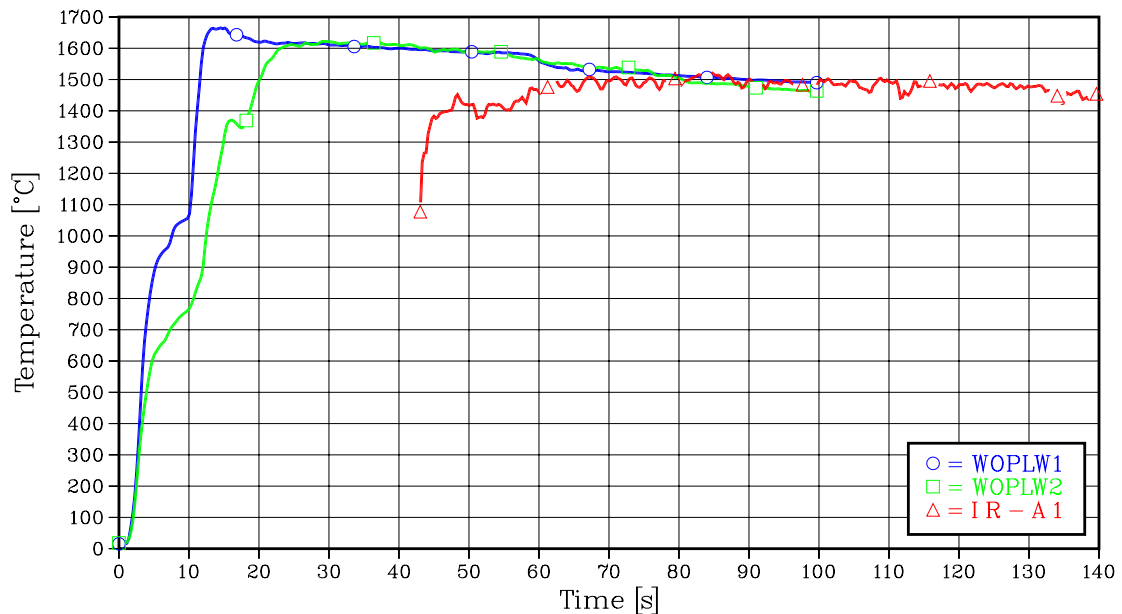
Figure 3-24: Temperatures in the whirl basin and IR measurements at the end of the channel

3.2.3.3 Temperatures on the Spreading Surface

To measure the temperature of the melt on the large concrete surface and the temperature distribution in the concrete surface, four instrumentation modules with several thermocouples were implemented in the concrete (**Figure 3-6** and **Figure 3-7**). As mentioned above, the melt only reached the module 1 with a brief stop of spreading, and partly module 2 which was only slightly covered with relatively cold melt.

Those thermocouples that are flush with the concrete surface (0 mm) measure under ideal conditions the contact temperature of melt and concrete. These thermocouples of the Ni-CrNi-type are NIWI11 and NIWI21 of module 1 and 2, respectively. The W-Re-thermocouples protruding 5 and 6 mm into the melt, are WOPL11 and WOMA11 of module 1 and WOPL21 of module 2. These sensors are located about 55 mm downstream of the Ni-CrNi thermocouples. Under ideal conditions, they would register the temperature in the bottom boundary layer of the spreading melt which is lower than the bulk temperature.

The measured temperatures over time are shown for the instrumentation module 1 in **Figure 3-25** and for the instrumentation module 2 in **Figure 3-26**. Some of the measured temperatures, however, are unphysical as the measured temperature in the melt is lower than at the concrete surface.
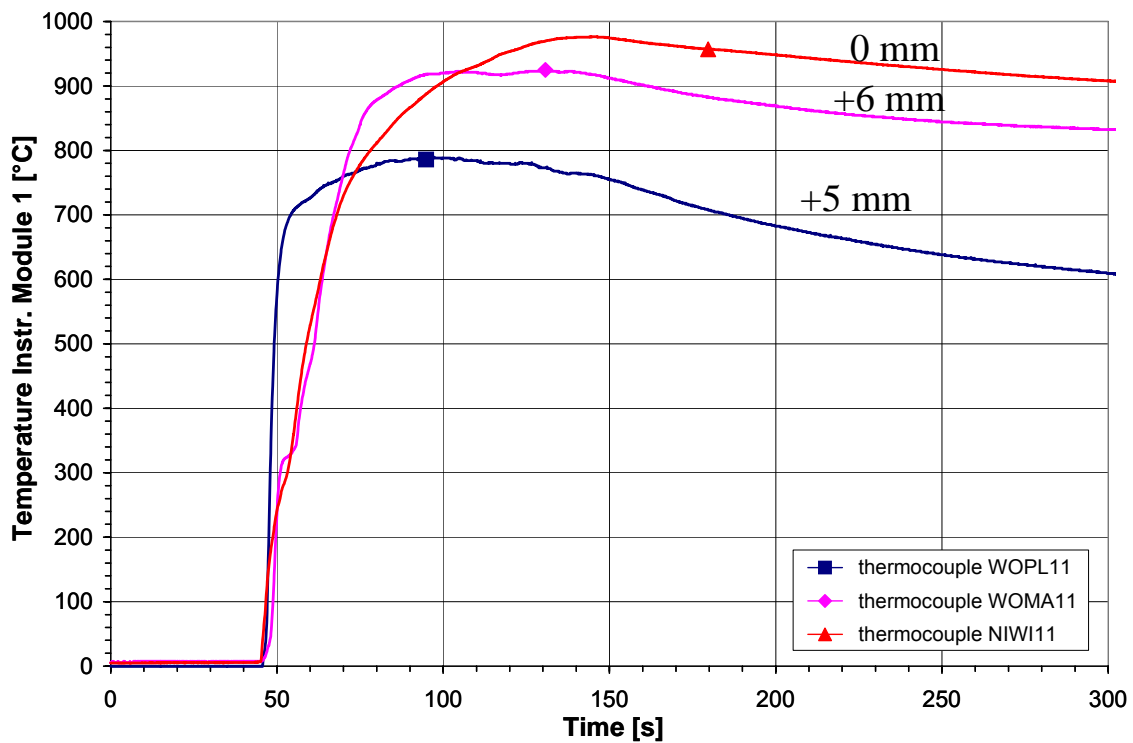
Figure 3-25: Temperatures measured by instrumentation module 1

The W-Re-thermocouple WOMA11of module 1 measured a temperature between 923 and 976°C at the + 6 mm position. This temperature is below the solidus temperature of the melt, indicating, that the melt has formed a crust over the tip of the sensor and the measured temperature is reduced by downward heat conduction through the metal sheath of the sensor. The actual temperature in the + 6 mm position in the boundary layer is certainly higher than registered. The same is true for the W-Re-thermocouple WOPL11, that measures even lower temperature. In addition, the short stop of the melt front near these sensors has reduced the temperatures of the melt front.

Similarly, the measurements of module 2 give no reliable information about the actual temperature of the melt, as the measured temperature was about 300°C only. Inspection of the thermocouple WOPL21 after the test showed that because of the low temperature of the melt the glass protection tube around the sensor was not melted.

The measured temperature at the concrete surface (980 °C at 0 mm) of module 1 seems reasonable and could be interpreted as the contact temperature of the hot melt and the cold concrete surface. A theoretical estimate of the contact temperature is 1070 °C, assuming 1-d transient heat conduction from the hot melt to the cold concrete. For this calculation, the initial temperature of the melt was assumed to be 1540 °C, allowing for some temperature reduction from the whirl basin to the position of module 1, and assuming constant physical properties of melt and concrete. This low temperature explains that no major erosion of the concrete substrate occurred.
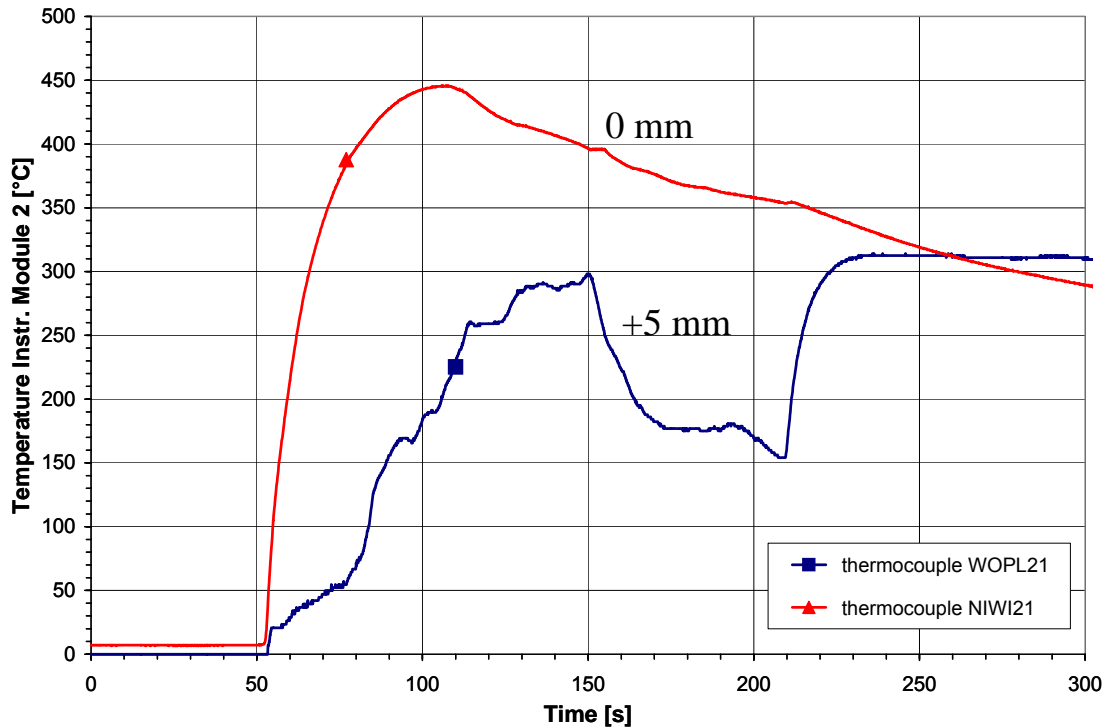
Figure 3-26: Temperatures measured at instrumentation module 2

To estimate the temperatures of the melt surface during spreading, the infrared measurements of the IR camera are evaluated at defined locations of the melt area. For the most important situations of the spreading process, the surface temperature is displayed in **Figure 3-27** to **Figure 3-30**. In each figure, the left picture shows the spreading situation at a given time with two defined lines of temperature measurement, namely a red line L1 along the flow direction in the middle of the surface and a green line L2 perpendicular to the flow. The temperatures along these two lines are given in the right diagram in each figure with the associated colours of the lines. The red temperature plot goes from left to right, whereas the green plot goes vertically from up to down. It is important to keep in mind that the evaluated surface temperature is, however, lower than the bulk temperature of the melt.

Figure 3-27 shows the situation when the melt flow interrupted at module 1, 46.7 s after the start of the melt pour, (see corresponding picture in **Figure 3-12**). **Figure 3-28** gives the situation when the melt stops at module 2 at 51.8 s and **Figure 3-29** shows the end of symmetric spreading at 61.8 s. Finally **Figure 3-30** shows the end of spreading at 126 s.

In the first 2 diagrams, the analysed centre of the melt surface has a maximum temperature of 1300 to 1400 °C. In contrast, the two last diagrams show a higher maximum central temperature of 1450 to 1480 °C, as the ongoing melt inflow continuously brings fresh melt to the central surface. The surface temperature of the incoming melt in the supply channel is 1460 to 1480 °C, compared to the 1600 °C bulk temperature of the melt released into the whirl basin. Looking at the dynamics of the spreading process in the video registrations, it is evident that for the temperature near 1450 °C and above no surface crust exists. This is in agreement with the calculated liquidus/solidus temperature of the melt as for such a temperature the solid fraction would be too small to form a surface crust.

41
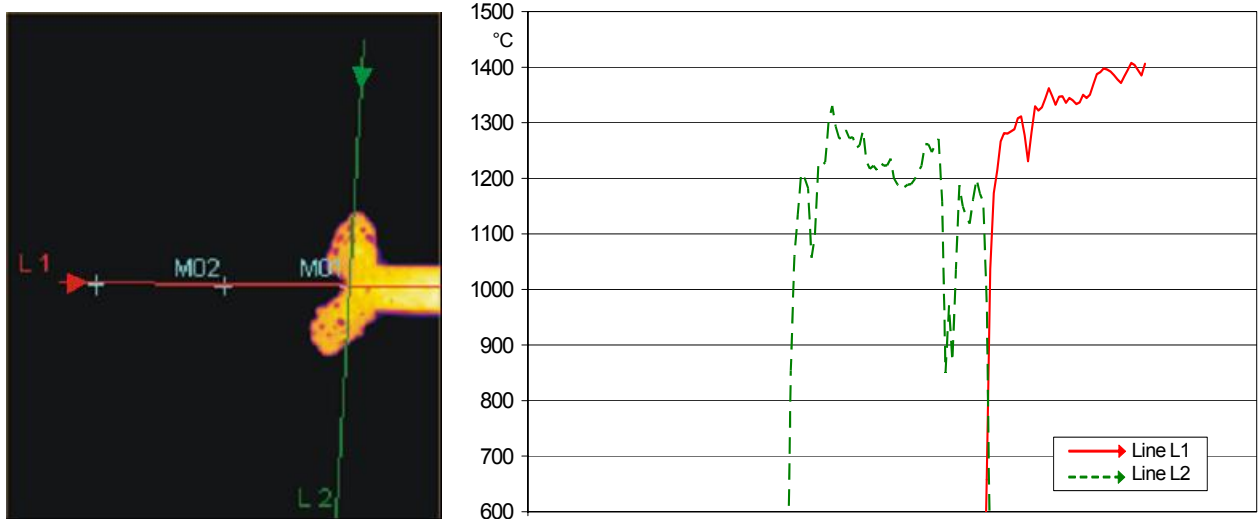
Figure 3-27: Surface temperature of the melt at 46,7 s [14.9 s] from infrared measurements
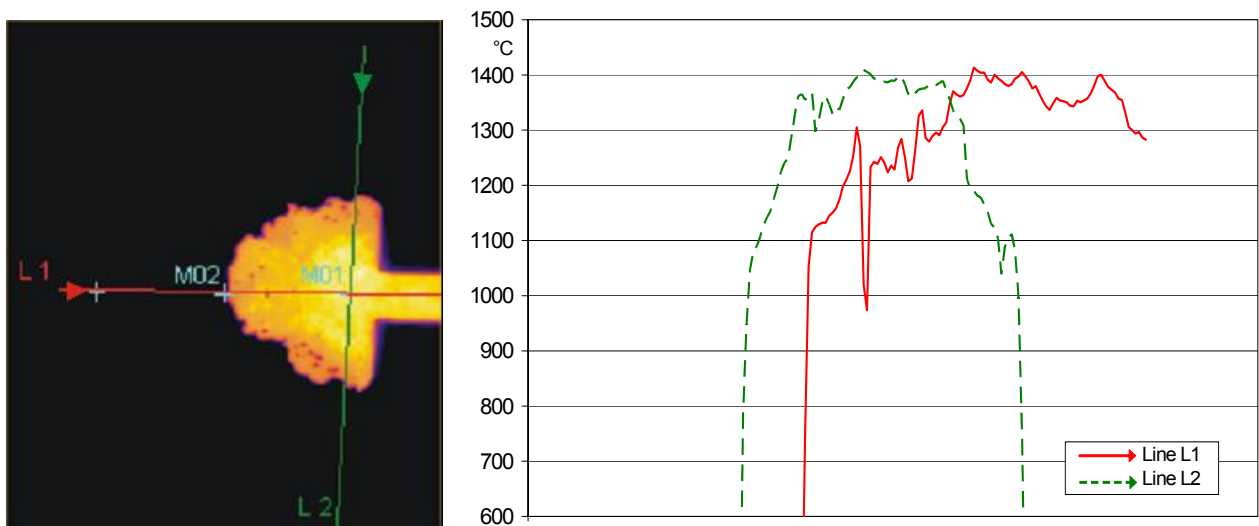
Figure 3-28: Surface temperature of the melt at 51,8 s [20 s] from infrared measurements
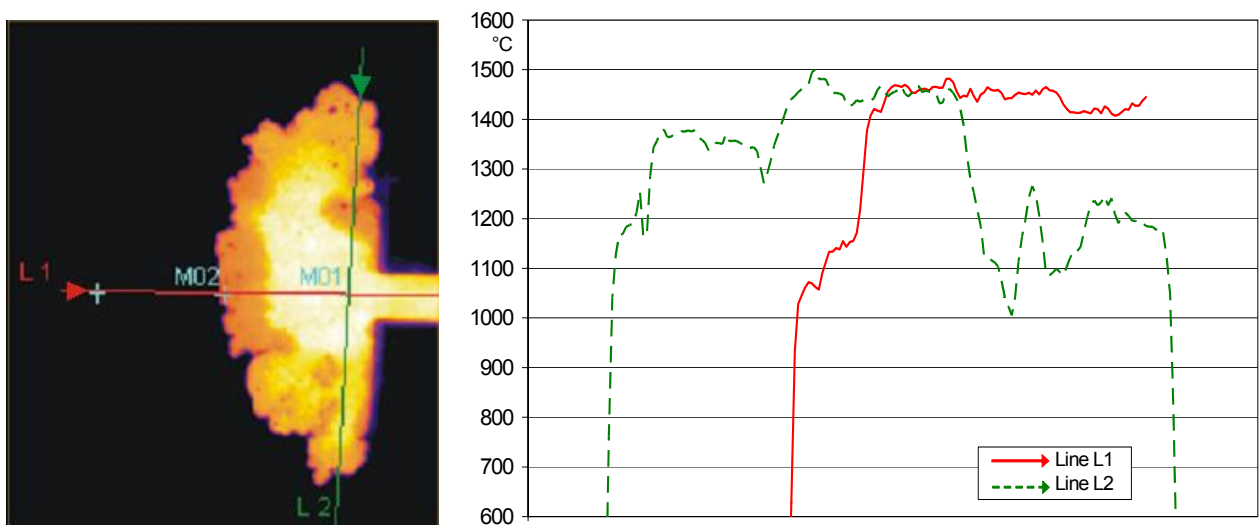
Figure 3-29: Surface temperature of the melt at 61,8 s [30 s] from infrared measurements
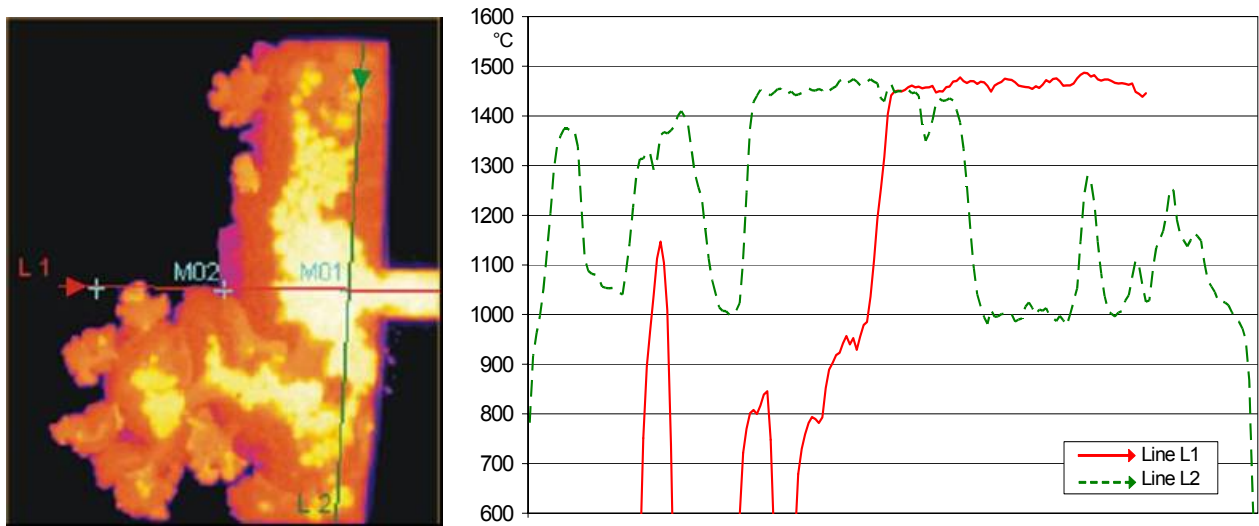
Figure 3-30: Surface temperature of the melt at 126,0 s [94.2 s] from infrared measurements

In addition, the temperature plots show a distinct low temperature plateau in the range of 1050 to 1150 °C clearly visible in **Figure 3-28** to **Figure 3-30**. This can be clearly identified with the existence of surface crusts. For this temperature plateau, the calculated solid fraction of the melt is 0.9 to 0.7.

It is highly interesting, that the surface of the spreading melt consists mainly of two regions that have either high or low temperature plateau (see **Figure 3-29** and **Figure 3-30**). These regions are identified as liquid melt (near onset of solidification) or high temperature crust, respectively, and confirm the calculated melt freezing range with respect to high and low liquid fractions.

These observations indicate that the melt flow during spreading is dominated on the one hand by distinct, relatively thin thermal boundaries with crusts and fluid with temperatures near the solidus temperature, and on the other hand by a high temperature bulk region that is near the liquidus temperature. This is the typical behaviour of the fluid flow with a higher Prandtl number, as for Pr > 1 the thermal boundary layer is thinner then the velocity boundary layer. For the actual melt, Prandtl number is near 50.
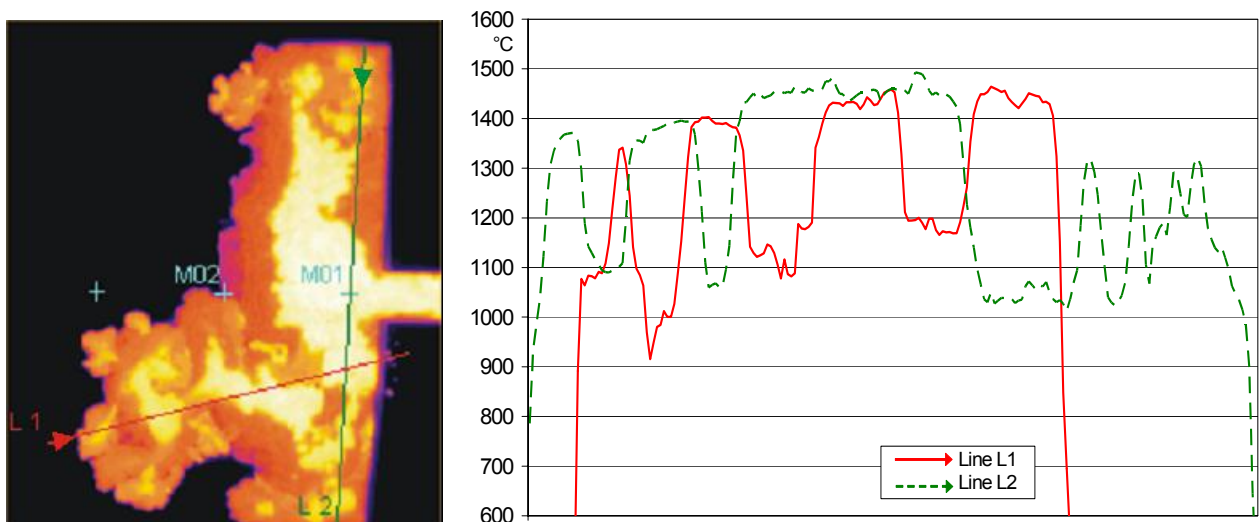
Figure 3-31: Surface temperature of the melt at 108.3 s [76.5 s] from infrared measurements

This is also confirmed by **Figure 3-31** which shows late outflow of melt through the front crust mainly along the line L1. This process occurred about 76.5 s after onset of spreading. The red solid line in the temperature plot shows that the surface temperature of the melt that moves towards the growing front is 1350 °C to 1400 °C. This temperature is only slightly lower than the maximum surface temperature near the outlet of the channel which is 1450 °C to 1480 °C, as shown by the line L2. This is the same behaviour as at the early spreading process, seen e.g. in **Figure 3-29**.

3.2.3.4 Temperature Distribution in the Concrete Substrate

The Ni-CrNi thermocouples NIWImi embedded in the concrete of the instrumentation modules were arranged in a staggered, uniformly spaced manner with distances of 2 mm as shown in **Figure 3-7** and **Figure 3-8**. They provided a spatial and temporal distribution of the temperature in the concrete, which is given in **Figure 3-32** and **Figure 3-33** for modules 1 and 2, respectively. As the thermocouples remained intact, they give reliable results and show typical temperature histories based on transient heat conduction. Beside the time delay due to the higher distance from the concrete surface, the curves of module 1 show by flattening at about 110 °C the influence of the evaporation of water that was present in the pores of the concrete. In module 2 the measured temperatures are considerably lower as module 2 was only partly covered by the spread melt. Consequently, the measurements have only qualitative information. Disturbances at 390 s are interpreted as a result of ablation of the solidified melt layer from the concrete which was caused by the shrinking process of the melt.
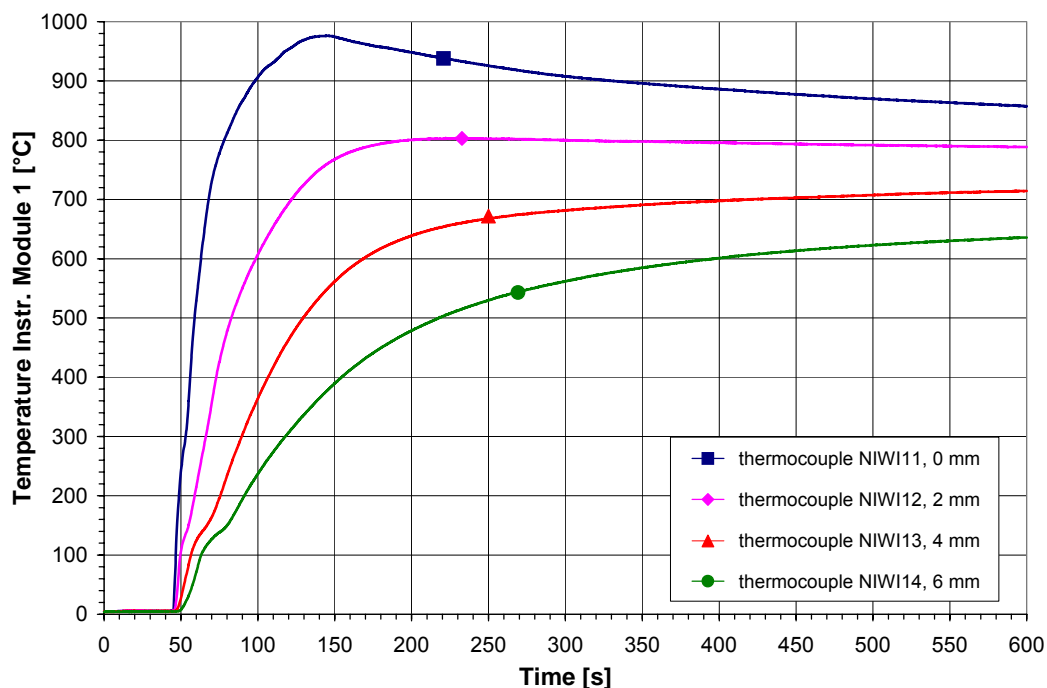
Figure 3-32: Temperature distribution in the concrete substrate at instrumentation module 1
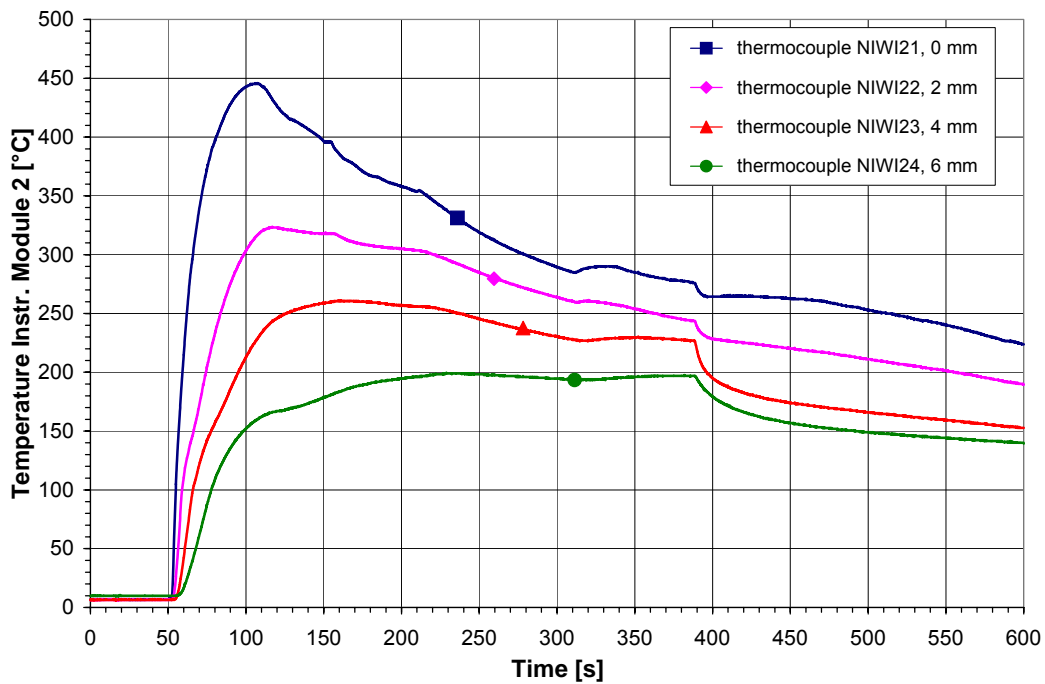
Figure 3-33: Temperature distribution in the concrete substrate at instrumentation module 2

3.2.3.5 Calculation of the Temperature Distribution in the Concrete

Time distribution of the temperature in the concrete at thermocouple module 1 which is shown in **Figure 3-32** allows the calculation of the corresponding heat flux to the concrete surface. This requires the solution of the inverse heat conduction (IHC) problem where the acting boundary conditions, especially the heat flux, have to be determined by means of their measured effects in the depth of the concrete depending on location, temperature, and time. The problem was solved with a numerical method according to J. V. Beck [7], where the time integration is stabilized by a special regulation procedure (computer code SINCO). With the applied code only a first approximation of the heat conduction problem is possible. To assess the obtained result, the calculated surface temperature was used in a second step for a standard transient heat conduction calculation, where the results are compared with the measured concrete temperatures. This control is useful because of the tendency of the IHC solving methods to become unstable.

Another problem in application of the IHC solver is the change of the concrete properties during heat-up. Furthermore, the evaporation of the water contained in the pores of the concrete caused a hold-up in the temperature rise. This phenomenon shows up like an inhomogeneous material behaviour during the heating process. Another heat absorbing process that takes place during the heat-up is the chemical decomposition of the cement matrix. The weakness of the actual program version, where only constant material properties are accepted, requires the treatment of a short term phase with the properties of normal concrete and a long term phase using modified values for a changed concrete with a lower thermal diffusivity.

Figure 3-34 shows the experimental temperature data conditioned by carefully smoothing for their further use in short term IHC calculation. This pre-processing is necessary to avoid strong fluctuations due to the amplifying effect of the solving procedure. Because of the finite expansion of the thermocouple tip, the location of the uppermost thermocouple was specified at 0.2 mm below the surface.

45
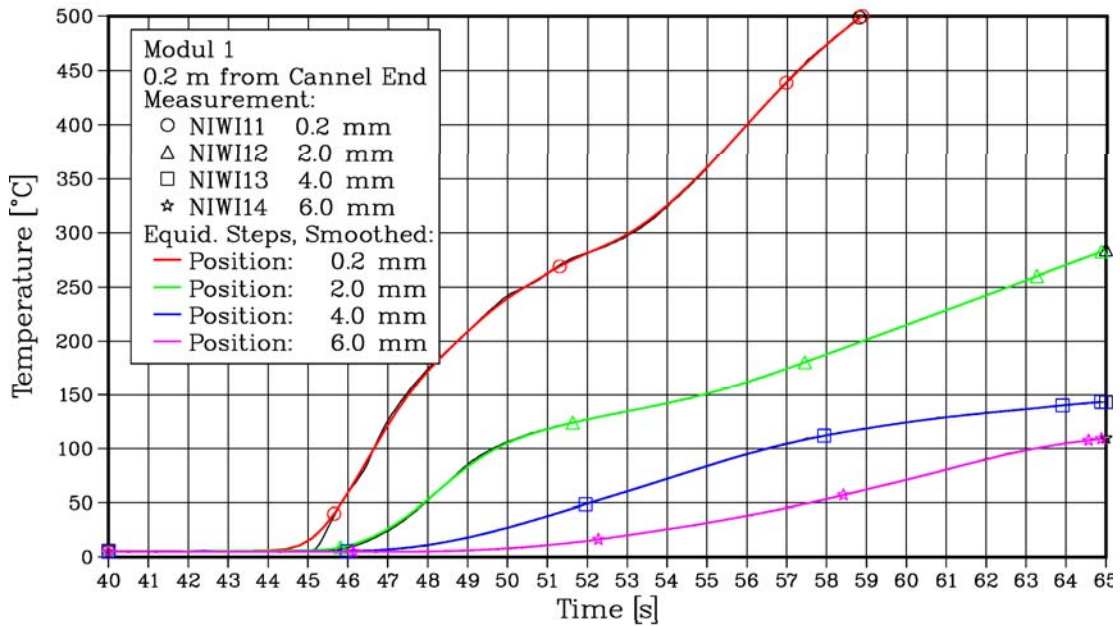
Figure 3-34: Experimental Input for the Inverse Heat Conduction Calculation - Module 1

The results of the IHC calculation are presented in **Figure 3-35** labelled with "SINCO", and compared with the corresponding measurements. Up to t = 49 s the agreement between calculation and measurement is excellent. However, as shown by the temperature hold-up, the water evaporation after 49 s acts like a heat sink and leads to a significant deviation between calculation and experiment in the uppermost concrete layer. Therefore, only the calculated values in the time span between 44 and 49 s can be considered as meaningful. This is also true for the calculated heat flux to the concrete surface in

Figure 3-36. After 49 s, the SINCO IHC calculation reduces the heat flux to compensate for the non existing heat sink of water evaporation in the code. With this artificial reduction, the measured temperatures in the lower concrete layers can be reproduced reasonably, but the heat flux is of course underpredicted after 49 s. The maximum heat flux amounts to about 220 kW/m^2 at t = 48 s, as shown in **Figure 3-36**.
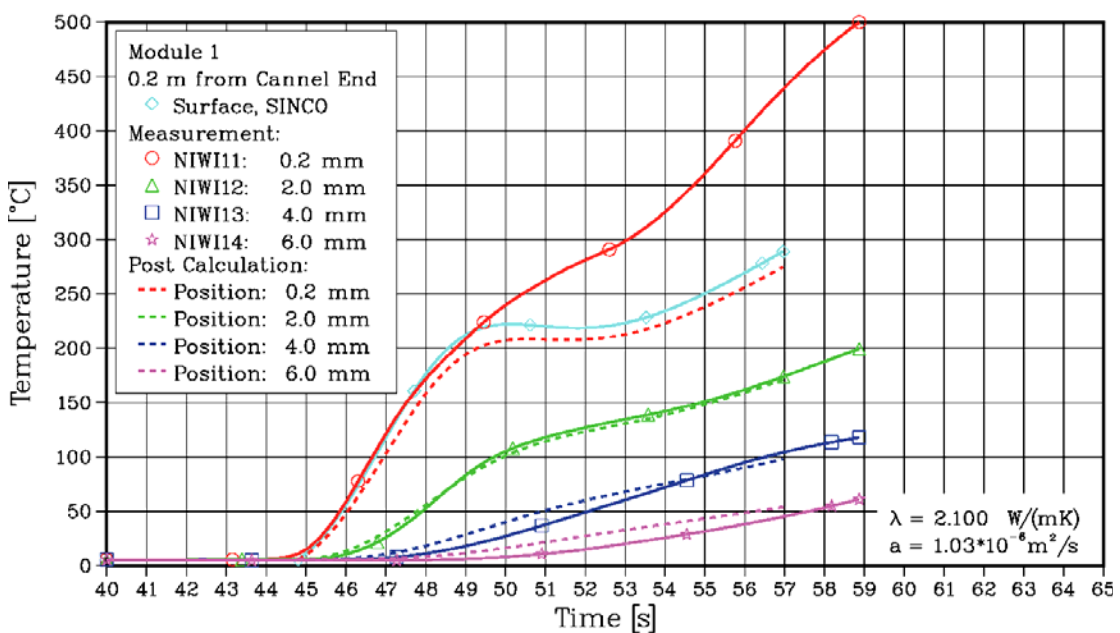
Figure 3-35: Results of the Inverse Heat Conduction Calculation - Module 1

46
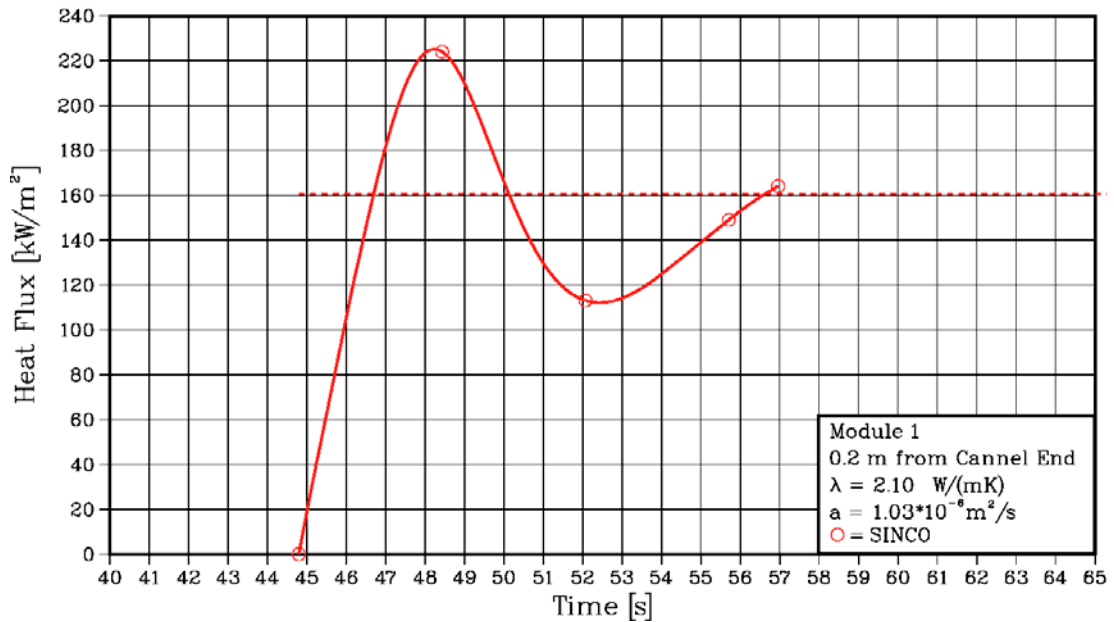
Figure 3-36: Calculated Heat Flux to the Concrete Surface with Short Term Concrete Properties

Whereas the standard value for the thermal diffusivity of concrete (a = $1.03*10^{-6}$ m^2/s) provides a reasonable, self-consistent result in the short term analysis, as shown in **Figure 3-35**, this is not the case for the long term calculation. **Figure 3-37** presents significant differences in the time behaviour between measurement and analysis. The theoretical curves are much closer together which gives evidence that a lower thermal conductivity should be used for theoretical analysis.
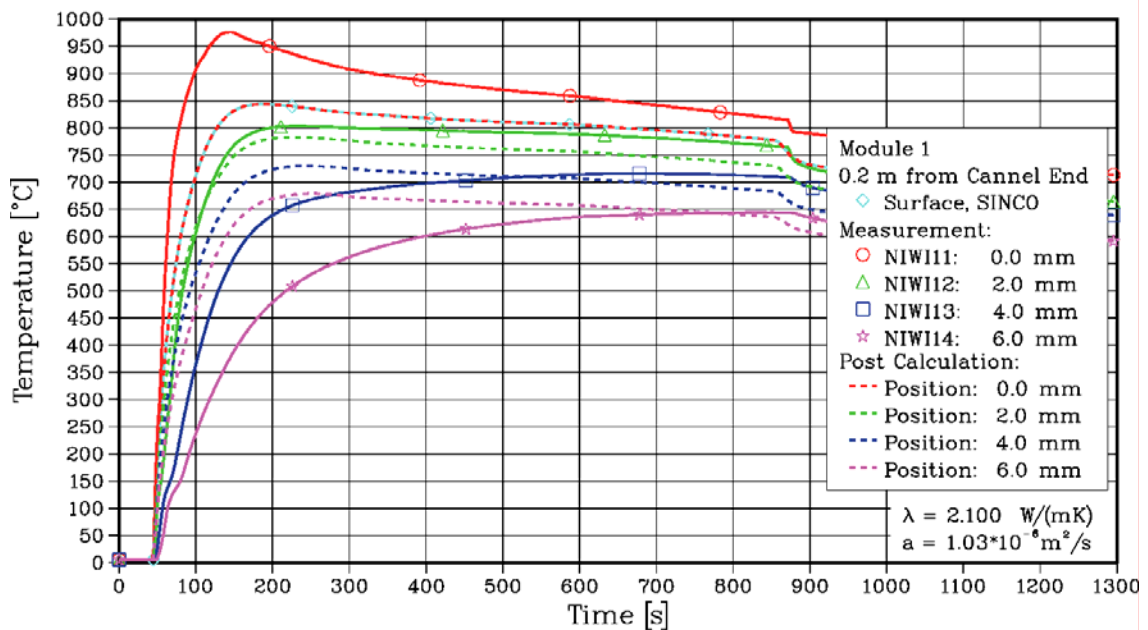
Figure 3-37: Long Term Results with Standard Properties of Concrete

A better representation of the experimental data succeeds with a value a = $0.3*10^{-6}$ m^2/s as shown in **Figure 3-38**. A reduction of the thermal conductivity (and hence of the thermal diffusivity a) of high temperature concrete is indeed expected because of the decomposition of the cement matrix of the concrete which results in a more porous structure. In addition, these endothermic chemical reactions in the concrete absorb energy which in context with the calculations of transient heat conduction could be taken into account by an increased effective specific heat of the concrete. In **Figure 3-38** also

47

the individual thermocouple positions are slightly modified compared to the specified locations in order to obtain an optimal agreement. However, it is noted that these adjustments are in the range of the manufacturing accuracy.
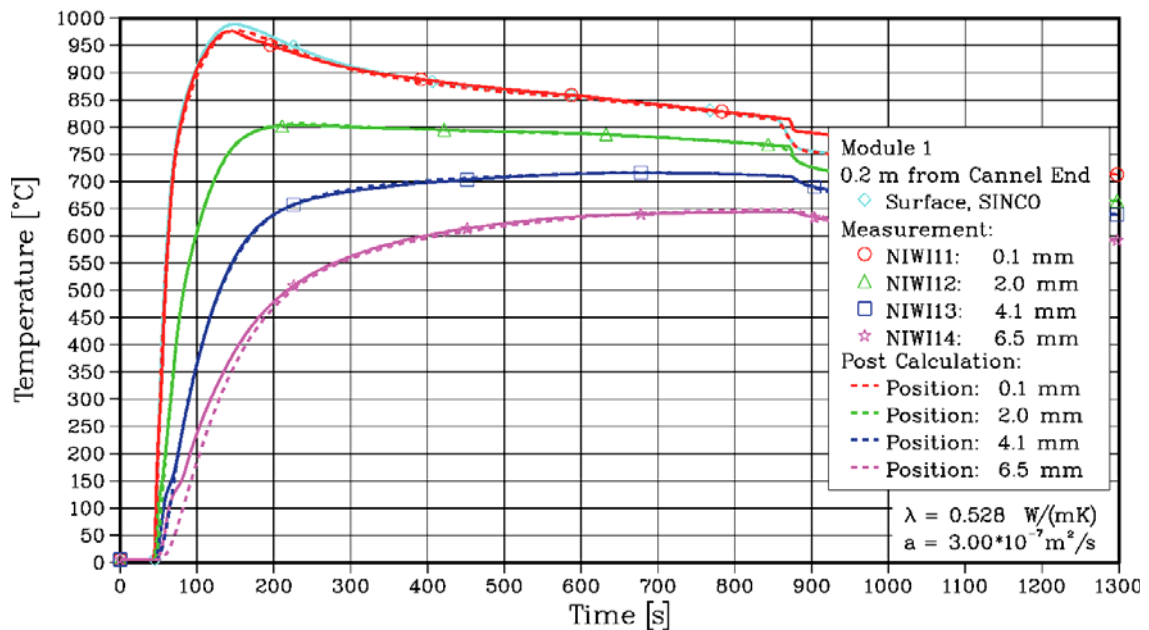
Figure 3-38: Long Term Results with Modified Concrete Properties

The calculations mentioned above assume, however, constant material properties of the concrete, whereas in reality the properties change with temperature. Therefore, the calculations are an approximation even after an optimised modification of the properties. Consequently, the heat flux to the concrete surface that was derived from the IHC calculations can be considered as a first order approximation only. The estimated heat flux for the long term analysis, shown in **Figure 3-39** is valid after about 200 s and gives a plausible impression of the later heat flux. The better estimate of the maximum heat flux of about 220 kW/m^2 is given in **Figure 3-36**. The disturbance at t = 860 s is a result of the separation of the solidified melt layer from the concrete. The unequal shrinking progress in oxide and concrete leads to this separation associated with the formation of an air gap.
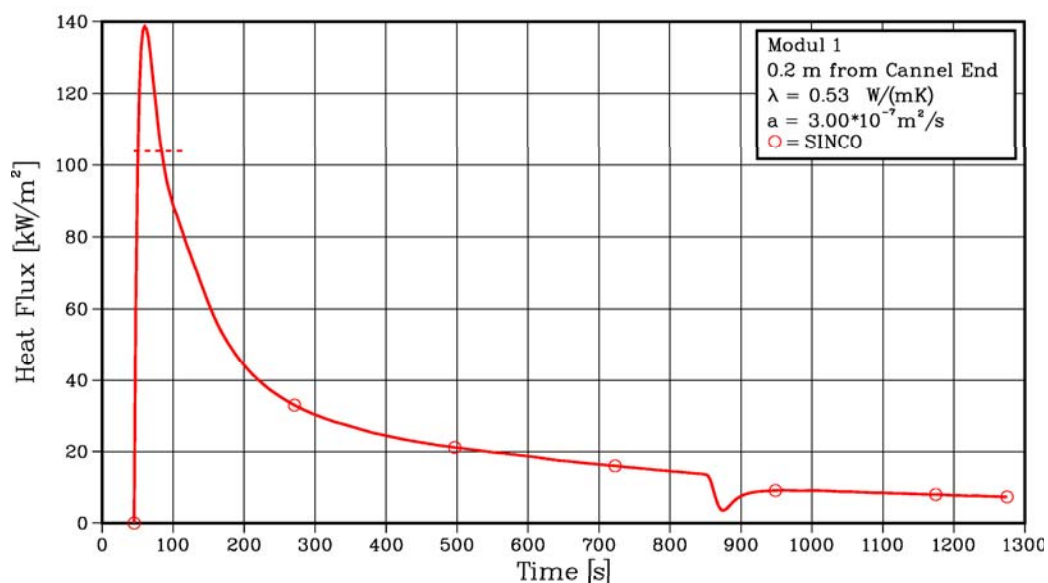
Figure 3-39: Calculated Heat Flux to the Concrete Surface with Long Term Concrete Properties

48

Figure 3-40 shows the temperature distribution in the concrete layer in the form of temperature profiles at different times, according to the above calculation. It is evident that penetration of the high temperature into the concrete is a slow process.
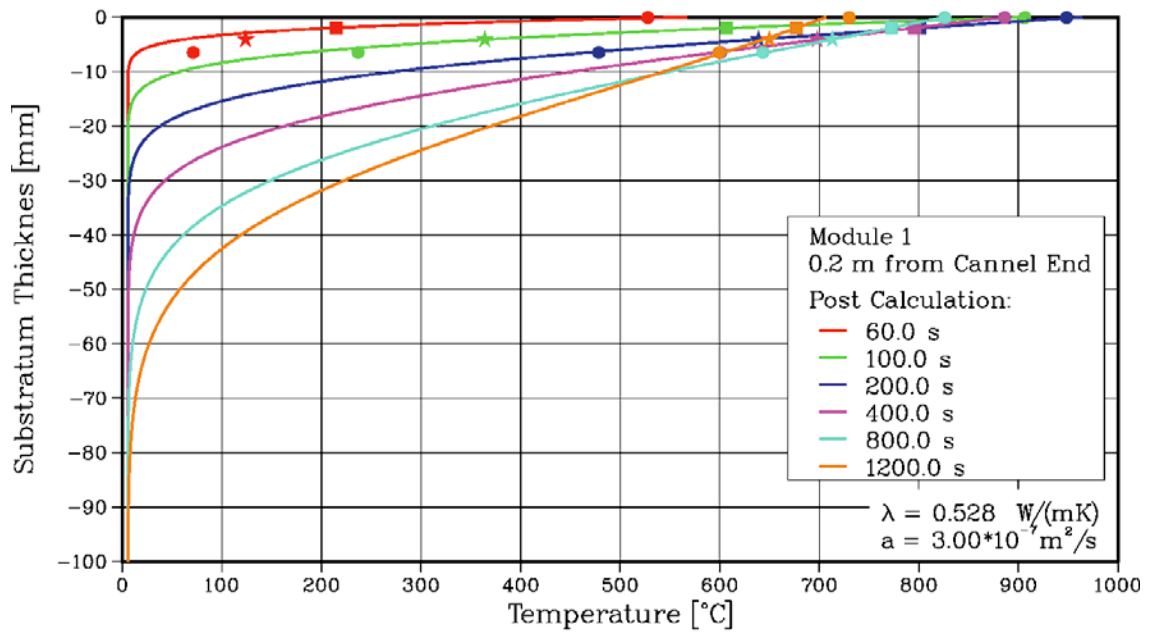
Figure 3-40: Temperature Distribution in the Concrete Layer

3.2.4 Post Test Analysis

3.2.4.1 Structure of the solidified Melt

Figure 3-41 shows the surface of the melt in the supply channel at the beginning and at the end of the channel. The surface at the entrance of the channel is more uneven than at the outlet, probably because of the higher thickness of the melt layer which caused longer concrete erosion.

Start of channel near the whirl basin   End of channel at the 2-d area

Figure 3-41: Contour of the melt in the supply channel after cool down

Figure 3-42 and **Figure 3-43** give the structure of the solidified melt surface on the 2-d spreading area. In these pictures two different structures are visible: (1) relatively even crusts which were formed early during spreading, and (2) regions with very uneven surfaces. These are the areas, where the melt surface remained liquid until to the end of melt inflow and which are clearly identified in **Figure 3-12**, **Figure 3-19** and **Figure 3-30** as high temperature areas. The characteristic surface structure results from the pertinent gas production during solidification which is the consequence of concrete decomposition, producing a multitude of small hills and small volcanoes. They are partly hollow, and some of them have small openings at the top. The diameters of the volcanoes are about 50 – 60 mm. Beyond the maximum elevations of 75 to 85 mm, the distances from the valleys to the peaks are typically 25 to 45 mm. The spacing of the volcanoes corresponds to the centres of gas release from the concrete surface.

The thickness of the solidified melt on the concrete surface has been measured at several positions. In spite of the irregularities, the melt has in a wide range a relatively even thickness of 50 to 60 mm. At the concrete sidewalls which surround three sides of the spread melt, the thickness of the melt goes down to only 45 - 30 mm in a transition region that is about 40 mm wide. The plausible explanation is that the surface crust that

50

was formed during the early spreading period was lifted by the ongoing increase of the height of the melt with the exception of that region of the crust that was anchored to the sidewalls. At the free melt front on the left side of the figures the thickness of the melt reduces from 50 to 10 mm over a transition range of 80 to 120 mm. This part of the melt is uniformly covered with small particles of concrete with sizes of 1 to 3 mm. These particles which can be seen in **Figure 3-42**, in **Figure 3-43** and in **Figure 3-47** are small, unmelted fragments of the uppermost concrete surface decomposed by the hot melt.

Figure 3-42: Right side of the spread melt after cool down
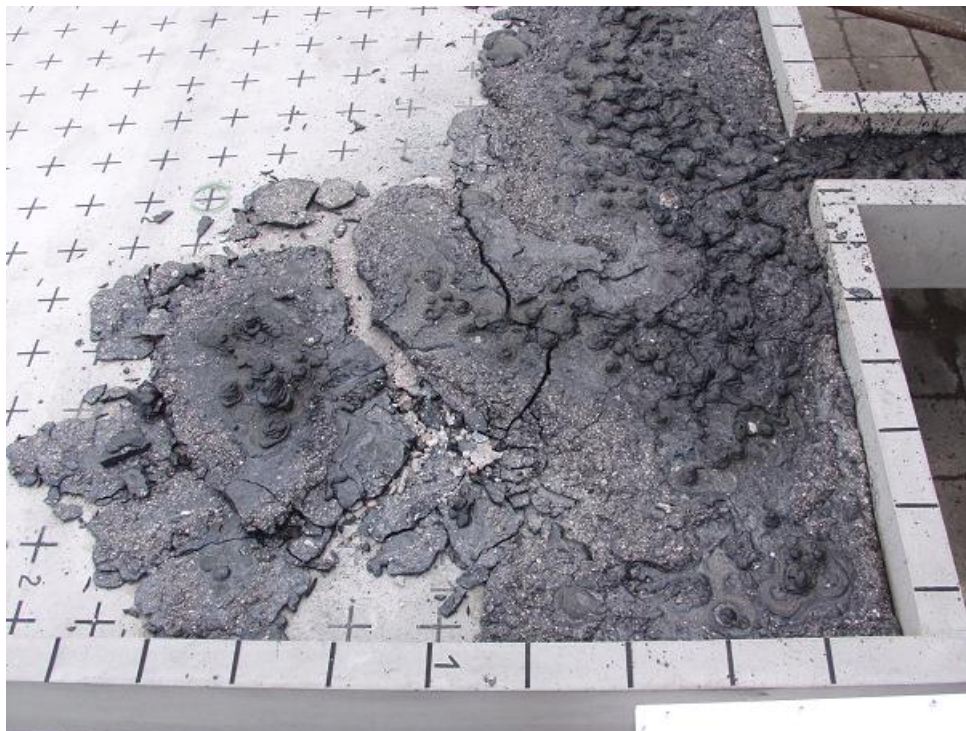
Figure 3-43: Left side of the spread melt after cool down

3.2.4.2 Cross Section and Porosity of the Melt

The following pictures give an impression of the inner structure of the solidified melt. To inspect the structure (porosity, thickness etc.) at different positions, the melt area has been broken into several parts as shown in **Figure 3-44**. **Figure 3-45**, **Figure 3-46**, and **Figure 3-47** show that the configuration of the melt varies only slightly at different positions. In general, the porosity of the melt is higher in the upper and in the lower layers with inclusion of gas bubbles of ~1 cm size, whereas the intermediate layer (about 60 % of the total thickness) has a relatively homogeneous consistency with fine porosity. All porosities are closed porosities with only few exceptions that have openings through the upper surface. The accumulation of gas bubbles in the upper layer can be explained by the early formation of the surface crust which excludes penetration of bubbles through the upper surface

Figure 3-44: Profile of the melt in the middle near the supply channel of ECOKATS-1 with fracture lines for the inspection

Figure 3-45: Cross section of the melt at the right concrete border at x = 30 cm

Figure 3-46: Cross section of the melt in the middle at x = 50 cm

Figure 3-47: Cross sections of the melt at x = 40 cm, y = -60 cm

As further representatives of the cross sections, three specimens from different positions of the melt are given in **Figure 3-48**. Specimens 1 and 2 have been taken from the middle of the left area of the spread melt and show the general consistency as described above. Specimen 3 is from the front part in the middle of the broken furthermost plate with a higher porosity. In this specimen also a small part of unmolten concrete can be seen, enclosed in the upper layer.

Specimen 1
Position x = 44 cm, y = 80 cm

Specimen 2
Position x = 50 cm, y = 70 cm

Specimen 3 from position x = 165 cm, y = 75 cm

Figure 3-48: Sections of specimens from different positions in the melt of ECOKATS-1

3.2.4.3 Erosion of Concrete

Because of the relatively cold oxide melt and the lack of heating, the erosion of the concrete substrate was very small. A maximum penetration depth of about 2 mm was reached on the spreading surface in the central, uneven region of **Figure 3-42** and **Figure 3-43**). In the outer more even region only the thin smooth finishing layer of cement of about 1 mm thickness was decomposed and partly transferred to the upper melt surface as described above (see e.g. **Figure 3-47**).

In the supply channel, the erosion could be easily inspected at the beginning of the channel where the whirl basin was mounted. It is obvious that here the erosion is maximum because of the long term supply of the hot melt flow. After removing the whirl basin it was observed that the edges direct in contact with the whirl basin were not changed noteworthy. About 75 mm behind these edges the maximum erosion depth was reached. The geometry of the supply channel after the test is shown in **Figure 3-49**. The edges of the channel have been rounded and the following maximum erosion values were measured:

On the left wall	16 mm,	110 mm from above
On the right wall	14 mm,	95 mm from above
At the bottom	15 mm,	in the middle

Full section of the channel   Right edge of the channel

Figure 3-49: Erosion of concrete at the entrance of the supply channel

4 Properties of the Melt

4.1 Melt Composition and dominant crystals determined by different institutions

The composition of the oxide melt has been determined after the test by high accuracy x-ray fluorescence analysis [4]. In **Table 4-1** the composition of the thermite mix as used for the EKOKATS experiments and the resulting melt composition per 100 kg oxide simulant melt are listed. For the composition of the oxide melt, the basic oxides are given. This does not preclude, that the oxides exist in the form of more complex compounds. For code application, use of the composition in **Table 4-1** is recommended.

Table 4-1: Mix of thermite powder and generated melt composition per 100 kg simulant oxide melt for the ECOKATS experiments

Constituent	Pre-Reaction	Post-Reaction
Thermite Mixture		
Aluminium thermite 10 Al SSH [1]	86.04 kg	
CaO [2]	21.00 kg	
SiO_2 [3]	15.00 kg	
Fe_2O_3 [4]	14.00 kg	
total:	136.04 kg	
Oxide Melt [5]		**100 kg**
Al_2O_3		41 %
CaO		19 %
FeO		24 %
SiO_2		16 %
Metal Melt [6]		**36 kg**
Fe		~100 %
Si		<0.24 %
Al		<0.30 %
C		0.005 %
Mn		0.01 %

[1] Supplier: Elektro-Thermit, Essen
[2] Burned lime, >98 % CaO, 0-6 mm, supplied by Rheinkalk GmbH, Wülfrath
[3] Quartz sand, >96 % SiO_2, 0.4-0.8 mm, supplied by Friedrich Quarzsandwerke, Eggenstein
[4] 98-99 w-% Fe_2O_3, supplied by Imhoff und Stahl GmbH, Mannheim
[5] XRF analysis, June 2003, C. Adelhelm , Forschungszentrum Karlsruhe-IMF1 [4]
[6] Chemical analysis PD03005 with spark spectrometer, 17.1. 2003, Siemens Bruchsal

The detailed analysis of the oxide samples by x-ray fluorescence analysis is given in **Table 4-2**. It shows that the melts in ECOKATS-V1 and ECOKATS-1 are practically identical and very homogeneous. Admixture of concrete constituents from the concrete substrate is negligible, as seen by comparison of "early" and "late" freezing samples.

Table 4-2: Composition of oxide melt in ECOKATS-V1 and -1 from high precision x-ray fluorescence analysis [4]

Analysis No.		200/2003	201/2003	202/2003
Constituent	**calibration range of reference sample** wt-%	**ECOKATS-V1 melt on cordierite** wt-%	**ECOKATS-1 melt on concrete "early freezing"** wt-%	**ECOKATS-1, melt on concrete "late freezing"** wt-%
Al_2O_3	26 - 36	40,91 ± 0,05	40,34 ± 0,20	40,64 ± 0,03
CaO	19,7 –25,7	19,05 ± 0,05	17,70 ± 0,03	18,06 ± 0,01
Cr_2O_3	0 – 0,4	0,12 ± 0,01	0,12 ± 0,01	0,11 ± 0,005
FeO	23,8 – 32,2	23,73 ± 0,04	24,46 ± 0,05	24,6 ± 0,07
K_2O	0 – 0,4	0,081 ± 0,004	0,12 ± 0,005	0,13 ± 0,005
MgO	0 – 0,4	0,56 ± 0,01	0,53 ± 0,005	0,55 ± 0,01
Mn_3O_4	0,3 – 0,7	0,53 ± 0,005	0,53 ± 0,01	0,54 ± 0,005
SiO_2	14 - 20	15,55 ± 0,02	15,56 ± 0,06	16,12 ± 0,02
total		100,5	99,4	100,8

The analysis confirms the XRF analysis performed at Würzburg University during the selection and preparation of the thermite mixtures [2]. Further chemical analyses were performed by LRST at Aachen University [8] and CEA Cadarache [9] using EDX and XRD methods, respectively. These analyses have a lower accuracy, with an error that is specified between 3 and 5 %. These data are listed in **Table 4-3**. The deviation from **Table 4-2** is within the experimental error band.

Table 4-3: Composition of oxide melt (wt-%) in ECOKATS test measured by EDX and XRD

Constituent	**LRST [8] ECOKATS-V1 EDX**	**LRST [8] ECOKATS-1, EDX**	**CEA Cad.[9] ECOKATS-1, EDX**	**CEA Cad.[9] ECOKATS -1, XRD**
Al_2O_3	39,2	36,2	32,0	39
CaO	21,4	23,0	24,9	16
FeO	23,1	21,2	22,1	27
SiO_2	16,3	19,7	21,1	19
total	108	107,1	108,1	109

To determine the composition of the solidified melt as function of the depth, LRST at Aachen University [8] has performed EDX analysis of 20 and 16 samples taken in different positions from the surface of ECOKATS-V1 and ECOKATS-1, respectively. **Figure 4-1** shows only minor variations of the atomic composition vs. depth of the layer, as the short time for solidification does not allow segregation of different chemical phases and the establishment of chemical equilibrium. However, due to the faster solidification velocities in the upper and lower layer as compared to the bulk of the spread melt, finer and denser dendrite structures are found near the upper and lower surfaces. For a more detailed description see [8].
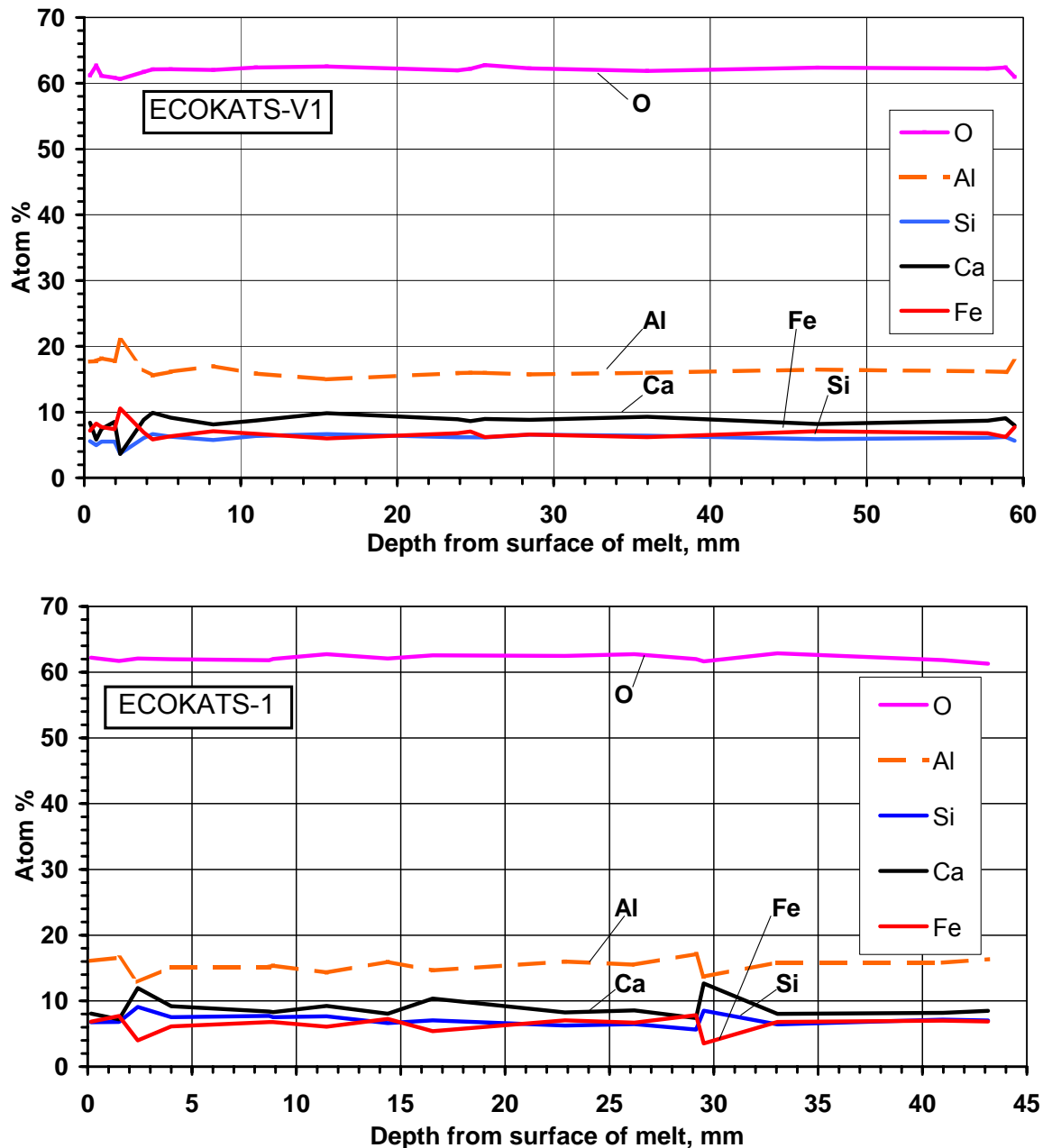
Figure 4-1: Elementary composition profile of the solidified oxide melt layer vs. depth in ECOKATS-V1 and ECOKATS-1

Further analysis of the solidified melt has identified the solid as a crystalline mixture. By microprobe analysis, Würzburg University describes the bright matrix crystals as Ca-Al-silicates with a small amount of Fe, and the dark quench crystals as a variety of spinelle that is similar to Gercynite [2]. According to XRD-analysis of LRST at Aachen University [8], the main components are Gehlenite [$Ca_2Al_2SiO_7$], Diopside [$Ca(Mg,Al)(Si,Al)_2O_6$], and Hercynite [$FeAl_2O_4$]. Semi-quantitative XRD analysis by CEA Cadarache [9] of the ECOKATS-1 solidified melt is summarized in **Table 4-4**. The different analyses agree with respect to the dominant crystalline phases. Comparison with GEMINI calculations performed by CEA Cadarache in **Table 4-4** show some deviations from the thermody-namic equilibrium which is the necessary condition for thermodynamic calculations. Nevertheless, the small deviations should allow an acceptable estimation of the freezing range of the melt from GEMINI calculations.

58

Table 4-4: Semi-quantitative XRD analysis of ECOKATS-1 solidified melt

Crystalline Phases		XRD wt-%	GEMINI 2 calculation wt-%
Hercynite	$FeAl_2O_4$	39 % $\pm$ 8 %	40
Gehlenite	$Ca_2Al_2SiO_7$	34 % $\pm$ 7 %	45
Anorthite	$CaAl_2Si_2O_8$	7 % $\pm$ 1 %	10
Quartz low	SiO_2	9 % $\pm$ 2 %	-
Magnetite	Fe_3O_4	6 % $\pm$ 2 %	-
Iron	Fe	< 3 %	-
Al-Fe-silicate	$Al_{0.7}Fe_3SiO_3$	< 3 %	-

4.2 Freezing range of the Melt

As stop of spreading is controlled by onset of solidification, the freezing range of the multi-component melt is of key importance. The fraction of solid crystals that grow in the solidifying melt in the freezing range increases the viscosity of the "slurry". With growing fraction of crystals the mixture of melt and crystals becomes immobile, or eventually a solid crust has formed.

A theoretical estimate of the freezing range is calculated by Forschungszentrum Karlsruhe with the GEMINI code and the THERMODATA data set [3], starting with the idealized components of the oxide melt of 41 wt-% Al_2O_3, 24 wt-% FeO, 19 wt-% CaO, and 16 wt-% SiO_2, as specified in **Table 4-1**. GEMINI determines the composition for a specific temperature and pressure of the melt by minimizing the Gibbs energy of the multiphase system. This assumes that the melt is in thermodynamic equilibrium. The GEMINI results given in **Figure 4-2** show that solidification takes place in the wide temperature range from 1820 K – 1270 K (1550 °C to 1000 °C). 50 mass-% of the melt are solid at 1600 K (1330 °C).
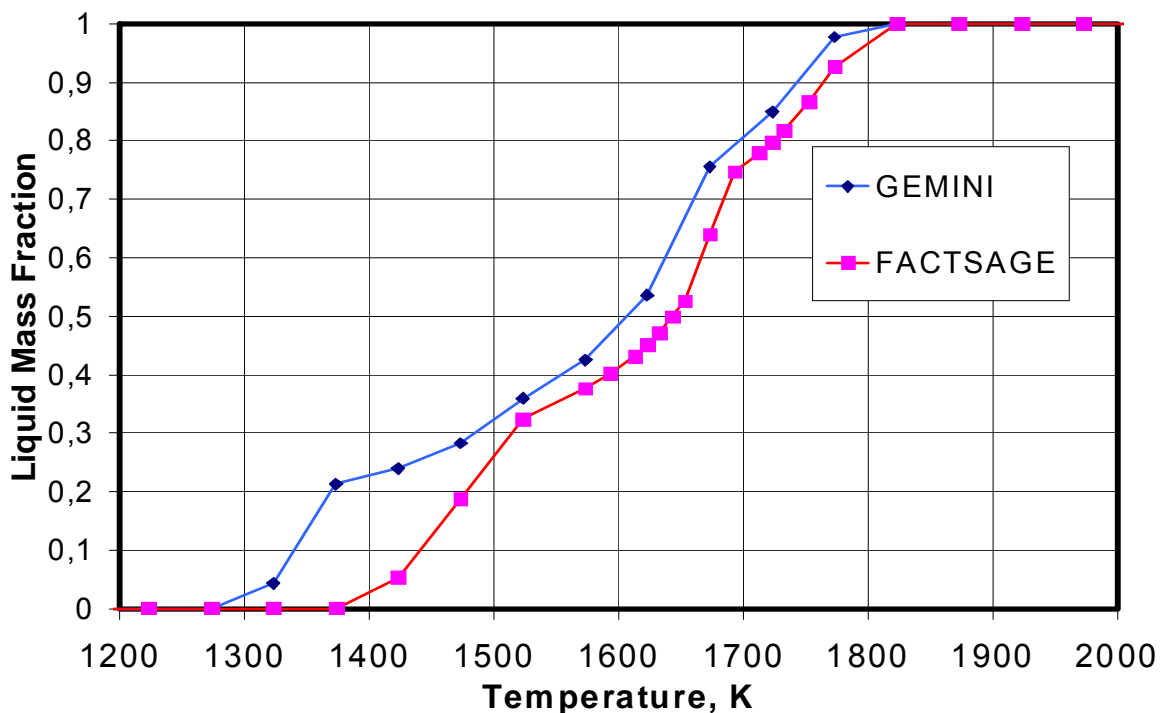
Figure 4-2: Freezing range of the oxide melt calculated with GEMINI and FACTSAGE

Additionally in **Figure 4-2** the calculation with the FACTSAGE code [10] performed by GRS is plotted, which predicts that the solidification range would be shifted to higher temperatures by some 50 K. As these data are the best representation of characteristic temperatures of the melt, which were determined in separate experiments described below, the FACTSAGE data are recommended for use in code calculations.

According to additional GEMINI-2 calculation by CEA Cadarache with a modified thermo-chemical data set [9], the freezing range would be reduced to the temperature interval between 1750 K and 1400 K (**Figure 4-3**) being in good agreement with the FACTSAGE results. This figure also gives the concentration of different types of crystals that grow during solidification.
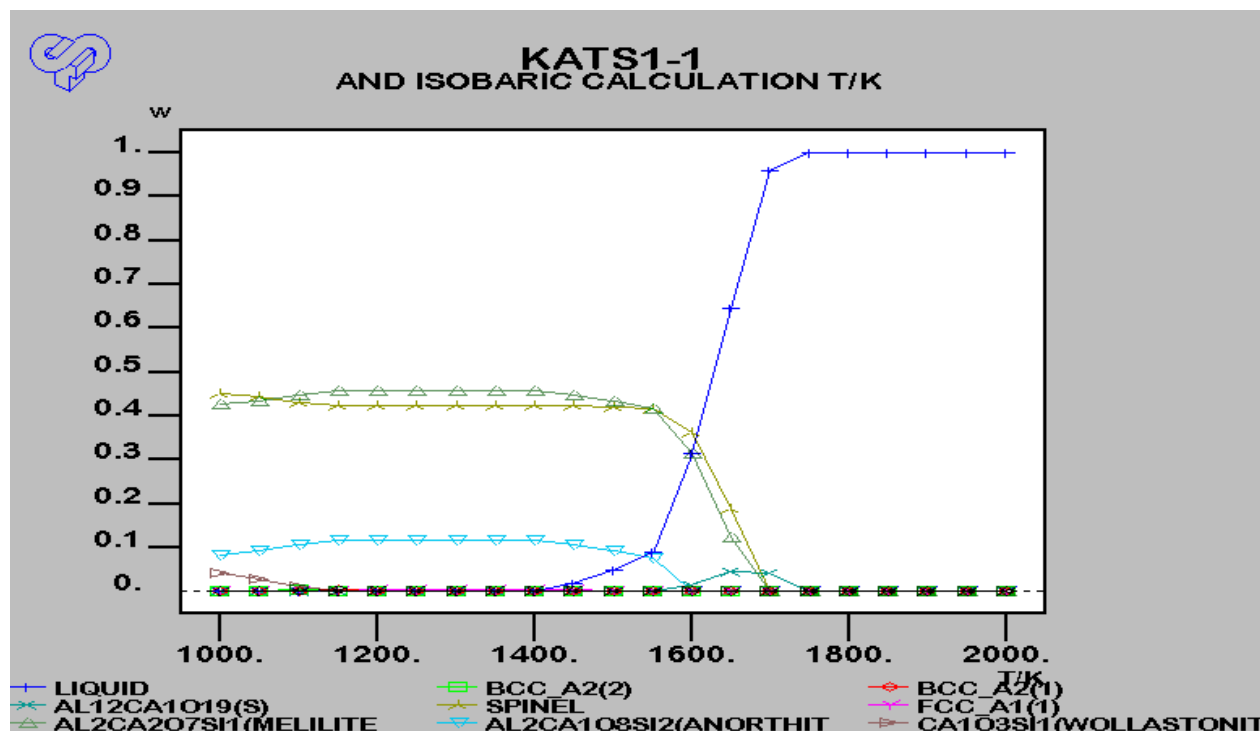
Figure 4-3: Freezing range and types of crystals calculated by GEMINI-2

It is extremely difficult to measure the characteristic temperatures of the melt during solidification. The following experimental information from post-test melt analyses were contributed from different institutions:

1. Würzburg University found that at 1400 °C (1673 K) it was not possible to insert the rotating shaft of a viscometer into the heated "melt" [2]. It is therefore concluded, that the liquid fraction at 1673 K is too low so that the melt is a slurry with a significant solid fraction. According to the FACTSAGE curve in **Figure 4-2** the solid fraction would be in the range of 35 wt-%.
2. Aachen University determined in a DTA apparatus a pronounced peak at 1291 °C during heat up and at 1308 °C during cooling of a melt sample. No further peaks were detected up to 1550 °C (1823 K). Post test inspection of the DTA crucible, however, suggests that the liquidus temperature (liquid fraction = 1) is below 1550 °C [8]. The DTA peak near 1300 °C = 1570 K is in the region of the steep increase of the liquid fraction in **Figure 4-2** and **Figure 4-3**.
3. Aachen University also investigated (partial) melting of a cylindrical oxide probe in a heating microscope up to 1450 °C [8]. First slow reduction of the diameter of the cylinder starts near 1320°C = 1593 K, which may indicate formation and relocation of

60

liquid melt fractions in a crystal structure. According to **Figure 4-2**, the liquid fraction would be close to 40 %.

Major partial melting was observed starting at 1435 °C = 1708 K, where the cylindrical probe deformed by a slow flow process from the original cylindrical shape to a bell-shaped form that has 55 % of the original height of the cylinder thus indicating presence of some residual crystals in the melt. This behaviour is in agreement with the 25 % residual crystal fraction in the melt that is predicted by the FACTSAGE calculation in **Figure 4-2**.

In summary, these observations support the FACTSAGE freezing curve in **Figure 4-2**, which is therefore recommended to be used for code calculations, see **Table 4-5**.

Table 4-5: Recommended solidification range of the melt as calculated by FACTSAGE

Temperature K	Liquid fraction wt-%	Temperature K	Liquid fraction wt-%
1373	0.000	1653	0.526
1423	0.054	1673	0.640
1473	0.188	1693	0.747
1523	0.325	1713	0.779
1573	0.377	1723	0.798
1593	0.402	1733	0.818
1613	0.432	1753	0.867
1623	0.451	1773	0.926
1633	0.472	1822	1.000
1643	0.500		

4.3 Recommended Physical Properties of the Melt

Table 4-6 summarizes additional physical properties of the melt [5, 6].

Table 4-6: Properties of the oxide melt in the Experiments ECOKATS-V1 and ECOKATS-1

Property	Value	Comment
Density at 1600°C	3264 kg/m^3	determined from melt flow rate from thermite vessel
Viscosity μ_0 for T > T_{liq}	0.2 Pa $\cdot$ s	from ECOKATS-V1 for T = 1893 K
Viscosity in freezing range	$\mu/\mu_0 = (1-x/x_{max})^{2.5} \cdot \exp[0.04\,(T_{liq}-T)]$	Pinkerton/Stevenson, x = solid fraction, x_{max} = 0.5
Average specific heat	~1.2 kJ/(kg K)	for the temperature dependence see [5], [6]
Thermal conductivity	5.4 W/(m K)	for T $\geq$ 1500 K, see [5], [6].

The density of the liquid oxide melt was determined from the transition from metal to oxide outflow rates during melt release from the thermite vessel. The density of the oxide is therefore determined directly in the first test phase, and related to the well known

density of liquid iron. In addition, Aachen University measured the density of the cold, dense oxide as 3600 kg/m^3 [8], which is certainly higher than the liquid density.

The viscosity of the liquid melt could not be measured by Würzburg University in the available rotational viscometer, as 1400 °C did not generate sufficient fluidity. It was stated that at 1400 °C the viscosity >> 10^4 Pa · s.

The viscosity for $T>T_{liq}$ was determined from the spreading velocity of the melt in the first phase of test ECOKATS-V1 by comparing the calculated spreading velocity with the experimental values. This value is typical for a high temperature melt with high silica content.

The porosity of the solidified oxide, determined by Aachen University [8], is given in **Table 4-7**:

Table 4-7: Measured porosities of solidified melt

	total porosity	open porosity
ECOKATS-V1	40 %	10 – 20 %
ECOKATS - 1	50 %	30 –40 %

It must be kept in mind that the porosities were determined from small samples of a few cm only. Especially the open porosity is sensitive to the surface to volume ratio. The open porosity takes into account openings to all surfaces of the sample, not only to the top or bottom surface. As expected, gas release from the concrete in ECOKATS-1 increases the porosity.

With the collected property data, the oxide melt is well characterized as a high simulant melt.

5   Conclusions

The spreading experiments ECOKATS-V1 and ECOKATS–1 were performed as well-defined large scale experiments. They investigated spreading of oxide melts driven by low pouring rates. Both experiments used a multi-component oxide melt with a wide solidification range. The melt and the spreading conditions were selected to represent conditions for which incomplete spreading would occur, that is intermittent stop of spreading may occur during the period of melt release. The melt and initial conditions of the melt pour represent important aspects of ex-vessel melt release during a core melt accident, especially with respect to the wide solidification range of a multi-component oxide melt. This was achieved by a thermite-generated, multi- component high temperature melt that was released with relatively low melt overheat.

The experiment ECOKATS-V1 was performed as a spreading test in a 1-d flow channel of inert ceramic substrate. 193 kg oxide melt were released to the flow channel and spread over a length of 6.5 m. The test provides useful information over the characteristics of the melt, such as the initial viscosity and the rheological behaviour in the freezing range, and about the nature of the 1-d spreading process during onset of solidification and growth and failure of a front crust.

In the experiment ECOKATS-1, 547 kg oxide melt were released to a concrete surface that was 4 m long and 3 m wide. Degassing of the concrete during the initial spreading phase has an important effect on the spreading process as can be seen e.g. in the inlet flow channel in comparison with the ECOKATS-V1 test. Spreading on the large surface into the longitudinal direction already stopped after 1 m at 20 s, and was subsequently followed by a pronounced spreading towards the lateral walls and a series of smaller outflows of melt through the front crust, while the melt release continued until 85 s after the begin of spreading. The end of spreading was reached 15 s after end of melt release. The total area that has finally been covered by the spread melt is 4.88 m^2.

Detailed material investigations were performed to determine the important properties of the melt, especially with respect to its viscosity and its freezing behaviour which dominate the spreading process. With this additional information, the physico-chemical properties of the multi-component melt are well characterized.

In both experiments, spreading of the oxide melt is characterized by pronounced thermal boundary layers that exist at the free surface of the melt on the one hand, and at the surface of the concrete or ceramic substrate on the other hand. This leads to the formation of crusts, while the bulk of the melt remains at high temperatures. This is evident, because late outflows of melt through cracks in the front crust show still high temperatures of the melt. The crust on the upper surface and especially at the leading edge of the melt is indeed responsible for the stop of the spreading process. At these locations, the relevant crust growth is controlled mainly by radiation. In contrast, the bottom crust has only little effect on spreading as that crust is easily overflowed by the bulk of the melt. Furthermore, as the bottom crust limits heat transfer to the substrate, heat conduction in the substrate has only minor influence on spreading.

The experimental conditions are described and detailed results are given. Both experiments are being used for blind post-test calculations for validation of advanced spreading codes.

Literature

[1]   Alsmeyer, H., Cron, T., Foit J.J., Messemer, G., Schmidt-Stiefel, S., Häfner, W., Kriscio, H., Interim Report on Design, Preparation, and Basic Data of the Melt Spreading Tests ECOKATS-V1 and ECOKATS-1", SAM-ECOSTAR-D17, January 2004

[2]   Zimanowski, B, Büttner, R. "Bericht zu den Messungen an Proben aus Spreading-versuchen", Inst. für Geologie der Universität Würzburg, Physikalisch Vulkanologisches Labor, April 2003

[3]   GEMINI 2 Code for thermochemical equilibria calculation, Version 3.4 (2000), and TDBCR97 Thermodynamic Database, Thermodata Company, 38400 Saint Martin d'Heres, France

[4]   XRF Analysis 200/2003–202/2003, C. Adelhelm, T. Kaiser, June 2003, Forschungszentrum Karlsruhe-IMF1

[5]   Spengler, C., Foit, J.J., Häfner, W. "Data Set for the Blind Benchmark Calculation of the ECOKATS-V1 Spreading Experiment", July 2003, SAM-ECOSTAR-P09/01

[6]   Foit, J.J., "Spreading under variable viscosity and time-dependent boundary conditions: estimate of viscosity from spreading experiments", Nucl. Eng. and Des. 227 (2004) 239-253.

[7]   Beck, J. V.; Blackwell, B.; St. Clair, C. R., Jr, "Inverse Heat Conduction. Ill-posed Problems", Wiley-Interscience, New York, 1985

[8]   Alkan, Z., Sanei, N.; "Results of the post-test analyses on the samples from oxide-melt spreading experiments", SAM-ECOSTAR-P13/02

[9]   Piluso, P, Taraud, P.; "Post-mortem analyses of the ECOKATS-1 spreading test", SAM-ECOSTAR P03/22

[10] Bale, C.W., Chartrand, P. et al., "FACTSAGE thermochemical software and databases", CALPHAD, 26(2):189-228 (2002)

[11] Alsmeyer, H., Cron, T., Foit J.J., Messemer, G., Schmidt-Stiefel, S., Häfner, W., Kriscio, H., "Experiment ECOKATS-2 on Melt Spreading and Subsequent Top Flooding", SAM-ECOSTAR-D14/16 and D39/40, May 2004

Appendix A   ECOKATS 1 Instrumentation Plan

A.1   Instrumentation Code

This table gives a short description of the sensor abbreviations and of the sensor locations

Abbreviation			Description
Char 1 - 4	**Char 5**	**Char 6**	
Sensor type			**Sensor type**
WOPLxx			WRe thermocouple (plunging type)
WOMAxx			WRe sheath thermocouple (mantle)
NIWIxx			NiCrNi wire thermocouple
NIMAxx			NiCrNi sheath thermocouple (mantle)
RTEM			Reference temperature sensor
LOAD			Load sensor
TRIG			Trigger input
	Location		**Sensor location**
	W		Whirl basin
	C		Supply channel
	1		Instrumentation module 1
	2		Instrumentation module 2
	3		Instrumentation module 3
	4		Instrumentation module 4
	0		Other
		Number	**Identification number**

A.2   Instrumentation Scheme

In the following table all the inserted sensors for the experiment ECOKATS1 are listed. Here is the description of the abbreviations.

Block: Terminal block for the thermocouples, 2 blocks available, each with 50 terminals.

Term: Terminal number of block.

5B01 M: Number of the I/O subsystem module 5B01 from Analog Devices. Each module has space for 16 input channels (0-15), each equipped with an amplifier matching the input signal. 3 modules are available.

5B01 CH: Channel number of the I/O subsystem module 5B01.

SCXI M: Number of the Multiplexer SCXI module from National Instruments with 32 channels. Two 5B01 modules are per Multiplexer. 2 modules are available.

SCXI CH: Channel number of the Multiplexer SCXI

CH: Input channel number of the application program under LabWindows resp. the index in the data array.

Additionally measured environmental temperatures

RTEM01:   Temperature of the 5B01 module, integrated in the module.

RTEM02:   Temperature of the terminal block under the spreading surface. Thermocouple of type Pt-100

RTEM03:   Temperature of the environment outside the measuring container. Thermocouple of type Pt-100

Special wiring for the load cells LOAD01-LOAD04

The load cells LOAD01 till LOAD04 are connected directly to four input channels of the multiplexer unit SCXI.
Each load cell has a cable with 7 conductors and is provided with a bridge amplifier.
Thus terminal 8 of the block Gx is free and terminal 9 and 10 yields the output signal.

Location	Identifier	Conductor	Block	Term	5B01 M	5B01Ch	SCXI M	SCXI Ch	Ch	Remarks
Whirl basin	WOPLW1	Screen	1	1	1	0	1	0	0	Typ D / 5B37-K-02
	WOPLW1	red +	1	2	1	0	1	0	0	Cable18
	WOPLW1	green -	1	3	1	0	1	0	0	
	WOPLW2	Screen	1	4	1	1	1	1	1	Typ D / 5B37-K-02
	WOPLW2	red +	1	5	1	1	1	1	1	Cable17
	WOPLW2	green -	1	6	1	1	1	1	1	
	WOPLW3	Screen	1	7	1	2	1	2	2	Typ D / 5B37-K-02
	WOPLW3	red +	1	8	1	2	1	2	2	Cable2B
	WOPLW3	green -	1	9	1	2	1	2	2	
Supply channel	WOPLC1	Screen	1	10	1	3	1	3	3	Typ D / 5B37-K-02
	WOPLC1	red +	1	11	1	3	1	3	3	
	WOPLC1	green -	1	12	1	3	1	3	3	
	NIMAC1	Screen	1	13	1	4	1	4	4	Typ K / 5B37-K-02
	NIMAC1	red +	1	14	1	4	1	4	4	
	NIMAC1	green -	1	15	1	4	1	4	4	
	WOPLC2	Screen	1	16	1	5	1	5	5	Typ D / 5B37-K-02
	WOPLC2	red +	1	17	1	5	1	5	5	
	WOPLC2	green -	1	18	1	5	1	5	5	
Instrument Module 1	WOPL11	Screen	1	19	1	6	1	6	6	Typ D / 5B37-K-02
	WOPL11	blue +	1	20	1	6	1	6	6	(silicon cable)
	WOPL11	brown -	1	21	1	6	1	6	6	
	WOMA11	Screen	1	22	1	7	1	7	7	Typ C / 5B30-02
	WOMA11	yellow +	1	23	1	7	1	7	7	(brown/red cable)
	WOMA11	brown -	1	24	1	7	1	7	7	
	NIWI11	Screen	1	25	1	8	1	8	8	Typ K / 5B37-K-02
	NIWI11	green +	1	26	1	8	1	8	8	(black)
	NIWI11	white -	1	27	1	8	1	8	8	
	NIWI12	Screen	1	28	1	9	1	9	9	Typ K / 5B37-K-02
	NIWI12	green +	1	29	1	9	1	9	9	(red)
	NIWI12	white -	1	30	1	9	1	9	9	
	NIWI13	Screen	1	31	1	10	1	10	10	Typ K / 5B37-K-02
	NIWI13	green +	1	32	1	10	1	10	10	(yellow)
	NIWI13	white -	1	33	1	10	1	10	10	
	NIWI14	Screen	1	34	1	11	1	11	11	Typ K / 5B37-K-02
	NIWI14	green +	1	35	1	11	1	11	11	(blue)
	NIWI14	white -	1	36	1	11	1	11	11	
Instrument Module 2	WOPL21	Screen	1	37	1	12	1	12	12	Typ D / 5B37-K-02
	WOPL21	blue +	1	38	1	12	1	12	12	(silicon cable)
	WOPL21	brown -	1	39	1	12	1	12	12	
	NIWI21	Screen	1	40	1	13	1	13	13	Typ K / 5B37-K-02
	NIWI21	green +	1	41	1	13	1	13	13	(black)
	NIWI21	white -	1	42	1	13	1	13	13	
	NIWI22	Screen	1	43	1	14	1	14	14	Typ K / 5B37-K-02
	NIWI22	green +	1	44	1	14	1	14	14	(red)
	NIWI22	white -	1	45	1	14	1	14	14	
	NIWI23	Screen	1	46	1	15	1	15	15	Typ K / 5B37-K-02
	NIWI23	green +	1	47	1	15	1	15	15	(yellow)
	NIWI23	white -	1	48	1	15	1	15	15	
			1	49						
			1	50						
	NIWI24	Screen	2	1	2	0	1	16	16	Typ K / 5B37-K-02
	NIWI24	green +	2	2	2	0	1	16	16	(blue)
	NIWI24	white -	2	3	2	0	1	16	16	
Instrument Module 3	WOPL31	Screen	2	4	2	1	1	17	17	Typ D / 5B37-K-02
	WOPL31	blue +	2	5	2	1	1	17	17	(silicon cable)
	WOPL31	brown -	2	6	2	1	1	17	17	
	WOMA31	Screen	2	7	2	2	1	18	18	Typ C / 5B30-02
	WOMA31	yellow +	2	8	2	2	1	18	18	(brown/red cable)
	WOMA31	brown -	2	9	2	2	1	18	18	
	NIWI31	Screen	2	10	2	3	1	19	19	Typ K / 5B37-K-02
	NIWI31	green +	2	11	2	3	1	19	19	(black)
	NIWI31	white -	2	12	2	3	1	19	19	
	NIWI32	Screen	2	13	2	4	1	20	20	Typ K / 5B37-K-02
	NIWI32	green +	2	14	2	4	1	20	20	(red)
	NIWI32	white -	2	15	2	4	1	20	20	
	NIWI33	Screen	2	16	2	5	1	21	21	Typ K / 5B37-K-02
	NIWI33	green +	2	17	2	5	1	21	21	(yellow)
	NIWI33	white -	2	18	2	5	1	21	21	
	NIWI34	Screen	2	19	2	6	1	22	22	Typ K / 5B37-K-02
	NIWI34	green +	2	20	2	6	1	22	22	(blue)
	NIWI34	white -	2	21	2	6	1	22	22	

Location	Identifier	Conductor	Block	Term	5B01 M	5B01Ch	SCXI M	SCXI Ch	Ch	Remarks
Instrument Module 4	WOPL41	Screen	2	22	2	7	1	23	23	Typ D / 5B37-K-02
	WOPL41	blue +	2	23	2	7	1	23	23	(silicon cable)
	WOPL41	brown -	2	24	2	7	1	23	23	
	NIWI41	Screen	2	25	2	8	1	24	24	Typ K / 5B37-K-02
	NIWI41	green +	2	26	2	8	1	24	24	(black)
	NIWI41	white -	2	27	2	8	1	24	24	
	NIWI42	Screen	2	28	2	9	1	25	25	Typ K / 5B37-K-02
	NIWI42	green +	2	29	2	9	1	25	25	(red)
	NIWI42	white -	2	30	2	9	1	25	25	
	NIWI43	Screen	2	31	2	10	1	26	26	Typ K / 5B37-K-02
	NIWI43	green +	2	32	2	10	1	26	26	(yellow)
	NIWI43	white -	2	33	2	10	1	26	26	
	NIWI44	Screen	2	34	2	11	1	27	27	Typ K / 5B37-K-02
	NIWI44	green +	2	35	2	11	1	27	27	(blue)
	NIWI44	white -	2	36	2	11	1	27	27	
Diverse	NIMA21	Screen	2	37	2	12	1	28	28	Typ K / 5B37-K-02
	NIMA21	green +	2	38	2	12	1	28	28	(green cable with screen)
	NIMA21	white -	2	39	2	12	1	28	28	
	NIWI25	Screen	2	40	2	13	1	29	29	Typ K / 5B37-K-02
	NIWI25	green +	2	41	2	13	1	29	29	(silk cable)
	NIWI25	white -	2	42	2	13	1	29	29	
	TRIG01	Screen	2	43	2	14	1	30	30	Signal provided by FZK
	TRIG01	red +	2	44	2	14	1	30	30	~24 V; voltage division: ~8 V
	TRIG01	black -	2	45	2	14	1	30	30	(5B31-03)
	RTEM02		2	46	2	15	1	31	31	Terminal block temp.
	RTEM02	HI red	2	47	2	15	1	31	31	Terminal 3 (5B34-03) Pt100
	RTEM02	LO yellow	2	48	2	15	1	31	31	Terminal 2
			2	49						
	RTEM02	RTN blue	2	50	2	15	1	31	31	Terminal 4
Load sensors	LOAD01	green	G1	1					32	Amplifier input
(spreading area)	LOAD01	grey	G1	2					32	
	LOAD01	white	G1	3					32	
	LOAD01	yellow	G1	4					32	
	LOAD01	pink	G1	5					32	
	LOAD01	brown	G1	6					32	
	LOAD01	Screen	G1	7					32	
	LOAD01		G1	8					32	
	LOAD01	grey-pink -	G1	9			2	0	32	Amplifier output <10 V
	LOAD01	blue-red +	G1	10			2	0	32	
	LOAD02	green	G2	1					33	Amplifier input
	LOAD02	grey	G2	2					33	
	LOAD02	white	G2	3					33	
	LOAD02	yellow	G2	4					33	
	LOAD02	pink	G2	5					33	
	LOAD02	brown	G2	6					33	
	LOAD02	Screen	G2	7					33	
	LOAD02		G2	8					33	
	LOAD02	white-green -	G2	9			2	1	33	Amplifier output <10 V
	LOAD02	brwn-green +	G2	10			2	1	33	
	LOAD03	green	G3	1					34	Amplifier input
	LOAD03	grey	G3	2					34	
	LOAD03	white	G3	3					34	
	LOAD03	yellow	G3	4					34	
	LOAD03	pink	G3	5					34	
	LOAD03	brown	G3	6					34	
	LOAD03	Screen	G3	7					34	
	LOAD03		G3	8					34	
	LOAD03	white -	G3	9			2	2	34	Amplifier output <10 V
	LOAD03	brown +	G3	10			2	2	34	
	LOAD04	green	G4	1					35	Amplifier input
	LOAD04	grey	G4	2					35	
	LOAD04	white	G4	3					35	
	LOAD04	yellow	G4	4					35	
	LOAD04	pink	G4	5					35	
	LOAD04	brown	G4	6					35	
	LOAD04	Screen	G4	7					35	
	LOAD04		G4	8					35	
	LOAD04	brown-olive -	G4	9			2	3	35	Amplifier output <10 V
	LOAD04	white-olive +	G4	10			2	3	35	

Location	Identifier	Conductor	Block	Term	5B01 M	5B01Ch	SCXI M	SCXI Ch	Ch	Remarks
LWL ports (not appl.)							2	4	36	not applied (LWL)
							2	4	36	
							2	4	36	
							2	5	37	
							2	5	37	
							2	5	37	
							2	6	38	
							2	6	38	
							2	6	38	
							2	7	39	not applied (LWL)
							2	7	39	
							2	7	39	
							2	8	40	
							2	8	40	
							2	8	40	
							2	9	41	
							2	9	41	
							2	9	41	
							2	10	42	not applied (LWL)
							2	10	42	
							2	10	42	
							2	11	43	
							2	11	43	
							2	11	43	
							2	12	44	
							2	12	44	
							2	12	44	
							2	13	45	not applied (LWL)
							2	13	45	
							2	13	45	
							2	14	46	
							2	14	46	
							2	14	46	
							2	15	47	
							2	15	47	
							2	15	47	
							2	16	48	not applied (LWL)
							2	16	48	
							2	16	48	
							2	17	49	
							2	17	49	
							2	17	49	
							2	18	50	
							2	18	50	
							2	18	50	
Reference temperatures	RTEM01				3	0	2	19	51	5B01 module temperature
	RTEM01				3	0	2	19	51	Wire bridge (5B37-K-02)
	RTEM01				3	0	2	19	51	Wire bridge
	RTEM03	RTN blue			3	1	2	20	52	5B34-03, term. 4, Pt100
	RTEM03	HI red			3	1	2	20	52	environment temp., term. 3
	RTEM03	LO yellow			3	1	2	20	52	Term. 2
	TRIG02	Screen			3	2	2	21	53	Signal provided by FZK
	TRIG02	red +			3	2	2	21	53	<10 V
	TRIG02	black -			3	2	2	21	53	(5B31-03)
					3	3	2	22	54	not applied
					3	3	2	22	54	
					3	3	2	22	54	
					3	4	2	23	55	not applied
					3	4	2	23	55	
					3	4	2	23	55	
Load sensors	LOAD00	Screen			3	5	2	24	56	Signal provided by FZK <10 V
(crucible)	LOAD00	black -			3	5	2	24	56	(without resistor packs:
	LOAD00	red +			3	5	2	24	56	RP4, RP8)